INFORMATION TO USERS

This manuscript has been reproduced from the microfilm master. UMI films the text directly from the original or copy submitted. Thus, some thesis and dissertation copies are in typewriter face, while others may be from any type of computer printer.

The quality of this reproduction is dependent upon the quality of the copy submitted. Broken or indistinct print, colored or poor quality illustrations and photographs, print bleedthrough, substandard margins, and improper alignment can adversely affect reproduction.

In the unlikely event that the author did not send UMI a complete manuscript and there are missing pages, these will be noted. Also, if unauthorized copyright material had to be removed, a note will indicate the deletion.

Oversize materials (e.g., maps, drawings, charts) are reproduced by sectioning the original, beginning at the upper left-hand corner and continuing from left to right in equal sections with small overlaps. Each original is also photographed in one exposure and is included in reduced form at the back of the book.

Photographs included in the original manuscript have been reproduced xerographically in this copy. Higher quality 6" x 9" black and white photographic prints are available for any photographs or illustrations appearing in this copy for an additional charge. Contact UMI directly to order.

U·M·I

University Microfilms International
A Bell & Howell Information Company
300 North Zeeb Road, Ann Arbor, MI 48106-1346 USA
313/761-4700 800/521-0600

Order Number 9326513

Growth of high In content InGaAs on GaAs substrates for optical applications

Lord, Susan Marie, Ph.D.

Stanford University, 1993

Copyright ©1993 by Lord, Susan Marie. All rights reserved.

U·M·I
300 N. Zeeb Rd.
Ann Arbor, MI 48106

GROWTH OF HIGH In CONTENT InGaAs ON GaAs SUBSTRATES FOR OPTICAL APPLICATIONS

A DISSERTATION
SUBMITTED TO THE DEPARTMENT OF ELECTRICAL ENGINEERING
AND THE COMMITTEE ON GRADUATE STUDIES
OF STANFORD UNIVERSITY
IN PARTIAL FULFILLMENT OF THE REQUIREMENTS
FOR THE DEGREE OF
DOCTOR OF PHILOSOPHY

By

Susan Marie Lord

June 1993

© Copyright by Susan Marie Lord 1993
All Rights Reserved

I certify that I have read this dissertation and that in my opinion it is fully adequate, in scope and quality, as a dissertation for the degree of Doctor of Philosophy.

Professor James S. Harris Jr.
(Principal Advisor)

I certify that I have read this dissertation and that in my opinion it is fully adequate, in scope and quality, as a dissertation for the degree of Doctor of Philosophy.

Professor Simon Wong
(Electrical Engineering)

I certify that I have read this dissertation and that in my opinion it is fully adequate, in scope and quality, as a dissertation for the degree of Doctor of Philosophy.

Professor William D. Nix
(Materials Science and Engineering)

Approved for the University Committee on Graduate Studies:

ABSTRACT

In this dissertation, the growth and device performance of high In content InGaAs quantum wells on GaAs substrates will be discussed. The motivation for this work is to produce devices on GaAs operating at 1.3 μm which is an optimal wavelength for fiber optic systems. Fabrication of long wavelength optoelectronic devices on GaAs substrates has great potential for monolithic integration of optical and high speed electronic devices for telecommunications applications.

Observation of excitons and the quantum confined Stark effect (QCSE) at 1.3 μm on GaAs using InGaAs/AlGaAs multiquantum wells (MQW) was achieved by incorporating a linearly-graded buffer layer beneath the MQW during growth by molecular beam epitaxy (MBE). This linear grading is shown to be superior to step-grading for the growth of high In content InGaAs on GaAs. Investigations of the effect of the gradient within the linearly-graded buffer revealed that slower grading yielded better quality material. Analysis of the material quality using techniques such as transmission electron microscopy (TEM) and optical absorption is discussed.

These high In content quantum wells were used as the active layers in electroabsorption modulators. Modulators are optoelectronic devices which can form an essential link between sources and receivers in fiber optic systems. Quantum well electroabsorption modulators operate via electric field induced changes in the absorption of quantum wells. The first transmission electroabsorption modulator at 1.3 μm on GaAs was demonstrated using a simple p-i-n mesa structure with a linearly-graded n-type region and MQW intrinsic region. Reflection modulators operating at 1.3 μm were produced on GaAs using a novel scheme which integrates a quarter-wave mirror stack into a linearly-graded buffer. In addition, these p-i-n structures were shown to perform as photodetectors operating at 1.3 μm with low leakage current and high internal quantum efficiency.

For my grandmothers,

Rose D'Amato DiGiore and Eva Kennedy Lord,

who were born too soon.

ACKNOWLEDGMENTS

When I was deciding on graduate schools, I remember someone telling me to go to the best possible place for my research area because my colleagues would be the future leaders in the field. From that perspective, Stanford has been an excellent choice as it has allowed me to interact with many current and future experts.

My adviser, Professor James S. Harris, Jr., has assembled an impressive array of people and facilities. I admire his skill at identifying future projects, his enthusiasm, and his generosity. One of the advantages of working for Professor Harris is that he insists that his students find a research topic on their own rather than fitting them into an established project. I thank him for this freedom and valuable lesson in self-reliance. I especially thank him for listening to me when I came to him with a few "2 by 4s".

I would also like to thank the other members of my orals and reading committees. It was a privilege to have Professor Teresa Meng as the chair of my orals committee as she has been a wonderful source of support for me. I considered Professor Simon Wong to be an excellent teacher when I took a course from him at Cornell and am pleased to have him as my associate advisor. My conversations with Professor William Nix about the structural properties of my samples, especially the dislocations, have truly been a highlight of my graduate study.

Throughout my graduate study at Stanford, I was privileged to be supported by a Graduate Research Program for Women (GRPW) Fellowship from AT&T Bell Laboratories. This program has been invaluable particularly in providing me with an insightful and wise mentor, Dr. W. Dexter Johnston, Jr. The opportunity to talk with other people in this field outside of Stanford particularly Robert Karlicek, Cammy Abernathy, and John Bean, has helped me keep things in perspective.

Collaborating with Dr. Gerhard Roos, during his time at Stanford, on the hydrogenation project was indeed a pleasure. His encouragement and confidence made my first paper and conference presentation possible for which I am deeply thankful.

Dr. Bardia Pezeshki, a graduate of the Harris group, deserves a special mention for his contribution to this work. I am continually amazed by Bardia's keen intellectual insights and adeptness in the lab. I am indebted to him for his technical assistance with processing and measurements as well as his enthusiastic support.

Collaborating with Dr. Ann Marshall of Stanford's Center for Materials Research (CMR) has been one of the most rewarding parts of this project. Her knowledge and work, as evidenced by the TEM images presented throughout this thesis, are excellent. I would also like to acknowledge the assistance of Kim Nelson of CMR in preparing the TEM samples.

Many members of the Harris group contributed to this work. I would especially like to thank the MBE gurus, especially Herman Chui and Glenn Solomon, and those who helped keep System 1 running. I sincerely appreciated the help of John Trezza with "5 minute" measurements and Mike Larson in developing a very useful simulation program. Thanks to Mark Weckwerth for writing code to implement a linear compositional grading on our MBE and to Sam-Dong Kim for his TEM work. I also thank Douglas Bone for his friendship and excellent advice on editing manuscripts and delivering presentations. I would also like to thank several graduates of the Harris group including Professor Darrell Schlom and Dr. Jim Adkisson.

The administrative support which keeps the Harris group functioning smoothly is provided by Susie Burns and Gail Chun-Creech. Their assistance in dealing with a range of issues from travel arrangements to law suits is most appreciated.

I would like to thank Dr. Judy Hoyt of the Solid State Lab for interesting discussions about linear-grading as well as RBS measurements. The assistance of Pat Johnsson at Stanford with the AFM is gratefully acknowledged. Thanks to Pauline Prather for her wire bonding expertise. Trips to Visual Arts Services at Stanford became a daily routine while preparing my oral defense and I appreciate the assistance of the people there with my microscope images.

The support and friendship of many women has been vital to my survival in graduate school. Having co-founded EE Women is one of my favorite accomplishments at Stanford. I would like to particularly acknowledge Claire Chan, Margaret Martonosi, Michele Mathys, and Kathy Richardson. I would also like to thank the facilitators, and past, and present members of the School of Engineering's Graduate Women's Support Group. I am deeply grateful to those who have kept WomenSpirit alive especially Dr. Caroline Stahle and Elaina Kyrouz. Special thanks to Reesa Abrams of Digital Equipment Corporation for her wisdom.

Finally, this work has only been possible because of the tremendous support of my family. I can never adequately thank them for this gift. I have been blessed with wonderful parents, Arthur and Rose Marie Lord. My sister Kathy has always been one of my greatest champions. Thanks to my husband, Victor Wei-chung Chang for listening, understanding, and reminding me to have fun along the way. I would also like to thank Victor's parents, Chun-shu and Shelley Chang, for their example of excellent scholarship. I have been privileged to have my grandmother, Rose DiGiore, visit me while at Stanford. I will always remember her comment when I showed her the MBE machine: "If you know how to take care of that machine, I think you can do anything."

TABLE OF CONTENTS

ABSTRACT iv
DEDICATION v
ACKNOWLEDGMENTS vi
LIST OF TABLES xiii
LIST OF ILLUSTRATIONS xiv
1. INTRODUCTION 1
1.1. Overview 1
1.2. Motivation 1
1.2.1. Advantage of long wavelength operation in InGaAs/GaAs 1
1.2.2. Strained Layer Epitaxy 3
1.3. Overview of this work 4
2. BACKGROUND: Materials, Growth, and Devices 6
2.1. Overview. 6
2.2. Materials 6
2.2.1. AlGaAs 7
2.2.2. InGaAs 7
2.2.3. InAlAs 9
2.3. Molecular Beam Epitaxy (MBE) 10
2.3.1. System 10
2.3.2. Growth 12
2.4. Devices 14
2.4.1. Electroabsorption Modulators 14
2.4.1.1. Quantum Confined Stark Effect (QCSE) 14
2.4.1.2. Structure 16
2.4.1.3. Figures of Merit 18
2.4.1.4. Measurements 19
2.4.2. Photodetectors 21
2.4.2.1. Structure 21
2.4.2.2. Figures of Merit 22
2.4.2.3. Measurements 23
2.5. Summary 24
3. STRAINED LAYER EPITAXY 25
3.1. Overview 25

3.2. Critical Thickness 25
3.3. High In Composition InGaAs on GaAs 28
3.3.1. Growth 28
3.3.1.1. Reduced Area Growth 28
3.3.1.2. Buffer Layers 29
3.3.1.3. Short Period Superlattices 30
3.3.2. Devices 31
3.3.2.1. Modulators near 1.06 μm 31
3.3.2.2. Photodetectors near 1.3 μm 32
3.4. Si-Ge Graded Buffer Layers 34
3.5. Summary 36
4. EFFECT OF GROWTH TEMPERATURE AND In COMPOSITION 37
4.1. Overview 37
4.2. Measurements 37
4.3. Effect of Growth Temperature 37
4.3.1. Samples 37
4.3.2. Results 37
4.3.3. Discussion 38
4.4. Effect of In Composition and Growth Temperature 39
4.4.1. Samples 39
4.4.2. Results 40
4.4.2.1. Transmission Electron Microscopy (TEM) 40
4.4.2.2. 77 K Photoluminescence (PL) 41
4.4.3. Discussion 43
4.5. Conclusions 45
5. STEP-GRADED VS. LINEARLY-GRADED BUFFER LAYERS 46
5.1. Overview 46
5.2. Structure and MBE Growth 46
5.3. Materials Characterization 48
5.3.1. Microscopy 48
5.3.1.1. Scanning Electron Microscopy (SEM) 48
5.3.1.2. Transmission Electron Microscopy (TEM) 49
5.3.2. Electron microprobe 52
5.3.3. Zero Field Optical Absorption 53
5.3.4. Photoluminescence (PL) 55
5.3.5. X-ray Diffraction 56

5.3.6. SIMS 60
5.3.7. Summary 61
5.4. Device Performance 62
5.4.1. Electroabsorption Modulator 62
5.4.1.1. Photocurrent 62
5.4.1.2. Quantum Confined Stark Effect 62
5.4.1.3. Transmission 63
5.4.1.4. SEED Potential 65
5.4.2. Photodetector 65
5.4.2.1. Leakage Current 65
5.4.2.2. Responsivity and Quantum Efficiency 65
5.5. Conclusions 66
6. EFFECT OF GRADIENT OF LINEARLY-GRADED BUFFER LAYERS 67
6.1. Overview 67
6.2. Structure and MBE Growth 67
6.3. Materials Characterization 69
6.3.1. Microscopy 69
6.2.1.1. Scanning Electron Microscopy (SEM) 69
6.2.1.2. Atomic Force Microscopy (AFM) 71
6.2.1.3. Plan-View Transmission Electron Microscopy 72
6.2.1.4. Cross-Section Transmission Electron Microscopy 73
6.3.2. X-ray Diffraction 76
6.3.3. Electron microprobe 78
6.4. Device Performance 79
6.4.1. Electroabsorption Modulator 79
6.4.1.1. Absorption Spectra 79
6.4.1.2. Transmission 83
6.4.2. Photodetector 83
6.4.2.1. Leakage Current 83
6.4.2.2. Responsivity and Quantum Efficiency 84
6.5. Conclusions 84
7. COMPARISON OF AlGaAs AND GaAs BARRIERS 86
7.1. Overview 86
7.2. Structure and MBE Growth 86
7.3. Materials Characterization 86
7.3.1. Microscopy 86

7.4. Device Performance 87
7.4.1. Electroabsorption Modulator 87
7.4.1.1. Absorption Spectra 87
7.4.1.2. Transmission 89
7.4.2. Photodetector 89
7.4.2.1. Leakage Current 89
7.4.2.2. Responsivity and Quantum Efficiency 89
7.5. Conclusions 91
8. REFLECTION MODULATORS 92
8.1. Overview 92
8.2. Anti-Reflection (AR) Coating 92
8.2.1. Structure and MBE Growth 92
8.2.2. Reflectivity Results 93
8.2.3. Discussion 95
8.3. Mirrors Integrated into Grading Layer 95
8.3.1. Structure and MBE Growth 96
8.3.2. Reflectivity: Experimental Results and Simulations 97
8.3.3. Discussion 100
8.4. Conclusions 101
9. CONCLUSIONS 102
9.1. Summary 102
9.2. Suggestions for Future Work 103
APPENDIX PROCESSING FOR P-I-N STRUCTURES 105
REFERENCES 109

LIST OF TABLES

TABLE 5.1 In composition in MQW determined by various techniques. 61
TABLE 5.2 Quantum efficiency for Sample III. 66
TABLE 6.1 Buffer descriptions for Samples I through V. 67
TABLE 6.2 Characteristics of clear region. 75
TABLE 6.3 Microprobe results. 79
TABLE 6.4 Zero field exciton results for Samples I through V. 81
TABLE 6.5 Modulation characteristics for Samples I, II, and III. 83
TABLE 6.6 Photodetector performance of Samples I, II, and III. 84
TABLE 7.1 Modulation characteristics for samples with GaAs and AlGaAs barriers. 89

LIST OF ILLUSTRATIONS

FIGURE 1.1 Schematic of simplified fiber optic system. 1
FIGURE 2.1 Schematic of MBE growth chamber. 11
FIGURE 2.2 Illustration of quantum confined Stark effect. 15
FIGURE 2.3 Absorption spectra for sample with thirty 75 Å $In_{0.50}Ga_{0.50}As$ quantum wells and 35 Å $Al_{0.33}Ga_{0.67}As$ barriers for various reverse bias voltages. 16
FIGURE 2.4 Schematic of a reflection modulator. 17
FIGURE 2.5 Schematic of a transmission modulator. 18
FIGURE 2.6 Schematic of transmission measurement set-up. 20
FIGURE 2.7 Schematic of photocurrent measurement set-up. 24
FIGURE 3.1 Schematic illustration of Matthews-Blakeslee model. 26
FIGURE 4.1 77 K PL spectra for InGaAs/AlGaAs quantum wells grown at 500 °C and 620 °C. 38
FIGURE 4.2 Schematic of MBE-grown samples used to study effect of growth temperature and In composition. 39
FIGURE 4.3 Cross-section TEM images of $In_xGa_{1-x}As$ quantum wells with x=0.2, 0.3, 0.4, and 0.5 grown at (a) 490 °C and (b) 535 °C. 40
FIGURE 4.4 77 K variable power PL spectra for samples grown at (a) 490 °C and (b) 535 °C. 42
FIGURE 4.5 Exciton energy versus indium composition. 44
FIGURE 5.2 SEM images of surfaces of (a) Sample I, (b) Sample II, and (c) Sample III. 49
FIGURE 5.3 Cross-section TEM images of (a) Sample I, (b) Sample II, and (c) Sample III. 50
FIGURE 5.4 High resolution TEM image of MQW grown atop a linearly graded buffer. 51
FIGURE 5.5 Cross-section TEM image of Sample III showing an area from the GaAs substrate at the bottom of the image up to just above the MQW. 52
FIGURE 5.6 300 K absorption spectra for Sample III at 0V 54
FIGURE 5.7 300 K absorption spectra for Sample I (one-step buffer) and Sample II (two-step buffer). 54
FIGURE 5.8 77 K PL spectra for Sample III for as -grown structure (heavy line) and after etching (light line) to remove top p-type layer. 56
FIGURE 5.9 X-ray diffraction spectra for Samples (a) I, (b) II, and (c) III. 58

FIGURE 5.10 SIMS spectra for Sample III. 60
FIGURE 5.11 300 K absorption spectra for Sample III at various reverse bias voltages. 63
FIGURE 5.12 Relative transmission versus wavelength at various reverse bias voltages for Sample III. 64
FIGURE 5.13 Photocurrent and transmission as a function of voltage at 1.27 μm for Sample III. 64
FIGURE 6.1 Schematic of MBE-grown structures. 68
FIGURE 6.2 SEM image (860X) of the surface of calibration sample (CalA) with 1 μm InGaAs. 69
FIGURE 6.3 SEM images (860X) of Samples (a) I, (b) II, (c) III, and (d) IV. 70
FIGURE 6.4 AFM image of (a) Sample I and (b) Sample III. 72
FIGURE 6.5 Plan-view TEM image of Sample III. 73
FIGURE 6.6 Cross-section TEM images of Samples (a) I and (b) III. 74
FIGURE 6.7 X-ray spectrum from Sample I. 77
FIGURE 6.9 Absorption spectra at various reverse bias voltages for Samples (a) I, (b) II, and (c) III.. 82
FIGURE 7.1 300 K zero field absorption spectra for samples with InGaAs/AlGaAs and InGaAs/GaAs MQW. 87
FIGURE 7.2 300 K absorption spectra at various reverse biases for (a) InGaAs/AlGaAs and (b) InGaAs/GaAs MQW. 88
FIGURE 7.3 Photocurrent spectra at 0V (heavy line) and 4V (light line) applied bias for (a) AlGaAs barriers and (b) GaAs barriers. 90
FIGURE 8.1 Schematic of AR-coated reflection modulator. 93
FIGURE 8.2 Reflectivity spectrum for AR-coated reflection modulator normalization standard. 94
FIGURE 8.3 Reflectivity spectra for AR-coated reflection modulator at 0V (heavy line) and 10V (light line) reverse bias. 95
FIGURE 8.4 Schematic of integrated mirror reflection modulator. 96
FIGURE 8.5 Reflectivity spectra for integrated mirror device at several reverse bias voltages. 97
FIGURE 8.6 Comparison of reflectivity spectra for measured device and simulation for (a) 0V applied bias and (b) 0V (heavy lines) and 8V (thin lines) applied bias. 98
FIGURE 8.7 300 K absorption spectra for InGaAs/GaAs MQW at several reverse bias voltages. 99

1. INTRODUCTION

1.1. Overview

This dissertation describes an investigation of the growth of high Indium (In) content InGaAs on GaAs substrates for optical applications. The motivation of this work is to produce useful devices for long wavelength optical fiber applications on a practical substrate and to understand the growth of highly strained materials.

1.2. Motivation

1.2.1. Advantage of long wavelength operation in InGaAs/GaAs

Fiber optic cables carry an increasing percentage of information. Perhaps the most familiar application is long distance telecommunications. Due to the material properties of the fibers, 1.3 μm is an optimal wavelength for operation of fiber optic systems. The dispersion minimum which occurs at this wavelength[1] makes for efficient propagation of light along the fiber. Practically, this efficiency could translate into advantages such as larger spacing between repeaters, which is especially beneficial for undersea applications, or greater information transmission. The simplest concept of a fiber optic system is shown schematically in FIGURE 1.1.

This system consists of a laser which serves as a source or generator of light, a detector which receives the light, and an additional element known as a modulator. This modulator controls the flow of information between the laser and the detector. In its simplest form, the modulator may be described as a switch which either allows light to pass from the source to the detector or blocks its path.

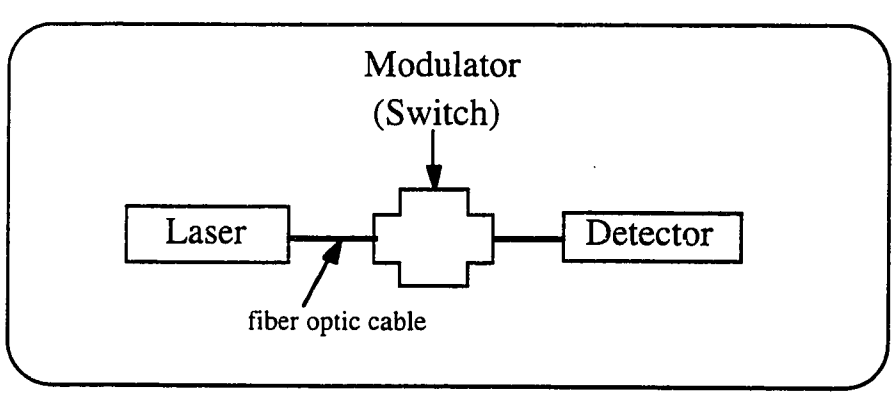

FIGURE 1.1 Schematic of simplified fiber optic system.

In addition to 1.3 μm operation, there are several other requirements for a modulator in a fiber optic system. The device should be capable of high performance and flexible in design to permit optimization for particular system applications. The modulator should be produced on a substrate which allows for monolithic integration of all system components. This offers the advantages of enhanced coupling efficiency and reduced packaging cost. Finally, having a substrate which is transparent at 1.3 μm offers the flexibility of transmission as well as reflection devices. In light of these requirements, GaAs is an excellent choice for a substrate. The bandgap of this semiconductor makes it transparent at 1.3 μm. As the most widely used semiconductor behind Si, considerable processing expertise exists for producing GaAs devices. Modulators, lasers, and detectors have all been made on GaAs substrates. Although these have included high performance devices, their limitation has been the wavelength of operation. Prior to this work, the longest wavelength modulated on GaAs was only 1.06 μm. Thus the goal of producing devices which operate at 1.3 μm on GaAs substrates is technologically important.

Although some 1.3 μm devices have been produced on InP substrates, devices on GaAs substrates offer several advantages, including; a higher degree of electronic device integration, the lack of dangerous phosphorous in a growth system, and a greater range of refractive indices for epitaxial materials which is particularly useful for devices requiring vertical cavity structures. To achieve 1.3 μm operation on InP requires InGaAsP active layers. These quaternary layers require precise control of both group III (In and Ga) and group V (As and P) species. The layers are usually produced by gas phase processes such as metal organic chemical vapor deposition (MOCVD). Both phosphine and arsine, which are used as the group V sources, are highly toxic. Because of its extreme flammability, solid phosphorous is extremely dangerous in growth systems using solid sources such as molecular beam epitaxy (MBE). Thus, the lack of phosphorous permits easier growth by a wider variety of techniques. Also, on GaAs, a ternary material such as InGaAs may be used to reach 1.3 μm. This requires control of only three sources rather than the four required for quaternary layers such as InGaAsP.

Optical modulators can interface between electronics and optics in a variety of applications including switching, information storage, beam steering,[2] mode locking and Q-switching of lasers,[3] and optical computing based on SEEDs.[4] There are many different types of modulators. In this work, only electroabsorption modulators will be considered. These modulators operate via electric field induced changes in the absorption of quantum wells. Such modulators are particularly attractive because they consist of reverse bias diodes

which operate in an efficient, low-power mode. In the InGaAs/GaAs system, these modulators offer the additional advantage of potentially high speed operation due to the relatively low barrier heights in both the conduction and valence band.

An additional motivation for the operation of optical devices at 1.3 μm is the proximity to the 1.319 μm emission line of a Nd:YAG laser and the 1.313 μm line of a Nd:YLF laser. Nd:YLF is less commonly used but is promising as it has demonstrated 20% higher optical to optical conversion efficiency than Nd:YAG.[5] The ability of optical devices to operate with such solid state lasers is particularly important for the realization of highly parallel and complex optical architectures[6,7] since these lasers are capable of sufficiently high optical power with high spectral and spatial quality to meet most system requirements. An example of such a complex architecture might be an analog fiber optic application such as cable television.

1.2.2. Strained Layer Epitaxy

The problem with producing devices operating at 1.3 μm on GaAs substrates was mostly the lack of suitable lattice matched materials. FIGURE 1.2 shows the lattice constant versus bandgap energy or operating wavelength for various semiconductors.[8] As shown in FIGURE 1.2, there is no material with a bandgap of 1.3 μm and a lattice constant equal to that of GaAs. Thus one must resort to the more complicated growth of lattice mismatched materials or strained layer epitaxy (SLE). The line joining InAs and GaAs represents the alloy InGaAs which does offer the possibility for 1.3 μm operation. However, since the lattice constant of InAs is 7.2% larger than that of GaAs, the addition of In increases both the operating wavelength and the lattice mismatch. During conventional epitaxial growth, the material quality of a mismatched layer degrades above a certain critical thickness so that it is unusable in devices. This critical thickness decreases with increasing mismatch. This will be discussed more fully in Chapter 3. The growth of InGaAs with sufficiently high In content for 1.3 μm operation had been hampered by the difficulty of obtaining sufficiently thick good quality material to be useful in realistic devices. This difficulty was overcome in this work through the use of linearly-graded buffer layers. Thus InGaAs/GaAs is a technologically interesting materials system in which to investigate the general problem of strained layer epitaxy.

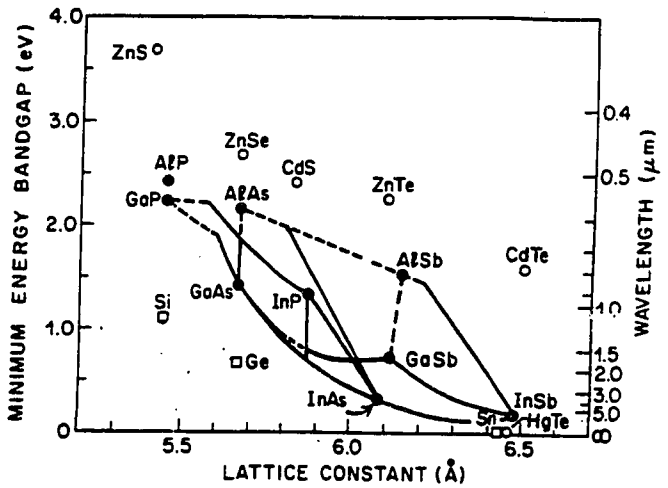

FIGURE 1.2 Minimum bandgap energy and operating wavelength versus lattice constant for various semiconductor materials. Lines connecting binary compounds represent ternary alloys. Solid lines indicate a direct bandgap while dashed lines indicate an indirect bandgap.(after Ref. 9)

1.3. Overview of this work

This thesis describes the growth, characterization, and device performance of high In content InGaAs layers grown atop GaAs substrates using molecular beam epitaxy (MBE). Chapter 2 summarizes the background for this thesis including materials, growth, and devices. Chapter 3 describes strained layer epitaxy and reviews relevant literature concerning long-wavelength (1.06 μm and 1.3 μm) InGaAs/GaAs as well as the related strained materials system of $Si_{1-x}Ge_x$/Si. Chapter 4 examines the effect of growth temperature and In composition on InGaAs quantum wells. Chapters 5 through 7 describe several experiments to optimize growth of high In content InGaAs on GaAs. Materials characterization including electron microscopy, optical absorption, and X-ray diffraction as well as device performance of this material in an electroabsorption modulator and a photodetector are considered. Chapter 5 provides a comparison of the growth of high In content InGaAs quantum wells on GaAs substrates using step-graded and linearly-graded buffer layers. The promising results from the linearly-graded buffer layer are further explored in Chapter 6 which considers the effect of varying the gradient of this graded buffer. Chapter 7 compares high In content InGaAs quantum wells with GaAs and AlGaAs barriers. The modulators described in Chapters 5 through 7 are transmission modulators. Chapter 8 deals with two techniques for producing reflection modulators

using these same materials. Finally, Chapter 9 contains a summary of conclusions from this work and suggestions for future work. An appendix describes the processing sequences used in preparing the devices described in this thesis.

2. BACKGROUND: Materials, Growth, and Devices

2.1. Overview

This chapter provides an introduction to the materials, growth technique, and device principles which serve as the foundation for this work. First, the materials and their parameters will be presented. Following this, the specific materials growth technique used, molecular beam epitaxy, will be explored. Finally, some details of the operation and measurements of the devices, specifically modulators and photodetectors, produced in later chapters will be discussed.

2.2. Materials

The materials described in this thesis are known as III-Vs since they are comprised of elements from Columns III and V of the periodic table. The epitaxial layers mainly consisted of AlGaAs and InGaAs. Some of the mirror layers described in Chapter 8 also included InAlAs. These are all semiconductors and may be characterized by their bandgap which is the energy difference between the top of the valence band and the bottom of the conduction band. The optical transition associated with this bandgap may be direct or indirect. Direct bandgap transitions require no momentum change, generate light efficiently, and result in excellent optical devices. Materials with indirect bandgap transitions are extremely inefficient in optical devices.

GaAs and AlGaAs are the most commonly used III-V semiconductor materials. AlGaAs has even become a "common household item" in the laser diodes of compact disk (CD) players.[9] Most III-V semiconductors including InGaAs, GaAs, and AlGaAs for compositions up to 45% Al, have direct bandgaps which gives them an advantage over the most commonly used semiconductor Si which is an indirect gap material. Thus III-V optical devices are much more efficient than Si optical devices. In general, III-V materials have higher carrier mobilities than Si which results in faster electronic devices.[10] However, the processing difficulties of such compound semiconductors compared with elemental Si, including lack of a stable native oxide and the lower level of technological expertise, has made it difficult for III-Vs to compete in commercial electronic devices.

This section describes the important material parameters such as lattice constant, bandgap, and refractive index for the semiconductors studied in this thesis. These parameters are useful for understanding the growth of the materials as well as for device design.

2.2.1. AlGaAs

As shown in FIGURE 1.2, the lattice constants of AlAs and GaAs are almost identical. Thus the full range of compositions of $Al_xGa_{1-x}As$ may be grown essentially lattice matched to a GaAs substrate providing high quality structures and interfaces. The growth of AlGaAs on GaAs has been widely studied and a considerable body of literature exists on the topic.[11] Of course, the growth of extremely high quality material does involve the optimization of such factors as growth temperature, V/III ratio, source furnace design, system preparation, and high purity source materials.

Since AlGaAs has a larger bandgap than GaAs, the combination of the two materials offers an excellent system for producing quantum wells. For compositions below 45% aluminum, AlGaAs is a direct bandgap material while for higher Al compositions, the band structure results in an indirect transition. Most of the physical parameters for AlGaAs may be described as a function of its aluminum composition, x. The lattice constant is given by

$$a = 5.6536 + 0.0069x \tag{2-1}$$

The 300 K bandgap of the alloy in eV at the Γ point is[12]

$$E_g=1.424 + 1.247x \qquad x \leq 0.45 \tag{2-2}$$

$$E_g=1.900+0.125x+0.143x^2 \qquad x \geq 0.45 \tag{2-3}$$

For direct gap AlGaAs, the conduction band discontinuity (ΔE_C) of AlGaAs/GaAs is about 65% of the total discontinuity and the valence band discontinuity (ΔE_V) is 35%.[13] The refractive index, which is an important parameter for the design of multilayer optical structures, varies approximately linearly from about 3.0 in AlAs to 3.5 in GaAs for energies slightly below the bandgap. This is the region usually used for devices such as modulators, since the material is transparent but electro-optic effects are strong.

2.2.2. InGaAs

The materials system of InGaAs on GaAs has not been as extensively studied as that of AlGaAs on GaAs. The high carrier mobilities of InGaAs make it attractive for electronic devices while its small bandgap is desirable for long wavelength optical devices. InGaAs may be grown lattice matched to InP at a composition of 53% In and virtually all of the information on InGaAs is available for that specific composition. However, there is no composition of InGaAs which lattice matches GaAs. Thus, as described in Chapter 1, the

growth of InGaAs on GaAs involves strained layer epitaxy. Numerous transport and optical devices have been produced with In compositions of less than about 30% e.g. strained InGaAs on GaAs including HEMTs,[14] HBTs,[15] lasers,[16] and modulators.[17] However, growth of higher In content material has been difficult and larger In concentrations are necessary to achieve 1.3 μm operation.

Besides strain, another factor which distinguishes InGaAs growth from AlGaAs or GaAs growth is that In tends to desorb preferentially from the surface of a wafer at a temperature above about 550 °C. Thus growth of InGaAs on GaAs must be performed at substrate temperatures lower than 550 °C to maintain good control of growth rates and insure uniform deposition. Since high quality AlGaAs is usually grown above 600 °C, this creates problems for the simultaneous optimization of InGaAs and AlGaAs. Optimization of growth temperature for InGaAs will also be considered in Chapter 4. High performance minority carrier devices such as HBTs have been produced by determining a temperature window for simultaneous high quality growth of InGaAs and AlGaAs.[18] However, the strict material requirements of devices such as lasers have led researchers to change growth temperature during growth of InGaAs and AlGaAs to attain the highest quality material. Such changes complicate the growth but avoid the incorporation of interface defects. See Appendix A for more details.

As with the AlGaAs alloy, the parameters of $In_xGa_{1-x}As$ may be described in terms of its indium composition, x. The lattice constant is given by

$$a = 5.6536 + 0.4054x \tag{2-4}$$

For bulk material, the room temperature (300 K) and 77 K bandgaps are given by

300K $$E_{gbulk} = 1.424 - 1.614x + 0.540x^2 \tag{2-5}$$

77K $$E_{gbulk} = 1.508 - 1.470x + 0.375x^2 \tag{2-6}$$

However, strain effects must also be considered. The most important effect of the strain is to break the degeneracy of the light and heavy hole bands at the top of the valence band.[19] This results in an increase in the bandgap as the bands shift to lower energies as well as changes in the effective masses.[20,21,22] Thus the change in bandgap for InGaAs on GaAs due to strain may be described by[13]

$$\Delta E_{gstrain} = 0.4484x - 0.3573x^2 + 0.02168x^3 \quad (2\text{-}7)$$

which is assumed to be independent of temperature. There is not general agreement on the appropriate values for the bandgap discontinuities in InGaAs/GaAs. Values from 83/17 to 11/89 have been reported for $\Delta E_C/\Delta E_V$.[23] In this thesis, a 60/40 split[24] between the conduction and valence bands is used.[25] Because the strain primarily affects the valence band, the calculations of the offsets must be done as follows

$$\Delta E_C = 0.60 \Delta E_{gbulk} \quad (2\text{-}8)$$

$$\Delta E_V = 0.40 \Delta E_{gtotal} \quad (2\text{-}9)$$

where

$$\Delta E_{gtotal} = \Delta E_{gbulk} + \Delta E_{gstrain} \quad (2\text{-}10)$$

Determining the refractive index of InGaAs a function of x and wavelength is quite difficult. Tabulated values do not exist. Interpolating between values for InAs and GaAs[26] disagrees drastically with the available experimental data. This may be due to the peculiarities of the extremely small InAs bandgap. Some data does exist for InGaAs lattice matched to InP[27] and for compositions up to 50% In.[28] A single-effective-oscillator model proposed by Wemple and DiDomenico[29] expresses refractive index for a material as a function of energy E as

$$n = \sqrt{1 + \frac{E_o E_d}{E_o^2 - E^2}} \quad (2\text{-}11)$$

where E_o and E_d are constants which are a function of composition. For $In_xGa_{1-x}As$, these constants are taken from Takagi[28]

$$E_o = 3.65 - 2.15x \quad (2\text{-}12)$$

$$E_d = 36.1 - 19.9x \quad (2\text{-}13)$$

which is basically a linear interpolation between the values for the binaries. This gives a reasonable fit to the experimental data.

2.2.3. InAlAs

Less work has been done on InAlAs than on InGaAs. It is most commonly used as the high bandgap companion material for InGaAs on InP as it may be grown lattice matched to InP at a composition of 52% In. For the purposes of this thesis, InAlAs is only used as the high index material of the integrated quarter-wave mirrors in Chapter 8. For this application, the most important parameter is the refractive index. Strain effects between InAlAs and InGaAs will not be considered as it will be assumed that they are lattice-matched for a given In concentration. As with InGaAs, tabulated values for the refractive index of InAlAs including dispersion and composition dependence do not exist and interpolating between values for InAs and AlAs[26] is not useful. Dingle et al. reported some data for $In_{0.52}Al_{0.48}As$ over a limited wavelength range.[27] We may again use the model of Wemple and DiDomenico and interpolate between the binaries[28,30] to obtain the following constants for $In_xAl_{1-x}As$

$$E_o = 4.7 - 3.2x \tag{2-14}$$

$$E_d = 33.65 - 17.45x \tag{2-15}$$

2.3. Molecular Beam Epitaxy (MBE)

All of the materials described in this thesis were grown on two inch GaAs substrates by molecular beam epitaxy (MBE). What is known today as MBE began in the 1960s[31,32,33] following studies of evaporation rates and sticking coefficients of various elements on substrates.[34] Today, this versatile technique is used for the growth of a variety of materials including semiconductors, insulators, metals, and superconductors. The brief introduction in this chapter will concentrate on growth of III-V semiconductors by MBE. Several excellent reviews are available for more information.[35,36]

2.3.1. System

A modern MBE system consists of a load chamber, a growth chamber, and an optional analysis chamber. The system used for this work at Stanford University is a modified Varian GEN-II with capability for growth on 2" or 3" diameter substrates. In this thesis, all growths were on two inch GaAs substrates. Wafers are radiatively heated on In-free holders. After an initial chemical clean, wafers are placed in a load chamber and baked at 400 °C at a pressure of 10^{-6} Torr for 1 hour primarily to drive off water vapor. Then the wafers are transferred to the growth chamber where the base pressure is about 10^{-10} Torr. Such ultra high vacuum (UHV) conditions are necessary for the growth of highly pure materials. Pressures less than about 10^{-4} Torr insure that the source to substrate distance is shorter than the mean free path of particles in the chamber. Thus the particles in the

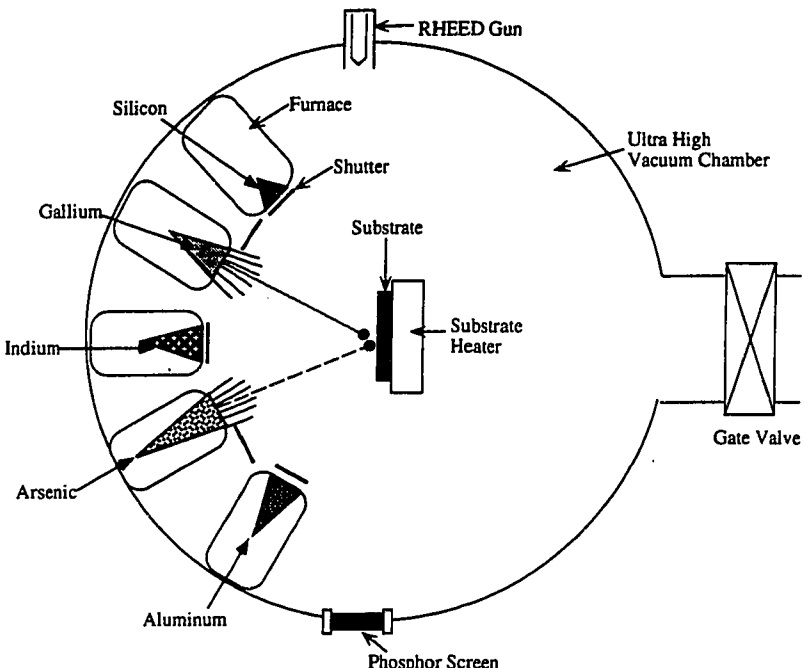

FIGURE 2.1 Schematic of MBE growth chamber.

chamber experience molecular flow. Various pumps including cryogenic, ion, and Ti sublimation, are used to maintain UHV conditions.

The growth chamber is shown schematically in FIGURE 2.1. The outer walls of the chamber are continuously cooled with liquid nitrogen (LN2) so that excess material which does not deposit on the substrate during growth will attach to the walls preventing "memory effects" where a species from a previously grown layer can contaminate a present growth. The growth chamber also includes analysis equipment such as a reflection high energy electron diffraction (RHEED) gun and phosphor screen and a quadropole mass spectrometer. The mass spectrometer is used to identify the constituents of the vacuum, especially when a leak is suspected. RHEED is very useful for calibrating growth rates especially those of GaAs and AlAs.[37,38] While keeping the substrate position fixed, oscillations are observed in the intensity of a particular spot on the RHEED screen as layers of material grow. One period of this oscillation corresponds to the growth of one monolayer (ML) of material.

Thus MBE has the capacity for monolayer-scale control. MBE may also be described as atomic layer spray painting[39] since individual layers of atoms are sprayed or deposited onto the surface. RHEED patterns can also be used to gain insights into growth processes and

to assess the quality of the growing material. A spotty pattern indicates rough growth while long streaks illustrate smooth growth.

Several sources are contained in an MBE growth chamber. At Stanford, we typically have two gallium, one aluminum, one indium, and two arsenic sources. Dopants include Si for n-type and Be for p-type doping. Each source is contained in a pyrolitic boron nitride (p-BN) conical crucible which is housed in a furnace known as an effusion or Knudsen cell. The evaporation rate or growth rate of each species is a function of its temperature. This temperature is determined by the power to the furnace which is computer controlled via a Eurotherm controller and a thermocouple. Each furnace has a shutter at its entrance to the growth chamber. By opening and closing these shutters, one can choose which materials will be deposited on the substrate during growth e.g. opening the In, Ga, and As shutters produces InGaAs. The substrate is rotated during growth to insure uniform growth. However, even with rotation, there is usually about a 2% variation in thickness and composition across a 2" wafer.

Growth rate calibrations are performed after each loading of new source material. For Group III materials, equations relating flux to temperature and growth rate to flux are determined from RHEED oscillations, X-ray diffraction data, and photoluminescence (PL). Because the amount of dopants used is so small, it is not possible to measure their fluxes. Thus calibration for dopants relies on growths of samples with varying doping that are characterized using Hall effect measurements and Polaron electrochemical profiling. Flux measurements may be made immediately prior to growth using a Bayard-Alpert ion gauge situated in the growth chamber. Although the furnace temperature is the controllable parameter via the power into the windings, the flux is the measurable parameter. As these are not linearly related, executing a linear grading, as will be described in Chapter 5, is rather complicated.

2.3.2. Growth

Epitaxy, from the Greek words *epi* and *taxis* meaning "upon" and "ordered", is the ordered growth of a material upon a substrate. In this work, epitaxy refers to the growth of a single crystal thin film on a single crystal substrate. MBE is a nonequilibrium process. Because MBE is conducted in the molecular flow regime, there are no collisions or chemical reactions of the incident species until they reach the substrate surface and surface kinetic reactions dominate the deposition. Thus growth of compounds which would not appear as stable on equilibrium phase diagrams is possible. Indeed, a wide variety of materials with

different bandgaps may be grown, which has given rise to the term bandgap engineering. The exact kinetics and growth mechanisms of the MBE growth process are an area of continuing research. However, a great deal of practical experience does exist.

Growth rates in MBE are determined by the Group III species. An overpressure of the Group V species (in this work arsenic) is required for successful growth of III-V compounds on GaAs. The excess arsenic prevents the desorption of arsenic from the surface of the substrate which would cause excessive roughness and prevent the initiation of smooth growth. Arsenic will not stick to other arsenic atoms on the surface but only to exposed Group III atoms. A sufficient amount of arsenic is required to guarantee stoichiometry. Two types of arsenic sources are available. A typical Knudsen cell similar to the furnaces for the other sources but larger (40 cc rather than 16 cc) may be used to supply tetrameric arsenic, As_4, which is the equilibrium vapor species over arsenic. Tetrameric arsenic has been the most widely used species. However, the equilibrium vapor species over GaAs is the As_2 dimer. Hence, directly supplying As_2 is desirable and has become increasingly popular. Dimer arsenic may be obtained using a special two-stage arsenic cracking furnace or "cracker". A cracker consists of a low temperature sublimator section where solid arsenic is heated to control the magnitude of the flux and a high temperature cracking section which produces As_2.[40,41] It is believed that the incorporation of As_4 is a second order process[42] whereby the As_4 molecule must first break into two As_2 dimers before incorporating on the surface. Since As_2 incorporates in a first order process,[43] it is more efficient. The sticking coefficient of As_4 is estimated to be ≤ 0.5 while that of As_2 is appreciably higher, approaching unity. Thus less As_2 than As_4 is required for successful growth. Studies have shown improved optical quality for material grown with As_2.[44,45] High purity growth requires the minimum possible V/III ratios.[46] However since Group III-rich material exhibits very poor surface morphology, for most applications it is safer to operate in a definitely Group V-rich regime. Typical values of V/III ratio are about 12:1 for As_2 versus 20:1 for As_4. Group III constituent fluxes are usually on the order of 10^{-7} Torr for typical growth rates of about 1 μm/h or 3 Å/s or 1 ML/s.

The most common competing thin film epitaxial growth technique is metal organic chemical vapor deposition (MOCVD). MOCVD is a purely gas-phase process relying on surface chemistry. One of its main advantages is a high throughput which makes it attractive for manufacturing environments. Its disadvantages include the need for highly toxic gases for growth of III-Vs and perhaps slightly less abrupt interfaces. MOCVD may be performed at

atmosphere or at "low pressures" of milliTorr. More recently, other techniques have emerged which attempt to synergize the desirable features of MBE and MOCVD. These include gas source MBE (GSMBE), metal organic MBE (MOMBE), and chemical beam epitaxy (CBE).[47]

2.4. Devices

Electroabsorption modulators and photodetectors are important photonic systems components and they were chosen to demonstrate the performance of InGaAs/GaAs devices at 1.3 μm. The fairly simple structures and processing required make them attractive candidates for eventual integration with GaAs electronics for optoelectronic integrated circuits (OEICs). This section will introduce the devices and then discuss their structure, parameters which serve as figures of merit, and the measurement techniques employed for evaluating these parameters.

2.4.1. Electroabsorption Modulators

Numerous types of optoelectronic modulators are described in references such as Hunsperger.[48] As described in Chapter 1, a modulator is a device which controls the flow of information carried on a lightwave system between a transmitter and a receiver. The modulators described in this thesis are multiquantum well (MQW) electroabsorption modulators based on the quantum confined Stark effect (QCSE). These devices may be used to modulate either the reflected or transmitted intensity of an external light source, such as a laser.

Electroabsorption modulators have potential uses in a variety of applications including optical computing and optical interconnection. A considerable amount of research is presently underway to optimize the design and performance of such modulators for particular tasks.[49]

2.4.1.1. Quantum Confined Stark Effect (QCSE)

To understand how these modulators operate, it is necessary to understand a quantum well and the quantum confined Stark Effect (QCSE).

One of the interesting consequences of a precise growth technique such as MBE is the ability to physically realize structures which exhibit quantum mechanical effects. The most commonly studied such structure is the quantum well. A quantum well consists of a relatively thin (< 500 Å) layer of a material with a small bandgap sandwiched between two

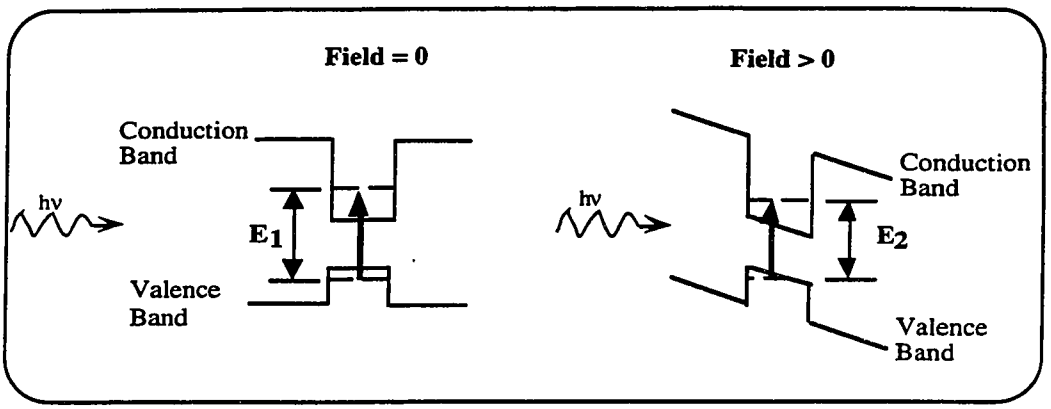

FIGURE 2.2 Illustration of quantum confined Stark effect.

layers of material with a larger bandgap. Thus the quantum well may be thought of as the physical realization of the particle in a finite box problem and the eigenvalue problem may be solved using the envelope approximation described in introductory quantum mechanics textbooks. The microscopic details of the materials, such as band structure, are taken into account through parameters such as effective masses and band offsets, ΔE_V and ΔE_C.[50]

For a quantum well, the energy levels in the growth direction become quantized. Thus only two degrees (2D) of freedom remain. This 2D character is reflected in the density of states of the quantum well which is step-like rather than smooth as for the 3D bulk material. Large resonances are observed at the step edges due to the presence of excitons. Excitons are a continuing topic of extensive research.[51,52,53] Basically, an exciton consists of an electron and a hole bound together in a hydrogenic-like state where the bonding is Coulombic attraction. The large overlap related to this coupling results in strong optical transitions and hence peaks in the optical absorption and photoluminescence. The formation of excitons is greatly enhanced in a quantum well compared to bulk material because of the spatial localization of electrons and holes.

When isolated quantum wells are placed in an electric field, a quantum-mechanical phenomenon known as the quantum confined Stark effect (QCSE)[54] is observed. Corresponding to a red shift in the absorption edge, this is similar to the Franz-Keldysh effect in bulk materials but is many times stronger. The reason for the QCSE may be understood using FIGURE 2.2.[55]

At zero bias, the lowest lying confined levels for electrons and holes are indicated as dashed lines. Thus the exciton will have an energy roughly equal to the difference in

energy between these levels. Upon application of a field, however, the oppositely-charged electron and hole wavefunctions are drawn to opposite sides as the well is tilted. Thus the optical transition occurs at a lower energy or longer wavelength. However, another consequence of such spatial separation is the reduction of the overlap of the electron and hole wavefunctions. Thus, the exciton resonance becomes weakened as the field is increased. This is illustrated in FIGURE 2.3. Excitons also exist in bulk material. However, without barriers to enhance confinement, they are quickly ionized and have very short lifetimes.

A structure exhibiting the QCSE may be used as an electroabsorption modulator since for a fixed wavelength, the application of a voltage changes the amount of absorption. One may operate a modulator in either of two regions as shown in FIGURE 2.3. Operating at the wavelength of the zero field exciton means that the absorption decreases with the application of an electric field. This is known as a normally off device. A normally on device may be produced by operating at a wavelength longer than the zero field exciton wavelength. In this case, the application of an electric field causes increased absorption.

2.4.1.2. Structure

To construct a modulator, the quantum wells are usually placed within the intrinsic region

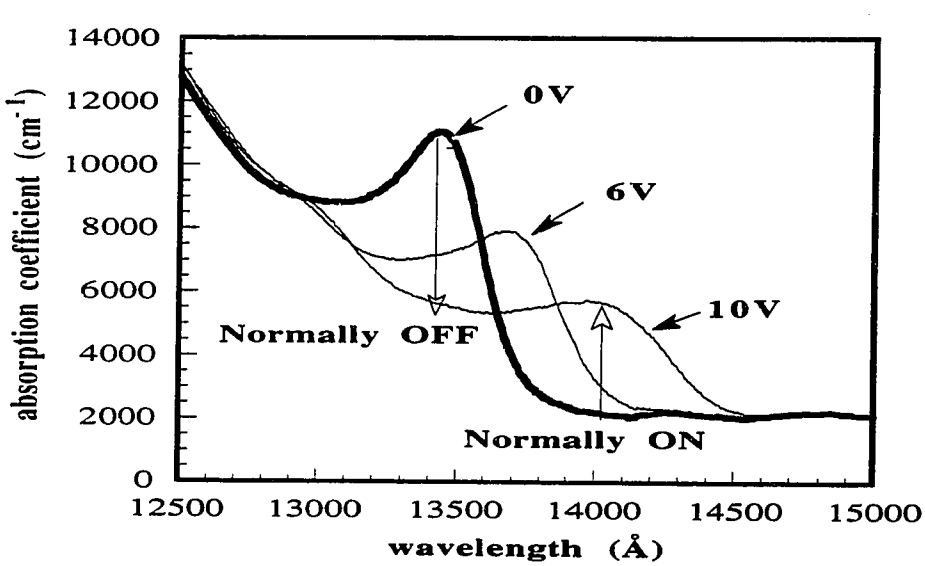

FIGURE 2.3 Absorption spectra for sample with thirty 75 Å $In_{0.50}Ga_{0.50}As$ quantum wells and 35 Å $Al_{0.33}Ga_{0.67}As$ barriers for various reverse bias voltages.

of a p-i-n structure. Since the absorption coefficient in semiconductors is about 10^4 cm^{-1}, multiple quantum wells are necessary in order to observe appreciable absorption. Thus these electroabsorption modulators will contain at least ten quantum wells, unlike most quantum wells lasers which contain fewer than five quantum wells for single mode operation. The barriers between the quantum wells in a modulator must be thick enough to prevent tunneling or electronic coupling between the wells which would result in miniband formation. For most III-V materials systems, this thickness is about 35 Å.

Reflection modulators are produced by incorporating highly reflecting quarter-wavelength mirrors into the n and/or p layers of such a p-i-n structure. The use of a Fabry-Perot (F-P) cavity in a device including mirrors enhances performance by providing a sharp dip in the zero-field reflectivity. FIGURE 2.4 shows an asymmetric F-P reflection modulator which will be discussed in Chapter 8. This structure has only a bottom mirror. If the n and p type layers are merely thick contact layers, the device would work in transmission as shown in FIGURE 2.5. Higher performance may be obtained with reflection modulators since they are capable of higher contrast ratios than transmission modulators.[56]

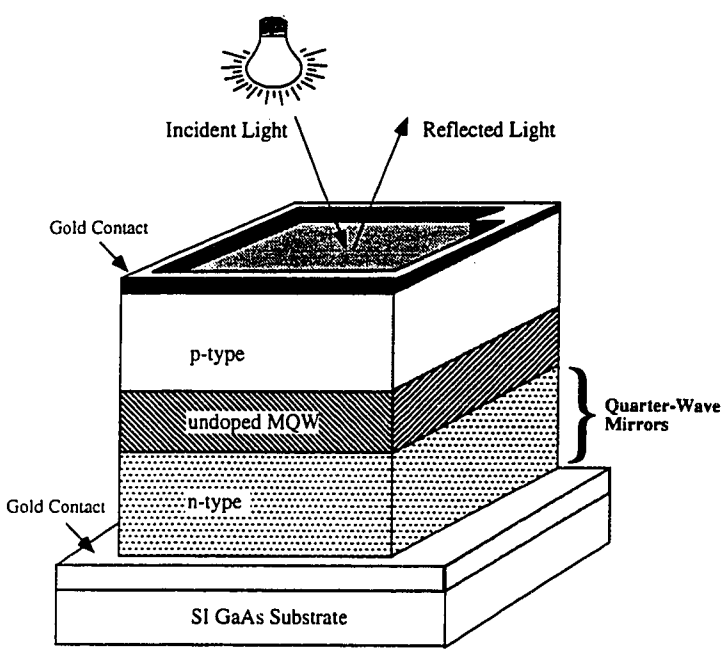

FIGURE 2.4 Schematic of a reflection modulator.

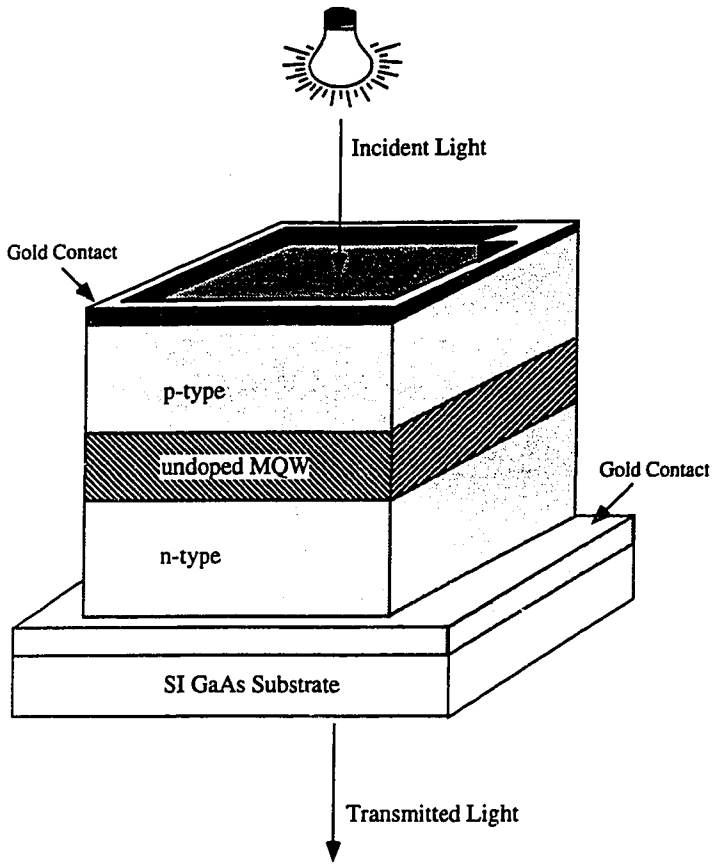

FIGURE 2.5 Schematic of a transmission modulator.

The fabrication process for the modulators is described in the appendix. Briefly, the wafers are chemically etched down to the n-type material to define isolated mesas. Contact to the n-type material is made using an alloyed Au/Ge/Ni/Au contact. Finally, Ti/Au is used to form a p-type contact. The devices measured in this work were 500 μm x 500 μm in area. Solid pads and annular rings were used for the p-type contacts. The annular rings permit the operation of transmission devices.

2.4.1.3. Figures of Merit

Figures of merit for modulators include contrast ratio, modulation depth, and insertion loss. Modulation depth or modulation index may be expressed in terms of the relative transmission, $\Delta T/T_0$ or reflection, $\Delta R/R_0$, where

$$\Delta T(V) = T(V) - T_0 \tag{2-16}$$

$$\Delta R(V) = R(V) - R_0 \tag{2-17}$$

where T(V) and R(V) are the transmission and reflectivity at a bias voltage of V and T_0 and R_0 are the transmission and reflectivity at zero volts. Modulation may also be described by modulation ratio (MR) or contrast ratio (CR). For a reflection device, modulation ratio is defined as the ratio of maximum reflectivity, R_{max}, to minimum reflectivity, R_{min}. For a transmission device, MR is the ratio of maximum transmission, T_{max}, to minimum transmission, T_{min}.

$$MR = R_{max}/R_{min} \quad \text{(Reflection Device)} \quad (2\text{-}18a)$$

$$MR = T_{max}/T_{min} \quad \text{(Transmission Device)} \quad (2\text{-}18b)$$

Contrast ratio may be expressed in dB as

$$CR = 10\log_{10}(MR) \quad (2\text{-}19).$$

The insertion loss (IL) or light lost coupling into the device is defined by equation 2-20a for a transmission device and equation 2-20b for a reflection device.

$$IL = -10\log(T_0) \quad \text{(Reflection Device)} \quad (2\text{-}20a)$$

$$IL = -10\log(R_{max}) \quad \text{(Transmission Device)} \quad (2\text{-}20b)$$

Bandwidth and switching time are particularly important parameters for modulators used in large-scale arrays. Operating voltage and wavelength are parameters which depend upon device design, particularly the quantum well structure. Minimizing power consumption and maximizing isolation among inputs and outputs to reduce crosstalk are also important design criterion for systems integration. Of course, there are trade-offs in optimizing all of these parameters.[56]

2.4.1.4. Measurements

When performing optical measurements on these devices, it is essential that all optics. including beam splitters, lenses, and mirrors, are suitable for the wavelength range of interest. Since the wavelength range here is near 1.3 μm, it is necessary to use an infrared (IR) viewer to image the devices. All measurements were performed at 300 K on an isolated optical table using an Oriel tungsten white light source, a 300 K Ge detector, and a Spex one-half meter spectrometer. The spectrometer and lock-in amplifier were both under computer control.

For a transmission device, a transmission measurement may be done and the absorption coefficient determined from that data. FIGURE 2.6 shows a schematic of such a set-up.[57] The devices were epoxied into drilled chip carriers and wire bonded so they could be held vertically with a filter clamp mounted on an xyz stage. The white light is incident on the back of the entire packaged device. Since the package is opaque, only light from the region within the drilled hole is transmitted. This transmitted light is then focused with a camera lens and irises are used so that only the transmitted light from a single device enters the spectrometer. To image the device on iris 2 using an IR viewer, the chopper must be off. The 830 nm filter enables the device to be more easily viewed with the IR viewer. A 300 K Ge detector and lock-in are used to collect the data. The periscope shown in the figure changes the height of the beam from the low level used on the table to the higher level used for entering the spectrometer. The measured signal is then divided by the white light spectrum to obtain a transmission signal. The spectrometer grating for these long wavelengths has several anomalies (Wood's) near 1.35 μm. This complicates the data acquisition and makes it crucial to have reliable white light spectra for normalization.

Transmitted intensity, T, through a material of thickness t may be expressed as:[58]

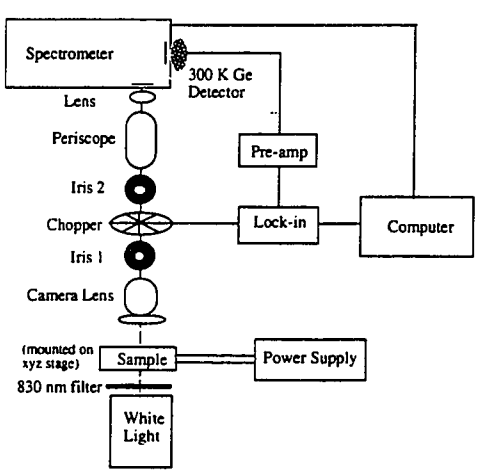

FIGURE 2.6 Schematic of transmission measurement set-up.

$$T = \frac{(1-R)^2 e^{-\alpha t}}{1-R^2 e^{-2\alpha t}} \tag{2-21}$$

where R is the reflection coefficient from the surface and α is the absorption coefficient. Using the quadratic equation, one may obtain an expression for α directly:

$$\alpha = -\frac{1}{t}\ln\left[\frac{-(1-R)^2 \pm \sqrt{(1-R)^4 + 4T^2R^2}}{2TR^2}\right] \tag{2-22}$$

To obtain an accurate determination of the zero absorption level requires a very precise value for R. Also, when computing the absorption coefficient for quantum wells within a p-i-n structure, it is often necessary to subtract the bulk absorption, such as that for a blank GaAs wafer.

For reflection modulators, the most common measurement is reflectivity. The set-up for such a measurement is similar to that for the transmission measurement. However, the white light source is focused down on the desired device using a beam splitter cube and a focusing lens. A doublet is used for this focusing lens to minimize chromatic aberration. For measurements near 1.3 μm, the best available beam splitter still has a nonlinear response. After illumination, the reflected light is then collected by the focusing lens, goes through the beam splitter and several mirrors and enters into the spectrometer. Thus the sample is situated beneath the beam splitter, flat on the table rather than held vertically as in the transmission measurement.

2.4.2. Photodetectors

Photodetectors, devices which detect optical signals through electronic processes, are used in a large variety of applications, especially optical fiber communication systems. They act, for example, as the receivers in the simple system shown in FIGURE 1.1. The photodetectors produced in this work and used in most communication systems are more specifically photodiodes since a reverse-biased p-i-n structure is essential to the detection. Basically, when a photon incident on a p-i-n structure creates a photogenerated electron-hole pair, the field within the depletion region separates the electron and hole producing a current known as photocurrent. Thus incident light may be detected by measuring the photocurrent. A good introduction to photodetectors may be found in the reference by Sze.[59]

2.4.2.1. Structure

Since modulators and photodetectors are both p-i-n diodes, the same structure may be operated as either a modulator or photodetector. However, it will not be simultaneously optimized for both applications. The depletion region of a p-i-n photodetector may be tailored to optimize the quantum efficiency and frequency response. Such devices are usually small to minimize junction capacitance unlike solar cells where the need for high power conversion efficiency spurs the production of large area devices.

2.4.2.2. Figures of Merit

Responsivity and quantum efficiency are important figures of merit for photodetectors. Both quantities measure the amount of current generated per photon of light incident on the device. Quantum efficiency is given by

$$\eta=\frac{I_p h\nu}{P_{opt} q} \tag{2-23}$$

where q is the Coulombic charge, I_p is the photocurrent (exclusive of reverse leakage current) generated by the absorption of incident optical power, P_{opt}, at an energy of $h\nu$ where h is Planck's constant equal to 6.62×10^{-34} Js and ν is given by c/λ where c is the speed of light, 3×10^8 m/s. Responsivity in A/W is then given simply by

$$R=\frac{\eta\lambda}{1.24} \tag{2-24}$$

where λ is the wavelength in μm. Of course, for an ideal photodiode, η equals 1 or 100%. Calculation of quantum efficiency and responsivity may be done in two ways. Using the total power incident on the device yields the external values. The internal values may be determined by including only the amount of optical power incident on the active portion of the device i.e. the quantum wells. This involves estimating the amount of absorption in other areas of the device. To calculate internal values from external values, one may use the following relationship:

$$\eta_{in} = \eta_{ex}\frac{P_{opt}}{P_{in}} \tag{2-25}$$

P_{in} is the amount of power actually absorbed in the active area of thickness L (i.e. the MQW). It is the sum of the optical power traveling from the top into the MQW and the amount traveling from the bottom into the MQW. P_{in} may be expressed as

$$P_{in} = \frac{(1-e^{-\alpha L})(1+R_2 e^{-\alpha L})(1-R_1)}{1-R_1 R_2 e^{-2\alpha L}} P_{opt} \tag{2-26}$$

where α is the absorption coefficient of the active layer material, R_1 is the reflectivity of the bottom interface and R_2 is the reflectivity of the top interface.

The quantum efficiency is strongly determined by the absorption coefficient of the material which is also a function of wavelength. Devices with larger depletion regions have more absorption but at the cost of longer transit times. Thus maximizing quantum efficiency provides a trade-off with maximizing the speed of operation of the detector, another important parameter. Since photodetectors are operated under reverse bias, their reverse leakage characteristics are also important. If a device has too large of a leakage current, it will not function effectively as a photodetector.

2.4.2.3. Measurements

To determine the responsivity of a device, the photocurrent generated when the device is illuminated and the power of the illuminating light are measured. A schematic of a set-up for the measurement of photocurrent is shown in FIGURE 2.7. White light is taken through the spectrometer and the exiting monochromatic light is focused down on the desired device using mirrors, lenses, and a beam splitter cube. The number of mirrors required to bring the light from the spectrometer to the device may vary with physical set-up. To reach the device, a focusing lens is used beneath the beam splitter. The current generated in the device is measured as a function of the wavelength of the incident light. A CCD camera with a TV monitor may be used to image the devices and insure that the incident light is sampling only one device. A microscope light is helpful for providing sufficient illumination to see the devices with the camera. Devices may be packaged to simplify the process or if the device is unpackaged, the metal contact pads can be probed directly.

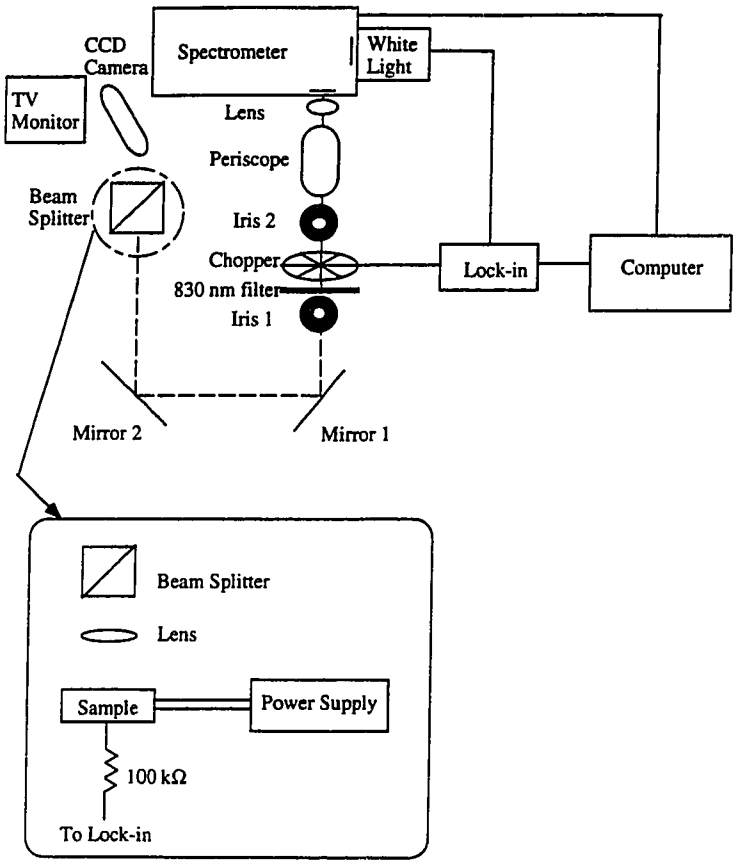

FIGURE 2.7 Schematic of photocurrent measurement set-up.

The power of the incident light is measured using a power meter with appropriate wavelength calibration. The measuring diode of the power meter replaces the sample in the set-up. The value of residual light is subtracted to obtain P_{opt}.

2.5. Summary

This chapter has presented some of the background of this thesis in terms of materials, growth, and devices. It included an introduction to III-V materials, MBE, and two optoelectronic devices: modulators and photodetectors.

3. STRAINED LAYER EPITAXY

3.1. Overview

This chapter reviews the literature most relevant to the focus of this thesis. The first section presents background material on strained layer epitaxy including the essential concept of critical thickness. This is followed by a discussion of studies of the growth and device performance of high In content InGaAs on GaAs. The final section of the chapter details some of the recent work with compositionally graded buffer layers in a related mismatched system, SiGe/Si.

3.2. Critical Thickness

Strained Layer Epitaxy (SLE) is a rapidly growing and active area of research. From its beginnings in 1982 by Gordon Osbourn of Sandia National Laboratories,[60] the field had grown enough by 1991 to merit two volumes in Willardson and Beer's Semiconductors and Semimetals series.[61,62] SLE has been used with a variety of semiconductor materials systems including III-V, Group IV, IV-VI, and II-VI compounds. In 1983, Osbourn first proposed using $In_xGa_{1-x}As/In_yGa_{1-y}As$ strained layer superlattices (SLS) as useful electronic materials.[63] He claimed that using SLS would allow great flexibility in the tailoring of electronic and optical properties through proper choice of materials and thicknesses.

Osbourn essentially recognized that lattice mismatched materials could be stable and might not always have such high defect concentrations as to destroy device performance. If the layers were sufficiently thin, theoretical predictions had shown that the mismatch would be accommodated by uniform strain rather than by misfit dislocations. This thickness is called the critical thickness. The most commonly used and simplest model to describe lattice mismatched epitaxy is known as the Matthews-Blakeslee model[64] and it is illustrated in FIGURE 3.1. For thicknesses below the critical thickness, the mismatch between an epitaxial thin film and a substrate is accommodated by strain in the film. In the case illustrated in FIGURE 3.1, the film has a larger equilibrium lattice constant than the substrate. Thus the lattice constant of the film in the growth plane will be compressed to match that of the substrate. Of course, this is accompanied by the Poisson expansion. This situation is known as compressive strain. If the film were to have a lattice constant smaller than that of the substrate, the film would be strained in tension. This strained configuration results in good quality epitaxial material because no defects are introduced. However, above the critical thickness, the film can no longer accommodate all of the

mismatch by strain so defects, specifically misfit dislocations, are introduced. Far from the interface, the film will be relaxed near its equilibrium lattice constant. Since the interface is now the union of two materials with dissimilar lattice constants, it results in missing half-planes, or dislocations. These dislocations degrade the material quality. Summarizing, the Matthews-Blakeslee model predicts that below the critical thickness, the material quality of the epitaxial film is good while above the critical thickness, the quality is quite poor. A good introduction to the mechanisms of misfit dislocation formation may be found in Nix.[65]

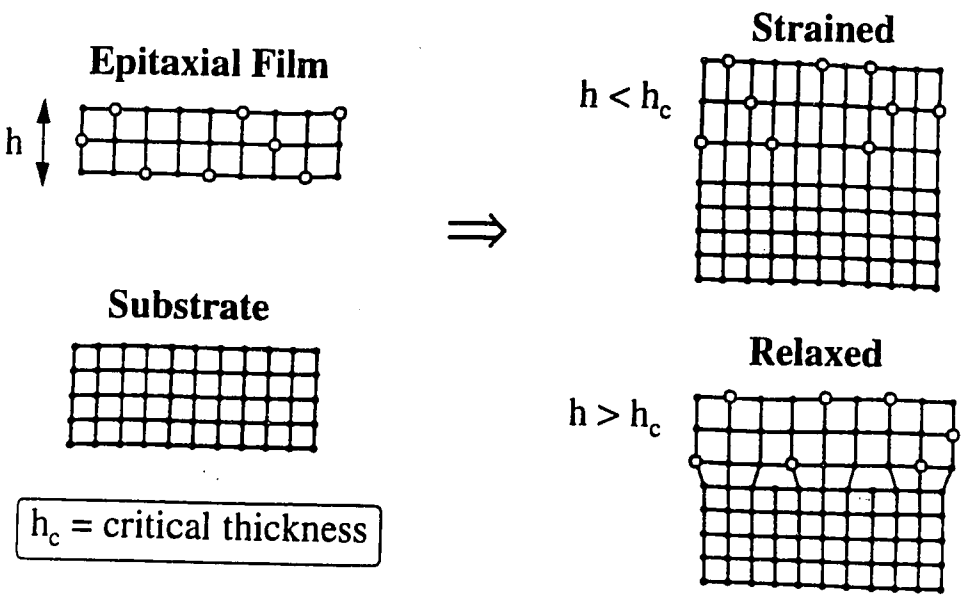

FIGURE 3.1 Schematic illustration of Matthews-Blakeslee model. On the left, the epitaxial film and substrate are shown in their bulk configurations. The top right represents the growth of a strained film while the bottom right shows a relaxed film with misfit dislocations at the film/substrate interface.

The exact growth mechanism of the InGaAs/GaAs system, particularly the role of lattice mismatch, is not well understood. Despite attempts to define the critical thickness for InGaAs/GaAs as a function of In composition[66,67,68,69,70,71] there is still disagreement. Most studies reference the Matthews-Blakeslee critical thickness which was originally developed to describe the critical thickness of GaAs/$Ga_{0.50}As_{0.50}P$ superlattices. The strain, ε, at the critical thickness, h_c, is given by

$$\varepsilon = \frac{a(1-\nu/4)}{\sqrt{2}h_c 2\pi(1+\nu)}(\ln\frac{\sqrt{2}h_c}{a} + 1) \tag{3-1}$$

for InGaAs on GaAs where a is the lattice constant and ν is Poisson's ratio. Exceeding the Matthews-Blakeslee limit is commonly characterized by marked decrease of photoluminescence (PL) signal intensity, increased full-width at half-maximum (FWHM), and a red shift in the exciton peak position. However, it is perhaps most important to describe the thickest strained layer that is useful for devices.[72] It has been proposed[73] that one should consider several thickness thresholds including one that is a transition from 2D to 3D growth or islanding occurring below the Matthews-Blakeslee limit. This regime has yet to be fully characterized and will be discussed in Chapter 4.

Heteronucleation is not well understood. The Matthews-Blakeslee model is a mechanical equilibrium model. Other models have been proposed to describe heteroepitaxy including the People-Bean[74] energy balance model and the Dodson-Tsao[75] relief of strain by plastic flow model. More recent models[76] include an interfacial energy term to account for the observed dependance of critical thickness on temperature which will also be described in Chapter 4. These newer models include 2D growth known as Frank-van der Merwe growth, coherent islanding, and incoherent islanding or 3D growth with dislocations known as Stranksi-Krastanov growth. Theorists continue to develop models to explain the variety of experimental observations.

Determining the exact onset of different growth mechanisms and defining the critical thickness are also complicated by the difficulty of making such measurements and the effect of the measurement technique on the results measured. Since different techniques are sensitive to roughness on different scales, comparisons among techniques are quite difficult.[77]

For the InGaAs/GaAs system and the SiGe/Si system, the {111} is the slip plane. Thus dislocations with Burger's vectors in this plane can easily glide which requires less energy than climb where atoms must be transported. The most commonly observed dislocations are 60° dislocations with Burger's vectors of $\frac{1}{2}[110]$. However, it is only the edge portion of the dislocation which can act to relieve misfit strain. Thus these dislocations are not the most efficient type for relief of misfit strain.

The major obstacle to producing InGaAs that operates at 1.3 μm on a GaAs substrate is that the material will exceed the critical thickness. As the amount of In increases, the critical thickness decreases. Operation at 1.3 μm requires about 33-44% In depending on whether the layers are relaxed or strained. Such compositions have critical thicknesses on the order of 50-80 Å for single layers. The succession of single layers which form a MQW must each be even smaller than this single layer critical thickness. These critical thicknesses are too small to be practical for most device applications. Identifying techniques to overcome this problem of material degradation above the critical thickness is crucial for producing high quality InGaAs which can operate at 1.3 μm on GaAs.

3.3. High In Composition InGaAs on GaAs

This section discusses previous work which relates to the growth and device performance of high In content InGaAs layers on GaAs substrates. Attempts to grow such material include reduced area growth, various buffer layers, and short period superlattices (SPS). Device results in this section concentrate on modulators and photodetectors. The longest wavelength modulation achieved in InGaAs/GaAs prior to this thesis work was only 1.06 μm. Photodetectors operating near 1.3 μm mostly involved bulk layers and are reviewed in the last subsection. Growth schemes reported primarily in connection with device results will be described in the appropriate device section.

3.3.1. Growth

3.3.1.1. Reduced Area Growth

Beam et al.[78] and Fitzgerald et al.[79] have demonstrated the use of reduced area growth for InGaAs on GaAs to avoid the limitations of critical thickness. The impetus for considering reduced area growth is that the probability of dislocation interaction and multiplication is directly dependent on the effective substrate surface area and lattice mismatch.[80] Only when small lattice mismatches and small substrate dimensions are used will the dislocations propagate to the growth edges. Fitzgerald et al. determined that different sources of misfit dislocations became active at different epilayer strain levels. Hence the critical thickness depends on which type of nucleation source activates first. By confining the growth to 2 μm high mesas with varying lateral dimensions and geometries on (001) GaAs, they were able to grow layers of $In_{0.05}Ga_{0.95}As$ that were 3500, 7000, and 8250 Å thick with dislocations densities of 1.5 x 10^5, 10^4, and 10^2 cm^{-2} respectively. These thicknesses correspond to 5, 10, and 11 times the experimental critical layer thickness measured for MBE-grown large-area samples. This demonstrates the potential for growth of highly mismatched layers using reduced area growth.

Beam et al. showed that step-composition grading and linear-composition grading are particularly effective when combined with reduced growth areas up to 30 x 30 μm for In compositions up to 25%. For In compositions between 25% and 53%, they observed that linear grading produced smoother layers than step-grading for growth in 10 μm wide trenches. They were uncertain of the reason for this difference but suggest a rougher growth interface for step-graded layers. In general, their growth of high In composition layers with greater than 25% In resulted in large defect densities and a substantial number of threading dislocations suggesting the beginning of 3D growth. They postulate that linear-composition grading in conjunction with reduced area growth shows the most promise for growth of highly mismatched layers.

Overall, although reduced area growth is very useful for small mismatches such as low In composition InGaAs on GaAs, In reduced area growth alone does not seem to be the solution for growing high quality layers of highly mismatched InGaAs on GaAs. The linear-composition grading alone appears to warrant further investigation. Linear grading will be discussed in the last section of this chapter in the SiGe/Si system and in sample III in Chapter 5 and in samples in the subsequent chapters

3.3.1.2. Buffer Layers

Buffer layers are commonly used in SLE. A buffer is a layer grown on top of the substrate but beneath the active layer. Researchers at the University of Florida have observed that a critical composition exists in the MBE growth of InGaAs on GaAs. Above this composition, 18% In for their growth conditions, dislocations propagate up through the active layers and down toward the substrate. However, below this critical composition, dislocations only propagate downward.[81] They attribute this behavior to the fact that for high In compositions, the surface image force due to strain is high and pulls dislocations up through the epilayers. However, below their critical composition, they believe that the dislocations will propagate in the softer material. As the In composition is increased, the material becomes harder until 53% In at which point this scheme no longer works since the high In content material now becomes softer. Although their initial work emphasized the importance of SLS to enhance the lateral motion of dislocations, they now believe that the SLS are not important.[82] They determine an optimum temperature for the growth of each In composition layer which decreases as In composition increases. Thus they intentionally grow a sacrificial multistage strain relief buffer system. All of the dislocations will reside in these sacrificial layers leaving the top layer suitably free of dislocations to be useful for

devices. To achieve this, it is important to determine the effective In composition in each layer using high resolution X-ray diffraction to compute the amount of relaxation in the layer. This is complicated and involves a good deal of time and materials growth. However, since it initially looked promising, an attempt to duplicate it will be discussed as Sample II in Chapter 5.

Melman et al.[83] attempted to spatially separate portions of the mismatch strain from the quantum well layer using a complicated buffer including SLSs. They relieved part of the strain by having a thick layer of InGaAs with composition x_1 grown well above the critical thickness. A SLS on top of this is designed to terminate the dislocations and isolate them from the quantum well. Next an unstrained layer is grown with composition x_1. This serves as the barrier for the single 60 Å quantum well of composition x_2 grown on top. The sequence of layers from the thick buffer to the barrier is then repeated in reverse order to form a symmetric structure. Thus the strain in the quantum well is due to the difference in lattice constants between x_1 and x_2 rather than x_2 and 0 for the GaAs. They claimed a 1.3-1.4 μm band edge at room temperature using transmission measurements and 15 K photoluminescence (PL). The width of their 15 K PL peak was about an order of magnitude larger than those for low composition quantum wells grown under similar conditions. They attribute this broadening to spatial nonuniformities in the strain and the presence of some dislocations due to incomplete termination of misfit dislocations by the SLS.

3.3.1.3. Short Period Superlattices

Short period superlattices (SPS) are also being investigated for long wavelength emission in InGaAs/GaAs. SPS consist of very thin alternating layers of InAs and GaAs. Typical dimensions are on the order of monolayers. Their use is based on the theory that the bandgap of a SPS is smaller than the corresponding randomly disordered alloy leading to a higher emission wavelength. The SPS is also thought to result in less strain and larger critical thickness than for the random alloy.

Research on SPSs is being conducted in a number of laboratories to investigate the materials growth of such a highly strained system[84,85,86] as well as device applications such as high electron mobility transistors (HEMTs)[87] and quantum well lasers.[88] Roan and Chang[89] demonstrated 1.3 μm room temperature photoluminescence in InGaAs/GaAs strained layer structures grown on GaAs substrates using an InAs/GaAs SPS. There are disadvantages to using SPS. The PL intensity from SPS depends strongly on growth

conditions, such as growth temperature and V/III ratio, thus hampering their reproducibility. SPS require precise control of many shutter openings and closings which could shorten the lifetime of a growth system. These features make SPS particularly unattractive for future production applications. In general, the nature of SPS dictates using particular layer combinations for achieving particular wavelengths and thus limits the flexibility of structures including SPS.

3.3.2. Devices

3.3.2.1. Modulators near 1.06 μm

Devices which operate at 1.06 μm are useful since they coincide with an emission line of Nd:YAG lasers. Thus there have been efforts to use InGaAs/GaAs at this wavelength. A number of interesting techniques have been employed to grow material with sufficiently high In composition and quality to be used as electroabsorption modulators.

Niki et al.[90] observed the quantum confined Stark effect (QCSE) at 1.08 μm for $In_xGa_{1-x}As/GaAs$ grown on a superlattice (SL) buffer with $0.15 \leq x \leq 0.28$. Transmission electron microscopy showed improved morphology for growth on SL buffers than on only a GaAs buffer. This SL buffer consisted of 125 periods of 25 Å InGaAs/25 Å GaAs where the In composition was equal to that of the MQW grown atop it. Under TEM, this SL buffer appeared to confine the misfit dislocations at the SL/substrate interface. This permitted the growth of quantum wells with thicknesses beyond the critical thickness. Their work is based on the belief that for an alternating strained layer structure whose weighted strains are equal but opposite, the structure will remain commensurate if each layer is below the critical layer thickness. They obtained their best results using a two stage buffer layer. The first stage was 5000 Å of $In_{0.13}Ga_{0.87}As$ and the second stage was a 50 period SL of 50 Å $In_{0.25}Ga_{0.75}As$/50 Å GaAs. Dislocations were confined to the ternary alloy layer.[91] They achieved a maximum absorption coefficient change ($\Delta\alpha$) of 5900 cm^{-1}. This is consistent with their earlier work[92] where they examined different buffer configurations to achieve 0.98 μm operation which is useful in connection with Er-doped fiber amplifiers.[93]

Woodward et al.[6] demonstrated $In_xGa_{1-x}As/GaAs$ multiple quantum well optical modulators for the 1.02-1.07 μm wavelength range. They grew samples with and without a strain-relief SL buffer. Samples grown on strain-relief buffers had more sharply defined excitons than those grown directly on GaAs. Greater strain nonuniformity was observed in samples grown directly on GaAs. They also concluded that samples grown on InGaAs

buffer layers showed a trend toward improved behavior with fewer total periods. Strain accommodation led to significant shifts in the band edge so that the samples grown on buffer layers had smaller bandgaps than those grown directly on GaAs due to the larger compressive strain of the wells without buffer layers. Their longest wavelength sample included 100 periods of 100 Å of $In_{0.26}Ga_{0.74}As$ with barriers of 50 Å of GaAs grown at approximately 500 °C by MBE. They demonstrated optical modulation of a Nd:YAG laser via operation of a self-electro-optic effect device (SEED). Relative transmission, $\Delta T/T_0$, of up to 57% was measured for transmission modulators.

Using gas source MBE (GSMBE), Cunningham et al.[7] produced modulators operating near 1.06 μm on GaAs using a novel approach with compressively strained InGaAs quantum wells and tensilely strained InGaP barriers. X-ray diffraction and absorption data confirm that the quality of this strain balanced InGaAs/InGaP material is superior to that of InGaAs/GaAs.[94] They obtained a transmission change from 60% to 80% at 1.014 μm for a sample with a 1 μm thick intrinsic region. A particularly nice feature of their work was the lack of cross-hatching on the surface of their strain balanced structure. However, the use of phosphorus in the barriers precludes using a solid source MBE for the growth unless complex special pumping techniques and/or a valved cracker are employed. More recently, this group demonstrated modulation at exactly 1.06 μm.[95]

Fritz et al.[96] designed a reflection modulator for 1.06 μm and achieved 1.04-1.05 μm operation. During MBE growth, they combined what they termed "mechanically stable" strained and unstrained epitaxial layers. Their structure began with a relaxed buffer of $In_{0.11}Ga_{0.89}As$ consisting of a short period SL of 20 Å $In_{0.23}Ga_{0.77}As$/ 20 Å GaAs used to improve interfacial smoothness followed by a bulk layer of 1710 Å of $In_{0.11}Ga_{0.89}As$. On top of this buffer, quarter-wave mirrors consisting of 753 Å $In_{0.11}Ga_{0.89}As$ and 891 Å of $In_{0.10}Al_{0.90}As$ were grown. The cavity was an $In_{0.23}Ga_{0.77}As/Al_{0.35}Ga_{0.65}As$ SL whose planar lattice constant also matched the buffer. The insertion loss at resonance of their device was about 2 dB with a fractional modulation of over 60% for a 4 V bias swing.

Perhaps the most obvious lesson learned from these reported results is the promise of buffer layers for producing high performance modulators. However the particular techniques employed to increase the In composition or wavelength seem inadequate for reaching 1.3 μm operation. Thus a different type of buffer layer must be found.

3.3.2.2. Photodetectors near 1.3 μm

There has been a fair amount of work aimed at producing photodetectors for 1.3 μm operation with InGaAs on GaAs. Most of these involve the growth of thick strain relaxed epitaxial layers. Tzeng et al.[97] produced a planar $In_{0.40}Ga_{0.60}As$ p-i-n photodiode on GaAs using MBE. The active layer was 0.8 μm thick. The dark current was 2.5×10^{-5} A/cm^2 at 6×10^4 V/cm. The device was produced using steps of 13% In and included superlattices in the underlying sacrificial layers. Warren et al.[98] used a novel scheme involving arsenic precipitates into low temperature grown GaAs (225 °C) to achieve 1.3 μm operation for a p-i-n photodetector. They propose that the arsenic precipitates act as local Schottky barriers. Then the absorption may be explained by internal photoemission from the arsenic into the GaAs. They demonstrated measurable 300 K responsivity for wavelengths out to 1.7 μm. At 1.3 μm, the maximum reported responsivity was roughly 2 mA/W and the internal quantum efficiency was about 2%.

Other groups have investigated interdigitated metal-semiconductor-metal (IMSM) devices. Rogers et al.[99] produced such detectors with 1 μm $In_{0.40}Ga_{0.60}As$ on 0.5 μm $In_{0.25}Ga_{0.75}As$ on GaAs. The device exhibited a 3 GHz bandwidth. Dentai et al.[100] used MOCVD to produce InGaAs p-i-n photodiodes on GaAs substrates. However, their use of a thick InP layer between the GaAs and InGaAs makes it difficult for optoelectronic integration. Elman et al.[101] reported InGaAs/GaAs IMSM photodetectors operational at 1.3 μm grown by MBE with 14 GHz performance for a bulk $In_{0.42}Ga_{0.58}As$ active layer. They used Schottky barrier enhancement cap layers to study thermal stability and device performance as well as oxygen plasma passivation to obtain low dark current.

Zirngibl et al.[102] used InGaAs/GaAs superlattices to produce high speed MSM photodetectors. Grown by MBE at 460 °C, the 200 x 200 μm device consisted of sixty 80 Å $In_{0.64}Ga_{0.36}As$ quantum wells with 50 Å GaAs barriers grown on a GaAs buffer. With a FWHM of less than 50 ps, the device had a dark current of 32 mA/cm^2 at 14.5V. Other devices[103] had one hundred twenty 60 Å GaAs barriers with 60-80 Å $In_xGa_{1-x}As$ wells with x=0.48-0.66 grown at 450-470°C using a minimum As/Ga ratio. These devices had a cutoff of 1.3-1.6 μm and dark currents of 4 mA/cm^2 to 0.1 A/cm^2 at 10V for 2500 μm^2 devices. They also reported internal quantum efficiencies of up to 60%.

The ability to produce high In content InGaAs quantum wells on GaAs substrates should allow for higher performance photodetectors operating near 1.3 μm. These should be able to achieve lower dark currents and sharper cut-offs.

3.4. Si-Ge Graded Buffer Layers

In 1991, several groups reported success in growing another strained system, $Si_{1-x}Ge_x$, using graded buffer layers.[104,105] LeGoues et al.[106] observed what they termed "Anomalous Strain Relaxation" (ASR) characterized by dislocations injected deep into substrate and no threading dislocations reaching the interface of the epilayer. They suggest the Modified Frank-Read Source (MFR) mechanism to explain their observations. This is similar to the well-known Frank-Read Source mechanism[107] where a pinned dislocation under applied stress serves as a source of dislocation loops. However, the MFR involves two dislocations gliding simultaneously on two {111} planes rather than just one. MFR proceeds by having a precursor dislocation formed somehow at the interface, perhaps as a results of particulates. 60° dislocations with the same Burgers vector intersect and an annihilation is observed at their crossing point. This results in two corner dislocations. Their interaction leads to an asymmetric dislocation configuration where one of the corners reduces its total length and removes part of the interfacial strain by gliding toward the substrate. This forms an inclined tip bent toward the substrate. The other corner remains pinned by the interaction and the strain in the epilayer. The inclined tip then serves as the initial stage of the MFR source. The dislocation half-loop grows by gliding along two {111} planes. Since each segment of the corner glides on its own glide plane, the resulting half-loop eventually closes onto itself yielding a whole loop and another initial tip. This whole loop will grow until it intersects with the surface where the misfit can be relieved as the threading segments glide to the edges of the wafer. The mechanism continues with the growth of the remaining tip. The operation of each successive dislocation source repels older ones further down into the substrate resulting in the observed double pile-ups along two {111} planes.

MFR is an energetically costly way to nucleate dislocations and will only operate if no other nucleation mechanism is available. Some sort of compositional grading seems to be necessary for enhancing the lateral motion of existing dislocations. LeGoues et al. assert that the type of grading is not important. The grading may be continuous, stepwise, or a superlattice gradient. However, growth without any grading resulted in a large density of threading dislocations. The grading is believed to play a crucial role in decreasing the number of pinning points and speeding up dislocation motion. There is a minimum distance between pinning points above which activation of a Frank-Read source is energetically favorable. The grading spreads the total number of dislocations necessary to accommodate the lattice mismatch between the top layer and the substrate over the entire graded region. Thus each given plane will have fewer dislocations or a lower density of

pinning positions for a graded layer than an ungraded layer. Alternatively, one could speed up the dislocation motion by growing at high temperatures such as the 900 °C used by Fitzgerald et al. MFR is a dislocation nucleation controlled reaction. In order for it to be activated, a compositional grading and clean growth conditions and initial growth surface are important. There also probably exists a critical gradient above which MFR will not operate. LeGoues et al. estimate this to be somewhere around 2% misfit/μm but caution that it also depends on the composition of the final desired layer.

MFR can act independently of growth technique as it has been observed for both CVD- and MBE-grown material. LeGoues et al. even grew pure Ge with a defect density of only 10^6 cm^{-2} on top of a Si substrate. However, it is worth noting that the total mismatch between Si and Ge is about 4%, considerably less than the total 7.2% between InAs and GaAs. Also, for III-V materials such as InGaAs, the dislocation velocity on all {111} planes is not equivalent. Thus glide may be easier on one set of planes than another. {111}A planes terminate in Group III elements while {111}B planes terminate in Group V elements. Group IV materials such as Si and Ge do not have this asymmetry.[108]

Lefebvre et al.[109] also observed dislocation half-loops in the GaAs substrate for the growth of InGaAs on GaAs. To explain their observations, they use a simple Frank-Read source which is activated after a cross-slip of the inclined tip. LeGoues et al. find this inconsistent with the double pile-ups that they observed. Lefebvre et al. start with the same intersection of 60° dislocations with identical Burger's vectors. They point out that the commonly referenced Hagen-Strunk[110] dislocation multiplication model does not explain the observation of dislocation in the substrate since it asserts that the inclined tip glides toward the epilayer rather than the substrate. If one allows the tip to incline toward the substrate, they believe the rest of the Hagen-Strunk model is consistent with their observations in the InGaAs/GaAs system.

The usefulness of compositional grading was confirmed theoretically by Tersoff.[111] His calculations demonstrated that in graded layers, threading dislocations experience greater force due to larger residual strain. In addition, graded layers result in less pinning because new dislocations are added in regions with no previous dislocations. These two factors contribute to enhanced motion of threading dislocations toward the edge of the sample. Finally the reduced strain deep within the graded layer actually inhibits dislocation nucleation. Thus Tersoff has provided a model to describe the observations in graded layers of suppressed dislocation nucleation and enhanced lateral movement of dislocations.

These compositionally-graded buffer layers seem quite useful for achieving the goal of 1.3 μm operation of devices on GaAs if they can be used to produce high quality, high In content InGaAs. In MBE, this grading would be accomplished by changing the growth rate of a furnace rather than opening and closing shutters as in SPS. This grading technique should be readily adaptable to various growth techniques and thus shows promise for future production.

3.5. Summary

This chapter has presented a sampling of the diverse and interesting work in progress in the field of strained layer epitaxy. Although reduced area growth is useful for lower In content InGaAs on GaAs, it does not seem adequate for achieving the high In content necessary for 1.3 μm operation. Short period superlattices are an interesting option, however, their difficulties with reproducibility, thickness control, and limited flexibility do not make them the best choice. Buffer layers, which have been shown in this chapter to play a crucial role in SLE, seem the most promising. Of the types of buffer layers discussed in this chapter, linearly-graded composition buffer layers have the most potential for achieving 1.3 μm operation in InGaAs on GaAs. The results shown in the SiGe/Si system show significant promise for application to InGaAs on GaAs. Such buffer layers should allow for a variety of structures and devices to be grown atop them.

In addition to the problem of strain, growth of InGaAs on GaAs is also highly dependent on growth temperature. This important parameter will be considered in the next chapter.

4. EFFECT OF GROWTH TEMPERATURE AND In COMPOSITION

4.1. Overview

As mentioned in Section 2.2.2, the growth of InGaAs is strongly dependent on growth temperature. This chapter describes an investigation of the effect of growth temperature and In composition on the growth of InGaAs/GaAs quantum wells. The first section considers growth above and below the In desorption temperature. The second section concentrates on growth below this temperature and investigates the effects of varying both growth temperature and In composition. Using photoluminescence (PL) and transmission electron microscopy (TEM), we provide evidence for an intermediate regime between the fully strained (2D) and fully relaxed (dislocation network) regimes.

4.2. Measurements

PL was performed at 77 K using the 514 nm line an Ar-ion laser. The power density was roughly estimated from measurements of the incident power and the spot size. Cross-sectional TEM analysis was conducted using a Philips EM400 at a 120 kV operating voltage. High resolution TEM was performed on a Philips EM430 at 200 kV. Samples were prepared using the sandwich technique involving mechanical polishing, dimpling, and ion-milling.[112]

4.3. Effect of Growth Temperature

4.3.1. Samples

To investigate the effect of growth above and below the In desorption temperature, identical samples were grown by MBE at 620 °C and 500 °C. The samples consisted of five undoped 75 Å $In_{0.20}Ga_{0.80}As$ quantum wells separated by 1000 Å $Al_{0.15}Ga_{0.85}As$ barriers. The well thickness is below the observed critical thickness for this In composition so no strain effects are expected. The barriers are extremely thick and prevent any coupling effects between the wells.

4.3.2. Results

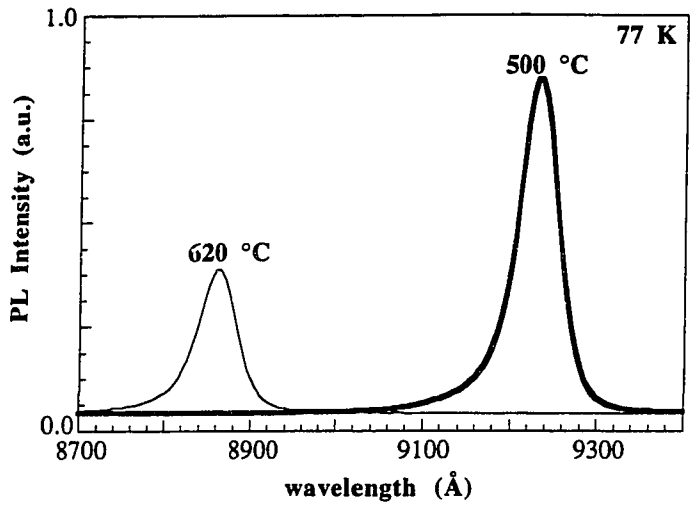

FIGURE 4.1 77 K PL spectra for InGaAs/AlGaAs quantum wells grown at 500 °C and 620 °C.

The 77 K PL spectra from these samples revealed clear differences. The position and intensity of the exciton peak were a strong function of growth temperature as seen in FIGURE 4.1. The lower PL intensity for the higher growth temperature suggests poorer material quality. As the growth temperature was increased, the wavelength of the peak decreased which is consistent with less In being in the quantum wells. There also appears to be considerably more compositional variation across the wafer for the high temperature sample which is reasonable considering that 620 °C is far above the temperature at which In desorbs from the surface during growth. A theoretical fit to the observed data including the necessary adjustment in quantum well width which accompanies a decrease in In concentration gives an estimate of only about 14% In in the quantum wells for the 620 °C sample and 20% In for the 500 °C sample. The In composition varies by as much as 1% In over a 1.5 cm radius in the high temperature sample. The 500 °C sample showed only about one quarter of this variation.

4.3.3. Discussion

Thus our experiments confirm those of others that growth above the 550 °C In desorption temperature results in poor quality material and poor uniformity. These results agree with those of several published studies describing the activation energy for In desorption from InGaAs during MBE growth.[113,114] A value of about 2 eV seems appropriate for the

activation energy.[115] The temperature dependence of the growth of InGaAs suggests that the activation barriers for dislocation nucleation and motion are functions of temperature.[116] Also at higher temperatures, the morphology degrades as a result of being close to the critical thickness. This degradation may be due to In segregation or In riding the surface.[117] Lower temperatures tend to promote complete surface coverage and thus yield smoother films.[118]

4.4. Effect of In Composition and Growth Temperature

4.4.1. Samples

For this study, two samples were grown which contained four undoped 30 Å $In_xGa_{1-x}As$ quantum wells with x=0.2, 0.3, 0.4, and 0.5, where the highest In composition well was grown closest to the substrate as shown in FIGURE 4.2. This order was chosen to permit observation of the PL signal from all quantum wells since the bandgap decreases as In concentration increases. This well width was chosen to be large enough that interface roughness would not dominate but small enough that several different In compositions could be grown without exceeding the Matthews-Blakeslee limit. 300 Å GaAs barriers between the quantum wells were designed to prevent propagation of strain up through the layers and to minimize interaction between quantum wells. Low growth rates were used with In remaining at 0.12 μm/h and the maximum InGaAs growth rate being 0.6 μm/h. Samples were grown below the In desorption temperature at 535 °C and 490 °C as measured by the substrate thermocouple.

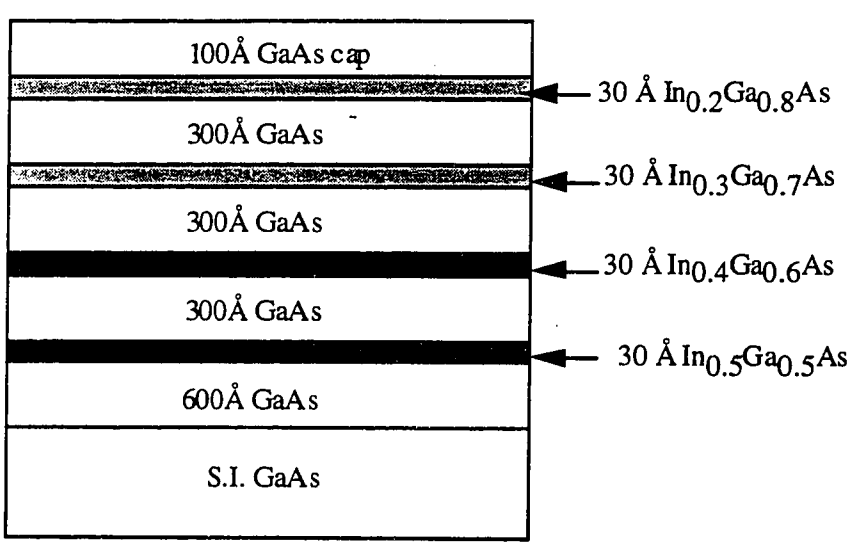

FIGURE 4.2 Schematic of MBE-grown samples used to study effect of growth temperature and In composition.

4.4.2. Results

4.4.2.1. Transmission Electron Microscopy (TEM)

The results of cross-section TEM analysis of samples grown at 490 °C and 535 °C are shown in FIGURES 4.3a and 4.3b, respectively. Both were taken under conditions of strong diffraction which enhances strain contrast. These images illustrate that growth at lower temperature produces smoother layers and is consistent with findings that the critical thickness depends on substrate temperature.[69,72] FIGURE 4.3a shows smooth homogeneous layers for the quantum wells. Only the 50% In well shows some roughening. FIGURE 4.3b shows considerable nonuniformities which could be evidence of islanding for the higher In composition layers. The reduced interdiffusion at lower temperature may explain the flatter interfaces.[119] High resolution TEM analysis performed on the 535 °C sample showed that the bottom surfaces of the InGaAs layers were flatter than the top surfaces for higher In compositions and some evidence of islanding within the quantum wells. No dislocations were visible in either sample. However, one has to be careful in drawing the seemingly "logical" conclusion that there are no dislocations because TEM samples only a very small area.

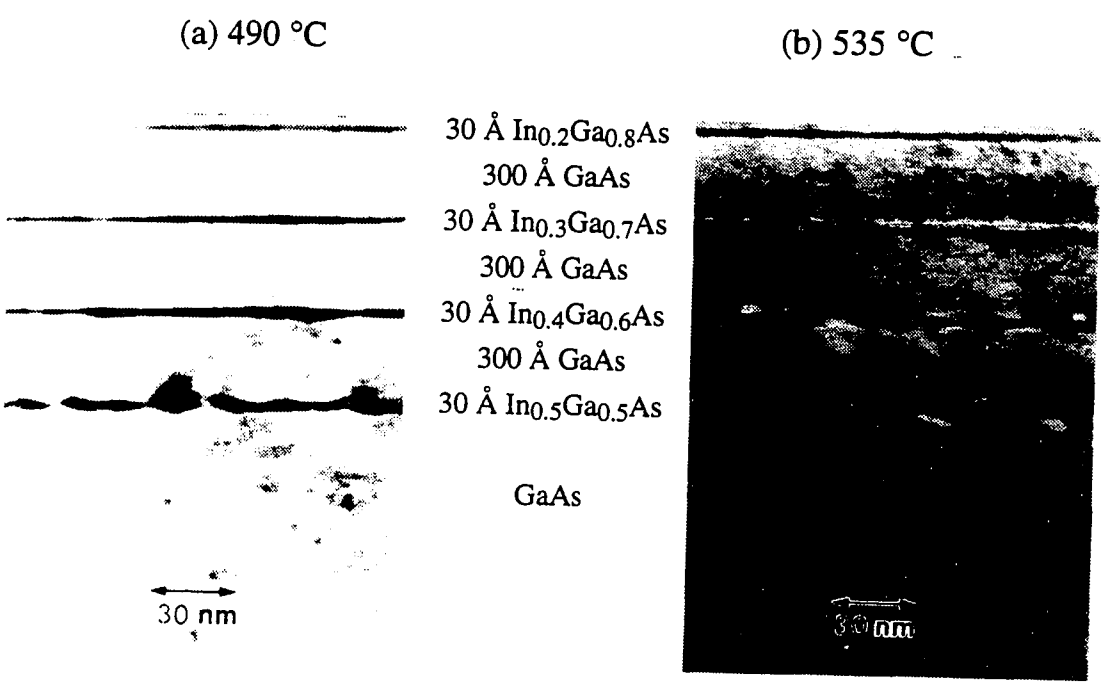

FIGURE 4.3 Cross-section TEM images of $In_xGa_{1-x}As$ quantum wells with x=0.2, 0.3, 0.4, and 0.5 grown at (a) 490 °C and (b) 535 °C.

4.4.2.2. 77 K Photoluminescence (PL)

FIGURES 4.4a and 4.4b show the 77 K variable power PL spectra for samples grown at 490 °C and 535 °C. Having data at various excitation power densities is useful for elucidating the origins of the peaks. Peaks from intrinsic features, such as excitons, should increase in absolute intensity as the excitation power increases but the intensity divided by the excitation power should stay fairly constant. However, due to their lower concentration, extrinsic features, such as defects or islands, should saturate as the excitation power increases and the energy of the peak can also shift with increasing power.[70]

The shape and power dependence of the PL spectra are strong functions of growth temperature. While the shape of the 490 °C spectra in FIGURE 4.4a does not seem dependent on excitation power, that of the 535 °C spectra in FIGURE 4.4b definitely depends on power. For In compositions greater than 0.3, a high energy bump becomes more prominent at higher power densities. This is inconsistent with its being defect-related. Thus the two peaks observed below 1.3 eV in FIGURE 4.4b at the lowest excitation power are probably not exciton peaks but are defect-related and the bumps which emerge to the right of these peaks at higher powers (marked by E in the figure) are the excitons. The extrinsic features saturate relative to the exciton peak as the excitation power is increased, thus making the excitons more visible.[120] Similar behavior has been observed by Anderson et al.[121] in 68 Å and 103 Å 28% In wells grown at 520 °C and Andersson et al.[68] in 30 Å wells with 36% In. Like Andersson et al., we believe that the significant PL intensity from the high In wells with defect structure implies that the defects are not all dislocations which would drastically reduce carrier lifetimes but other defects which localize the excitons such as fluctuations of the quantum well width due to 3D islanding. Wang et al. attribute the behavior to In segregation.[122] This structure's dependence on In composition and growth temperature suggest a change in growth mechanism in this materials system. Along with the TEM results, PL shows that as the In composition increases, InGaAs/GaAs quantum wells do not simply go abruptly from being fully strained with no dislocations to being fully relaxed with a misfit dislocation network. Rather, the structures pass through an intermediate regime which is characterized by defect-related features in the PL spectra and roughening observable in TEM.

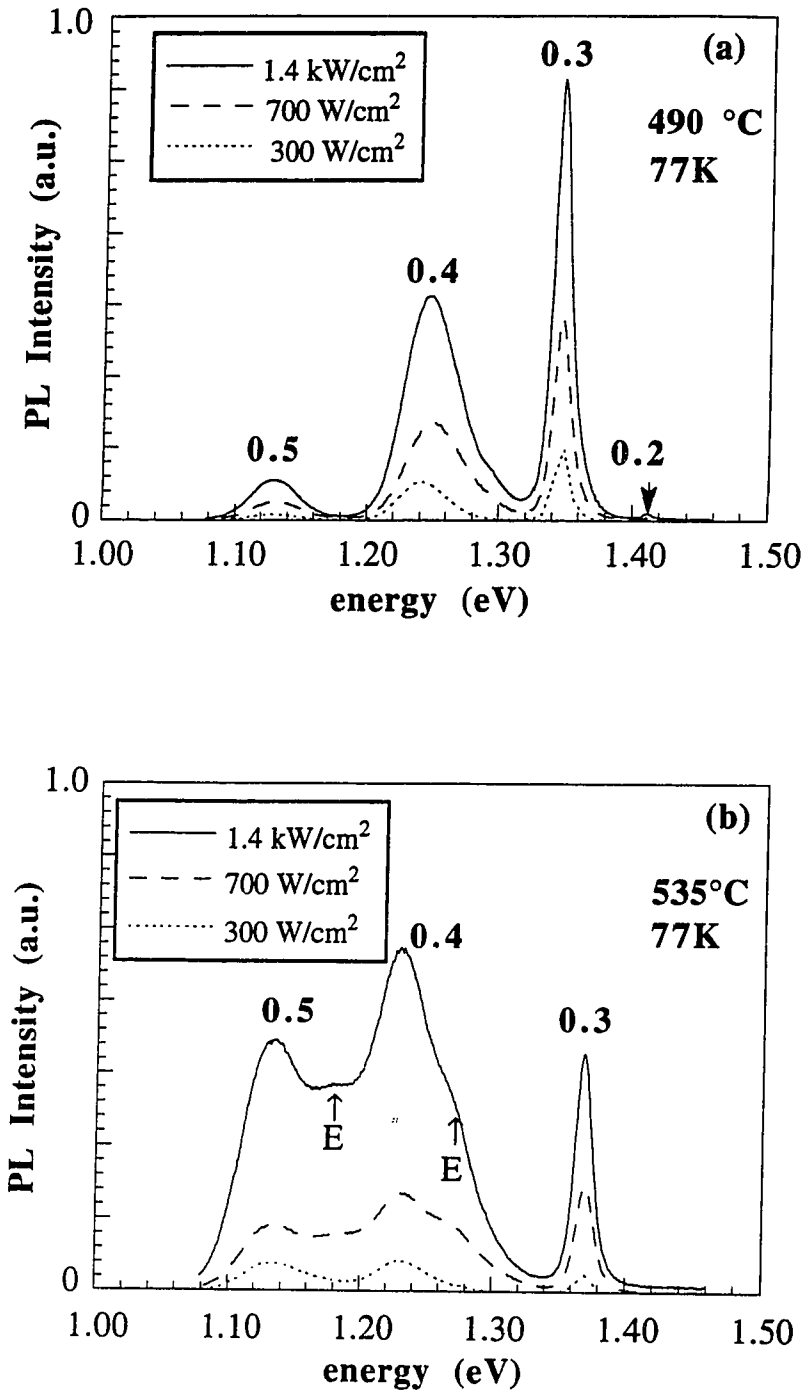

FIGURE 4.4 77 K variable power PL spectra for samples grown at (a) 490 °C and (b) 535 °C. E indicates estimated exciton energies.

No significant shift in energy of any of the peaks was observed as a function of excitation power. PL spectra shifts were all less than 50 Å. Such behavior is believed to demonstrate homogeneous 2D growth with high interfacial quality. This seems a questionable conclusion here. These results are in contrast to the results of Ekenstedt et al.[69] who observed a 150 Å blue shift as power went from 0.4 kW/cm^2 to 1 kW/cm^2 for a 30 Å quantum well with 36% indium. They categorized this blue shift as evidence of islanding. However, perhaps this blue shift included the saturation of extrinsic defects and the consequent dominance of the exciton peak. Thus islanding may not always be marked by a simple blue shift of the exciton peak.

4.4.3. Discussion

These results may be compared to theory using the following relationship for the intrinsic exciton transition energy in a quantum well:[123]

$$E_{PL} = E_{gbulk} + \Delta E_{gstrain} + E_{ec} + E_{hc} - BE \qquad (4\text{-}1)$$

where all values are given in eV and E_{PL} is the energy of the PL peak i.e. the exciton transition energy, E_{gbulk} is the bulk or unstrained bandgap, $\Delta E_{gstrain}$ is the change in bandgap induced by strain, E_{ec} and E_{hc} are the electron and hole confinement energies respectively, and BE is the exciton binding energy. This formula assumes that intrinsic features dominate the PL emission. The 77 K bulk bandgap of $In_xGa_{1-x}As$ is taken from Equation 2.6 and the change in bandgap due to strain from Equation 2.7. The exciton binding energy is taken to be a constant of 0.09 eV. A GaAs heavy hole effective mass $0.62m_0$ and a conduction band discontinuity of 60% is used. Electron and hole confinement energies are estimated using an envelope approximation.

FIGURE 4.5 compares the theoretical exciton transition energy as a function of In composition for both the fully strained and fully relaxed (where the bandgap is simply the bulk bandgap) cases with the observed data from PL.

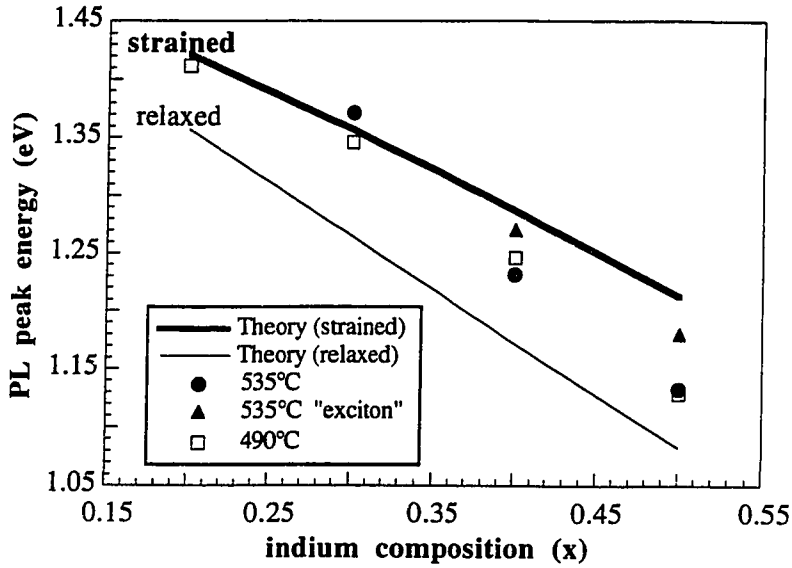

FIGURE 4.5 Exciton energy versus indium composition. Theory is shown as lines for fully strained (heavy line) and fully relaxed (light line) cases. Data for samples grown at 490 °C and 535 °C is indicated by solid and open symbols, respectively.

For In compositions less than or equal to 0.30, it seems reasonable to say that the wells are fully strained and thus in the 2D growth mode. The variations observed from theory could easily be accounted for by uncertainties in growth rates. However, for In composition greater than 0.3, the layers appear to be partially relaxed. For 60 Å quantum wells, Elman et al.[124] observed a sharp transition from fully strained to fully relaxed above 30% In. Only their 30% In sample appeared to be partially relaxed. They postulate the existence of a transition region where partially relaxed regions containing a low density of dislocations can coexist with strained regions. Such a transition region appears to be a plausible explanation for the results at high In compositions presented in this chapter. The estimated positions of the excitons for In compositions of 0.4 and 0.5 in FIGURE 4.4b are shown in FIGURE 4.5 as triangles. These show better agreement with the theoretical strained value, confirming the likelihood of their being the excitons and the other peaks being a defect which contributes to the red shift of the PL energy. However, it is difficult to precisely resolve the peaks due to the overlap of signals from neighboring wells. The red shift from theory of the 50% In wells grown at 490 °C suggests that there may be some relaxation involved in this case too. Based on thermodynamic arguments, Berger et al.[125] suggest that in a strained system, the minimum free-energy surface is more 3D than 2D. This is

consistent with our results that the 3D regime is more pronounced at higher growth temperatures where atoms have more surface mobility to move to minimum energy positions.

It is difficult to draw conclusions based on the relative intensities of the peaks on a given sample due to the inherent complications from surface or position effects, carrier capture between quantum wells, and effects of the measurement setup itself. FWHM values generally increase as In composition increases. This broadening is evidence of some relaxation consistent with the results shown in FIGURE 4.5. However, for applications not requiring narrow linewidths, the emission from these higher In content wells could be useful. The defect structure observed in the wells grown at higher temperature limits their application to devices. Quantum wells grown at lower temperature would be easier to incorporate.

4.5. Conclusions

TEM and PL were used to examine InGaAs/GaAs quantum wells with varying In composition and growth temperature. These measurements show a dependence of growth mechanism on growth temperature and In composition. Growth above the In desorption temperature yields poor composition control and poor material quality. However, even below this desorption temperature, lower growth temperatures yield higher quality material. The study of material grown at 490 °C and 535 °C illustrates the existence of an intermediate growth regime below the Matthews-Blakeslee fully relaxed limit but above the planar growth limit. The studies in this chapter emphasize the importance of growing at low temperatures in order to achieve good morphology for high In content layers. The InGaAs material described in subsequent chapters will all be grown at low temperatures. Growth at low temperatures may result in some problems with poor carrier transport due to high resistivity perhaps from a high density of nonradiative recombination centers.[126] However, this is not always a serious limitation. Heterojunction bipolar transistors (HBTs), minority carrier devices which are quite sensitive to defects, have been successfully grown at low temperatures.[127]

5. STEP-GRADED VS. LINEARLY-GRADED BUFFER LAYERS

5.1. Overview

In this chapter, different buffer layer configurations will be investigated for use in producing good quality high In content InGaAs on GaAs substrates. The first section discusses the structure and MBE growth of samples with both step-graded and linearly-graded buffers. The next section considers the materials characterization of the samples by various techniques including microscopy, electron microprobe, optical absorption, photoluminescence, X-ray diffraction, and SIMS. Finally, the device performance of the linearly-graded sample as an electroabsorption transmission modulator and a photodetector will be reported.

5.2. Structure and MBE Growth

For this study, samples were grown on semi-insulating GaAs substrates by MBE using As_2. Schematics of the targeted structures are shown in FIGURE 5.1. An n-type buffer layer was grown atop a 500 Å GaAs buffer layer grown at 620°C to optimize material quality. Then the substrate temperature was lowered for the subsequent growth to 480 °C for Samples I and II and 450 °C for Sample III. All of the samples had identical multi-quantum wells (MQW) designed to reach 1.3 μm operation at room temperature. These MQW consisted of thirty 75 Å $In_{0.50}Ga_{0.50}As$ quantum wells with thirty-one 35 Å $Al_{0.33}Ga_{0.67}As$ barriers. InGaAs/AlGaAs was chosen rather than InGaAs/GaAs due to the superior electroabsorption properties which will be described in Chapter 7. The average In composition in this MQW is 34%. To complete the p-i-n structures, 5000 Å of p-type $In_{0.34}Ga_{0.65}As$ or $In_{0.35}Ga_{0.66}As$ was grown on top.

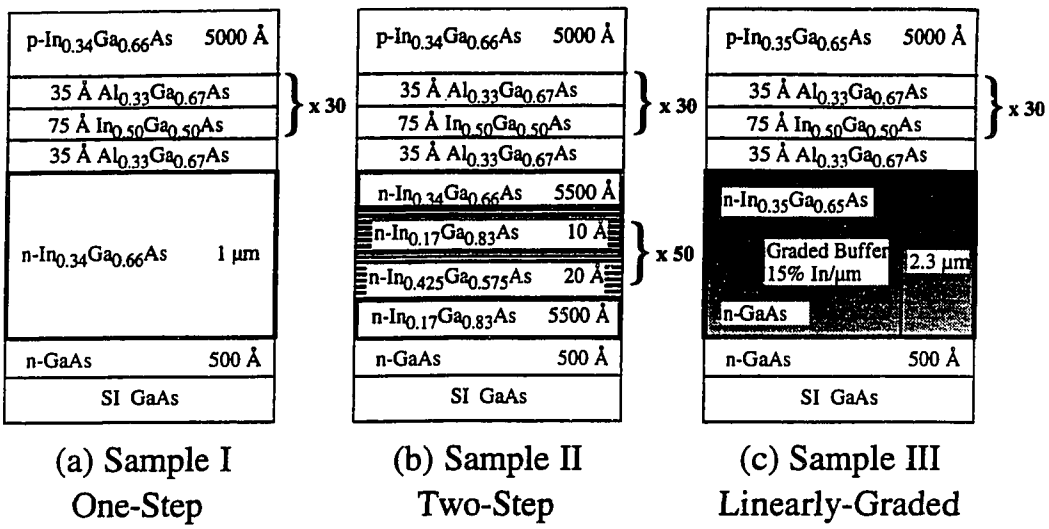

(a) Sample I One-Step (b) Sample II Two-Step (c) Sample III Linearly-Graded

FIGURE 5.1 Schematic of MBE-grown structures with various n-type buffer layers.

Each of these three samples is distinguished by the form of its n-type buffer layer. As described in Chapter 3, the problem with producing InGaAs of sufficiently high In content to operate at 1.3 µm on a GaAs substrate is the large lattice mismatch involved in the growth. So if there were a way to effectively decrease this mismatch, the growth should be of higher quality. The simplest approach to doing this is illustrated in Sample I (one-step) whose buffer is 1 µm of $In_{0.34}Ga_{0.66}As$. This thickness is clearly beyond the critical thickness and the material quality of the buffer itself is not expected to be good. However, if the material is fully relaxed to the lattice constant of 34% In at the top, then the MQW grown on top of this buffer will have an effective mismatch of only 16% (from 50% to 34%) rather than 50% (from 50% to 0% or GaAs). This approach used in Sample I involves a large abrupt change in In composition from 0% to 34%. In an attempt to lessen the shock of such a change to the system, Sample II (two-step) had a buffer which increases in In composition in two steps of 17% In each. The buffer begins with 5500 Å of $In_{0.17}Ga_{0.83}As$ followed by a filtering superlattice of 50 x 10 Å $In_{0.17}Ga_{0.83}As$/20 Å $In_{0.425}Ga_{0.575}As$ and then another 5500 Å of $In_{0.35}Ga_{0.65}As$. Each step was chosen to be 17% In based on the findings of Ribas et al.[81] that dislocations in InGaAs/GaAs will propagate down rather than up for steps of ≤ 18% In. In that report, the authors also stressed the importance of using a filtering superlattice.

Sample III has the most gradual increase in In composition of the three samples. For Sample III (linearly-graded), the In composition in the InGaAs buffer was graded from 0% to 35% at a rate of 15% In/µm.[128] This grading was targeted to be linear and involved

ramping only the In and Si sources. Two gallium sources were used-one for growth of the graded buffer layer and the other for growth of the quantum well region. The graded buffer actually began by increasing the temperature of the In furnace from idle to required for growing $In_{0.025}Ga_{0.975}As$. The temperature was held steady until 0.17 μm of $In_{0.025}Ga_{0.975}As$ was grown. Then the In temperature was increased and 0.17 μm of $In_{0.05}Ga_{0.95}As$ was grown.[129] After that, growth proceeded in 50 Å increments increasing the In concentration by about 0.075% per increment until reaching 35% In. Finally, 150 Å of 35% In was grown to allow the furnace to stabilize at this growth temperature. Attempting a true linear grading is very complicated in MBE where one controls the temperature of the furnaces as compared with gas phase techniques, such as MOCVD, where mass flow controllers can be programmed to provide linear grading. In MBE, the relationship between the temperature T in K, and the flux is given by

$$\text{flux} = A\, e^{-B/T} \tag{5-1}$$

where A and B are constants. Thus one must control the furnace temperature logarithmically to achieve a linear increase in the flux and hence the growth rate and composition.

Several features of the growth merit discussion. As_2 was chosen because improved surface morphology has been demonstrated for MBE growth of InGaAs on InP with As_2 versus As_4.[130] As_2 may also be beneficial at the low substrate temperatures employed during growth since As_2 incorporates more efficiently than As_4 as described in Chapter 2. Since less energy is available to break As_4 bonds at lower substrate temperatures, the As_2 is preferable. Low substrate temperatures are particularly important for the successful growth of high In compositions as described in Chapter 4. Also, the entire buffer region in Sample III is considerably thicker than that of Samples I and II which may affect its role with respect to dislocations. If the buffers are fully relaxed at the top i.e. with a lattice constant corresponding to the targeted 34% or 35% In, the MQW should be symmetrically strained with the InGaAs quantum wells under compressive strain and the AlGaAs barriers under tensile strain.

5.3. Materials Characterization

5.3.1. Microscopy

5.3.1.1. Scanning Electron Microscopy (SEM)

Considerable variation is apparent in the surface morphologies of these samples as observed in optical and scanning electron microscopy. FIGURE 5.2 shows SEM images of the surface. The surface of Sample I is extremely rough with no visible distinct features. The surface of Sample II is also quite rough, however it shows evidence of the cross-hatching which is characteristic of highly mismatched epitaxy. The surface of Sample III shows considerable cross-hatching, however, the area in between the dislocation lines appears fairly smooth in comparison with that of Sample II.

(a) Sample I
One-Step

(b) Sample II
Two-Step

(c) Sample III
Linearly-Graded

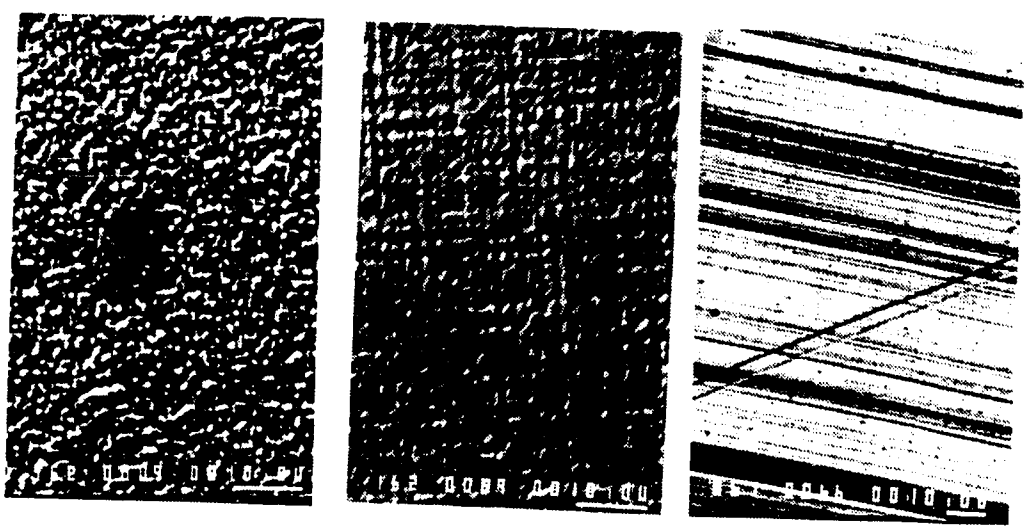

FIGURE 5.2 SEM images of surfaces of (a) Sample I, (b) Sample II, and (c) Sample III. White line on picture indicates 10 μm.

5.3.1.2. Transmission Electron Microscopy (TEM)

Cross-sectional TEM analysis was conducted using a Philips EM400 at 120 kV. High resolution TEM was performed on a Philips EM430 at 200 kV. Samples were prepared as in Chapter 4.

A dramatic difference is observed between the MQW grown atop the step-graded buffers and atop the linearly-graded buffer as shown in FIGURE 5.3. While the MQW in Samples I and II are quite rough, the MQW in Sample III exhibit smooth interfaces. For quantum wells with such high In content, these interfaces look particularly good. A high resolution TEM image in FIGURE 5.4 shows that the interfaces are flat to within two atomic layers.

No evidence of islanding, 3D growth, or clustering is visible. The 75 Å-thick quantum wells exceed the Matthews-Blakeslee critical thickness and would result in a rough morphology if grown directly on GaAs. Thus the linearly-graded buffer has enabled more In to be added without degrading material quality. In the two step-graded samples, many vertically-propagating or threading dislocations are observed above and below the MQW. In contrast, in FIGURE 5.3c no dislocations are visible within about 3400 Å beneath the MQW. Deeper into the linearly-graded buffer, although many dislocations are visible, none within the observable area are threading dislocations which would destroy material quality and device performance. Dislocations within the buffer do not necessarily degrade device performance. In fact, even heterojunction bipolar transistors (HBTs), minority carrier devices which are quite sensitive to defects, have been shown to be fairly insensitive to dislocations deep within the collector.[131]

(a) Sample I One-Step | (b) Sample II Two-Step | (c) Sample III Linearly-Graded

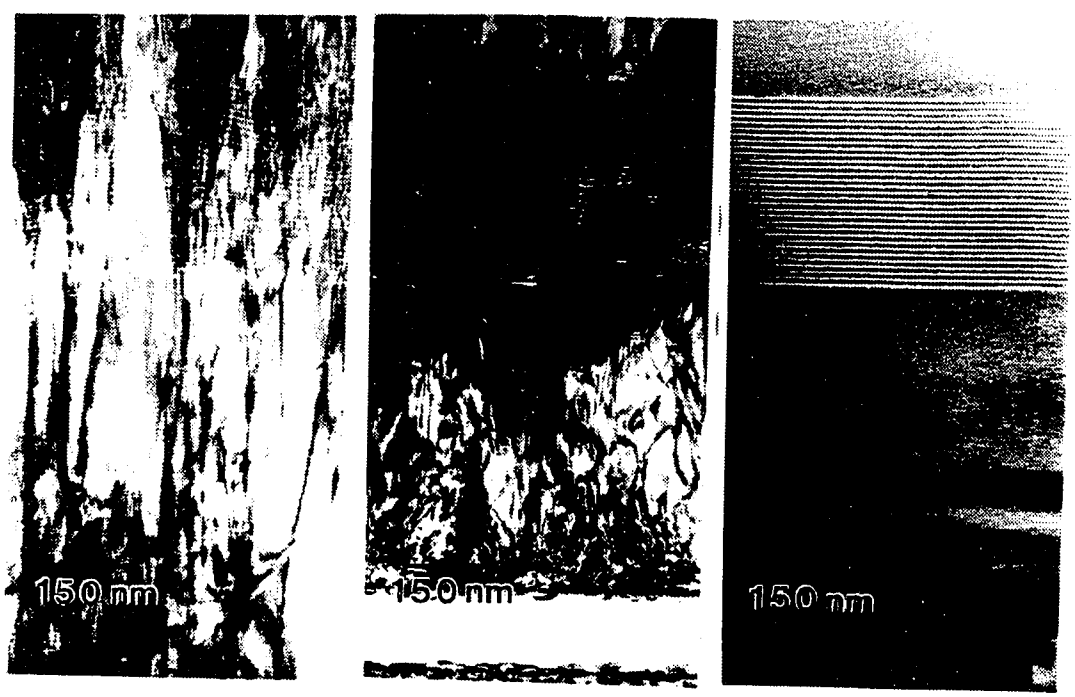

FIGURE 5.3 Cross-section TEM images of (a) Sample I, (b) Sample II, and (c) Sample III. From the top, some of the p-type layer, the entire MQW, and the top of the n-type buffers are visible.

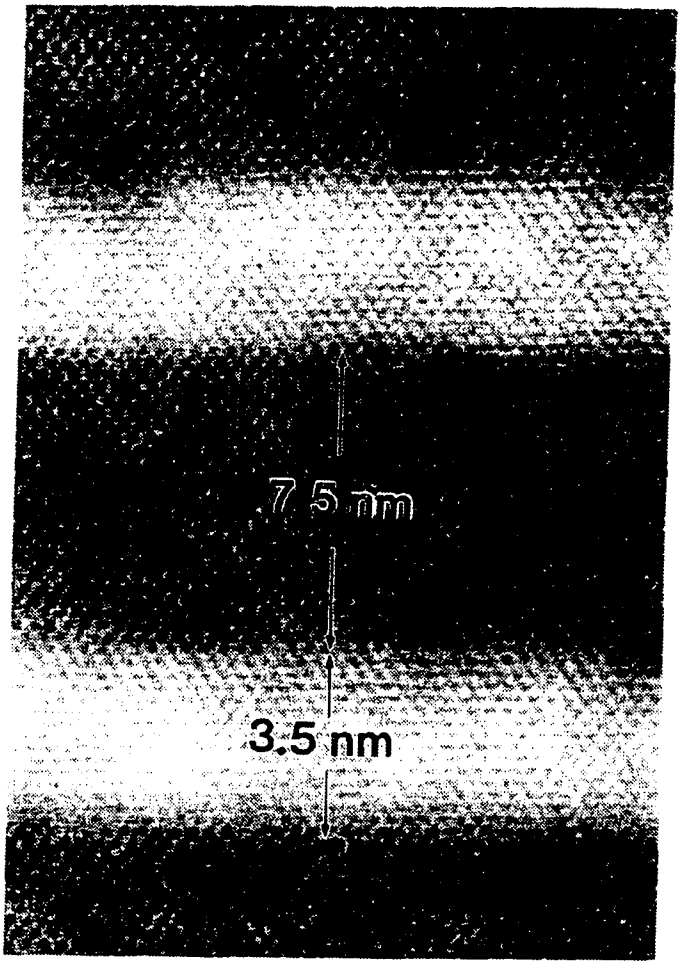

FIGURE 5.4 High resolution TEM image of MQW grown atop a linearly graded buffer.

FIGURE 5.5 shows Sample III from the GaAs substrate to just above the MQW. Many dislocations propagating parallel to the growth interface are visible. Misfit may be accommodated either by the nucleation of new dislocations or the extension of the line length of existing dislocations. Thus the presence of relatively few dislocations with long line lengths suggest efficient misfit relief through increasing line length and suppression of dislocation nucleation. Although a few dislocations are visible in the substrate, no dislocation loops such as those described by LeGoues et al.[106] were observed. This growth in Sample III appears to be experiencing a similar mechanism to that reported in SiGe by LeGoues et al. in that no threading dislocations are visible. However, we can not confirm that dislocations are propagating down into the substrate.

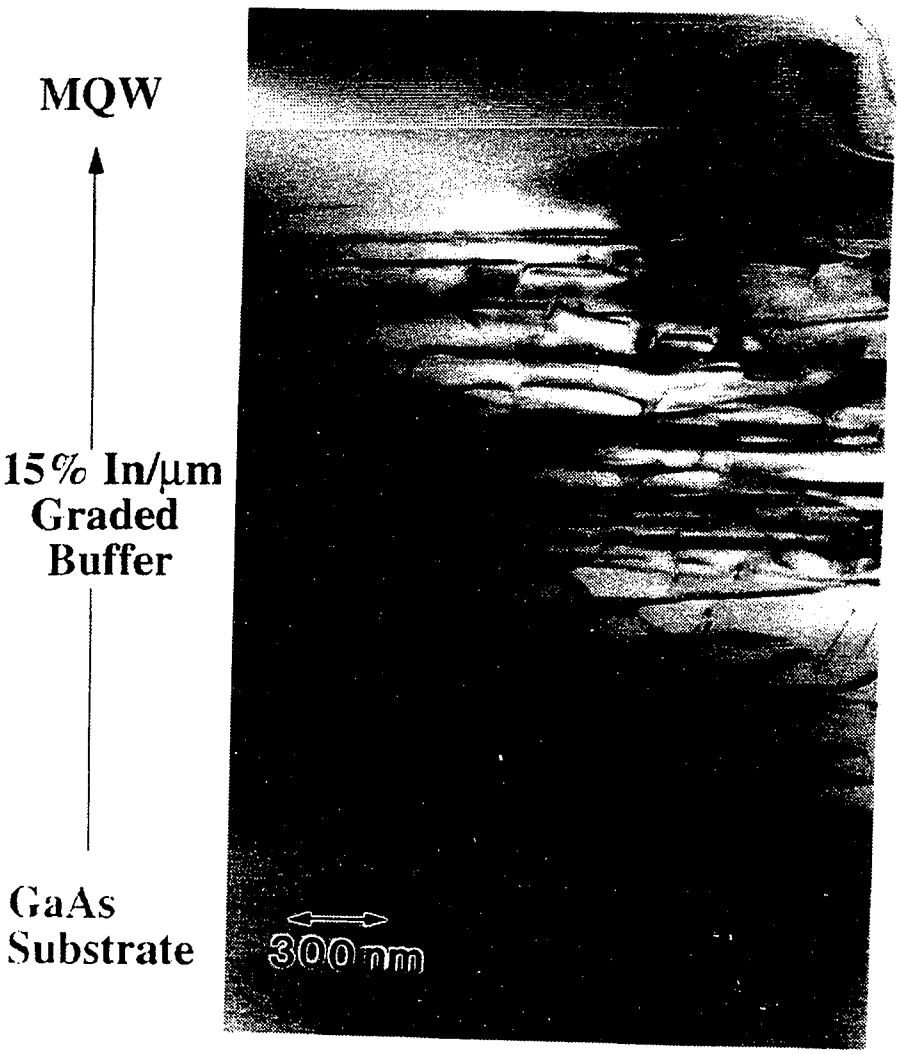

FIGURE 5.5 Cross-section TEM image of Sample III showing an area from the GaAs substrate at the bottom of the image up to just above the MQW. (The distortions in the top right corner are thickness contours due to proximity to the hole in the TEM sample.)

5.3.2. Electron microprobe

Electron microprobe analysis was performed at 15 keV and 40 degrees resulting in a penetration depth of about 4000-5000 Å. Thus this measurement indicates the composition of only the top p-type cap layer. Microprobe analysis on Sample I and Sample II indicated compositions of 33% and 34% In, respectively. Sample III was shown to be 29% In rather than the targeted 35%. This difference could be due to uncertainties in the In growth rate. Achieving 29% In when targeting 35% would mean that the flux was only 83% of what was intended. This large discrepancy could be due to the repeated changing of the In furnace temperature during the linear grading. If the In flux were assumed to remain a constant 17% low throughout the structure, we would expect only 41.5% In in the quantum wells rather than the targeted 50%.

5.3.3. Zero Field Optical Absorption

Room temperature optical absorption spectra at zero bias for Sample III with the linearly-graded buffer layer is shown in FIGURE 5.6. FIGURE 5.7 shows the corresponding spectra for Samples I and II. The absorption coefficient (α) was calculated from transmission measurements as described in Section 2.3.1.5. The nonzero α after the peak may be due to variation in the thicknesses of GaAs wafers and uncertainties in the surface reflection. Samples I and II have spectra which are similar to those from bulk samples in showing only a gradual dependence on wavelength and no distinct features or peaks. However, for Sample III, an exciton is clearly visible at 1.27 μm under zero bias. The absorption per well is estimated to be 1.1% which is comparable to that of the best GaAs/AlGaAs quantum wells.

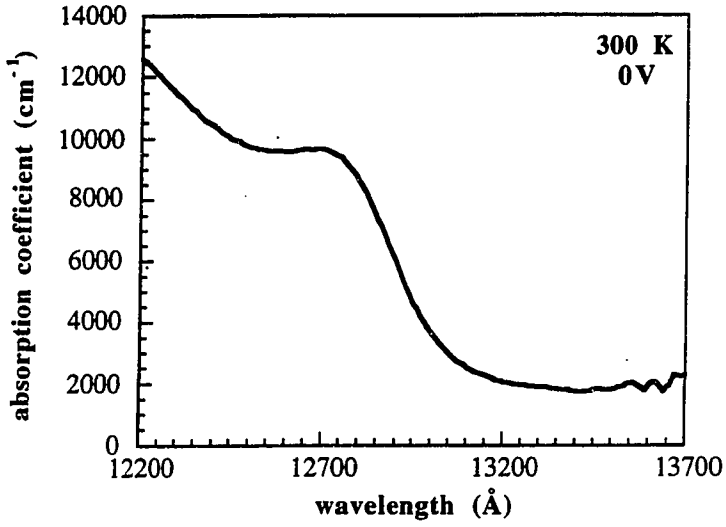

FIGURE 5.6 300 K absorption spectra for Sample III at 0V.

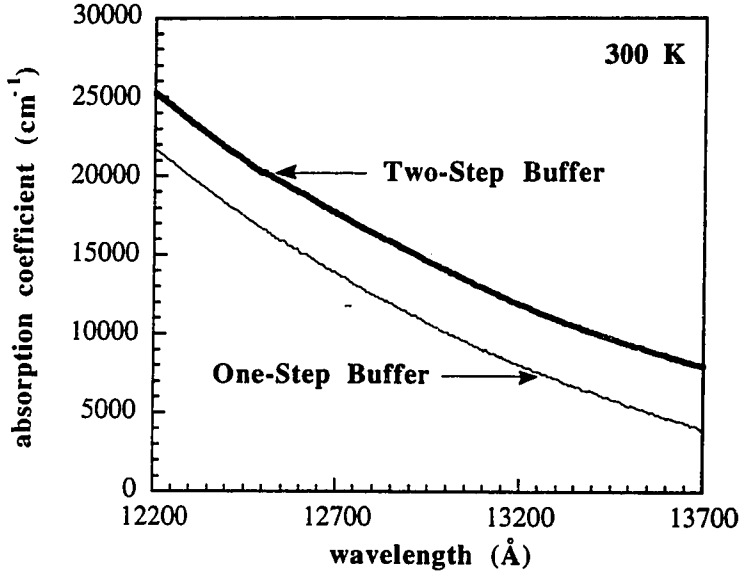

FIGURE 5.7 300 K absorption spectra for Sample I (one-step buffer) and Sample II (two-step buffer).

The In composition of the MQW in Sample III may be estimated from the zero field absorption spectra using the analysis described in Section 4.4.3. The peak occurs at 12700 Å or 0.9764 eV. The electron confinement energy is about 0.07 eV and the hole confinement energy about 0.008 eV using envelope approximations. This yields values of 41% and 38% In for MQW grown atop 35% and 29% In buffers, respectively. Small errors in the spectrometer calibration could have significant effects on the determination of the In concentration. For example, a 190 Å error in the peak determination corresponds to an error of about 2% In.

5.3.4. Photoluminescence (PL)

77 K PL was performed on Sample III. FIGURE 5.8 shows the PL spectrum for the as-grown sample as a heavy line. The luminescence from the 5000 Å p-type top layer dominates the spectrum. Assuming the layer is fully relaxed and thick enough to act as bulk, the exciton peak at 11710 Å or 1.059 eV corresponds to an In concentration of 33% using Equation 4-2 for the bandgap of InGaAs at 77 K. To observe the PL from the MQW, most of the top layer was removed by chemical etching. The spectrum for the sample after this etch is shown in as a light line in FIGURE 5.8. The peak in the etched sample occurs at a lower wavelength than that of the unetched sample which is consistent with it being from the MQW which are higher in In content that the top layer. The exciton peak at 12030 Å or 1.031 eV corresponds to 35% In for a bulk sample. Using the analysis described in Section 4.4.3 (Equation 4-1), with an electron confinement energy of 0.07 eV, a binding energy of 0.01 eV, and a hole confinement energy of 0.01 eV, the In concentration in the MQW is calculated to be roughly 45% In if the graded buffer is assumed to be relaxed to the lattice constant of 35% In. If the buffer is taken to be 29% In, then the MQW are calculated to be 48% In . Of course, this PL analysis depends on the temperature remaining at 77 K and there is uncertainty in the values for bandgap, strain, confinement energies, and exciton binding energy. Also, since some evidence of the top p-type layer is seen in the etched layer, this may affect the accurate determination of the exciton peak from the MQW.

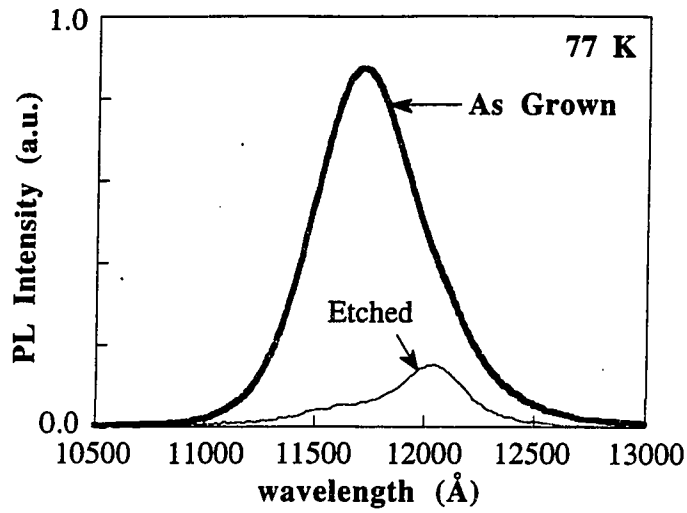

FIGURE 5.8 77 K PL spectra for Sample III for as-grown structure (heavy line) and after etching (light line) to remove top p-type layer.

5.3.5. X-ray Diffraction

X-ray diffraction was performed using a Picker Cu powder diffractometer. FIGURE 5.9 shows the X-ray spectra for the three samples. The GaAs substrate contributes the strongest peak in all three spectra, as expected, and appears as a double peak due to the diffraction from the $K_{\alpha 1}$ and $K_{\alpha 2}$ Cu lines. Peaks which do not appear as double peaks are actually quite broad. So the appearance of double peaks corresponds to higher quality material. Satellite peaks due to the presence of a periodic superlattice are visible on all spectra. However, the spectra from the linearly-graded sample clearly look the best. Given the TEM results described in Section 5.2.1.2, it is not surprising that the linearly graded sample shows the best MQW. In fact, it is perhaps more surprising that the step-graded samples show any periodicity at all. From the spacing between the satellite peaks, one may calculate[132] the MQW period (L) using

$$\pm \frac{n}{L} = \frac{2\sin\theta_n - 2\sin\theta_{SL}}{\lambda_{Cu}} \tag{5-2}$$

where n is the order of the satellite peak, θ_{SL} is the central or n=0 satellite peak, and λ_{Cu} is the wavelength of the Cu $K_{\alpha 1}$ radiation. For the one-step and two-step graded buffers, this yields 120 Å and 126 Å, respectively, for the period. However, it is quite difficult to

define the central peak position and the other peaks are not evenly spaced so there is significant error in this determination. For the linearly graded Sample III, the spacing is more regular and corresponds to a period of 114 Å which is in good agreement with the targeted 110 Å. Of course, interpretation of the X-ray spectra from Sample III is complicated by the overlap of the GaAs substrate, the top p-type layer, the top of the n-type buffer, and the central peak from the MQW.

It is possible to estimate the In concentration in the MQW from the X-ray data. However, one can only give a range for lattice constants of AlGaAs and InGaAs that look reasonable. It is impossible to uniquely determine either of these values from the available data. This analysis is based on the following relationship between the measured lattice mismatch, Δa_{meas}, and the relaxed lattice mismatch, Δa_R:

$$\Delta a_{meas} = f \Delta a_R \tag{5-3}$$

where f is given by

$$f = [\frac{1+\nu}{1-\nu}] \tag{5-4}$$

and ν is the Poisson ratio given as a ratio of the material's elastic constants, c_{11} and c_{12}:

$$\nu = \frac{c_{11}}{c_{11} + c_{12}} \tag{5-5}$$

Lattice mismatch for the MQW may be expressed as the difference in lattice constant of the grown film, a_f, from the underlying buffer, a_b, where a_b is a relaxed lattice constant. (Usually this is taken to be the lattice constant of the substrate.)

$$\Delta a = a_f - a_b \tag{5-6}$$

Then, equation 5-3 for the film may be written in terms of its measured lattice constant, a_{fmeas}, and its relaxed lattice constant, a_{fR}.

$$a_{fmeas} = f(a_{fR} - a_b) + a_b \tag{5-7}$$

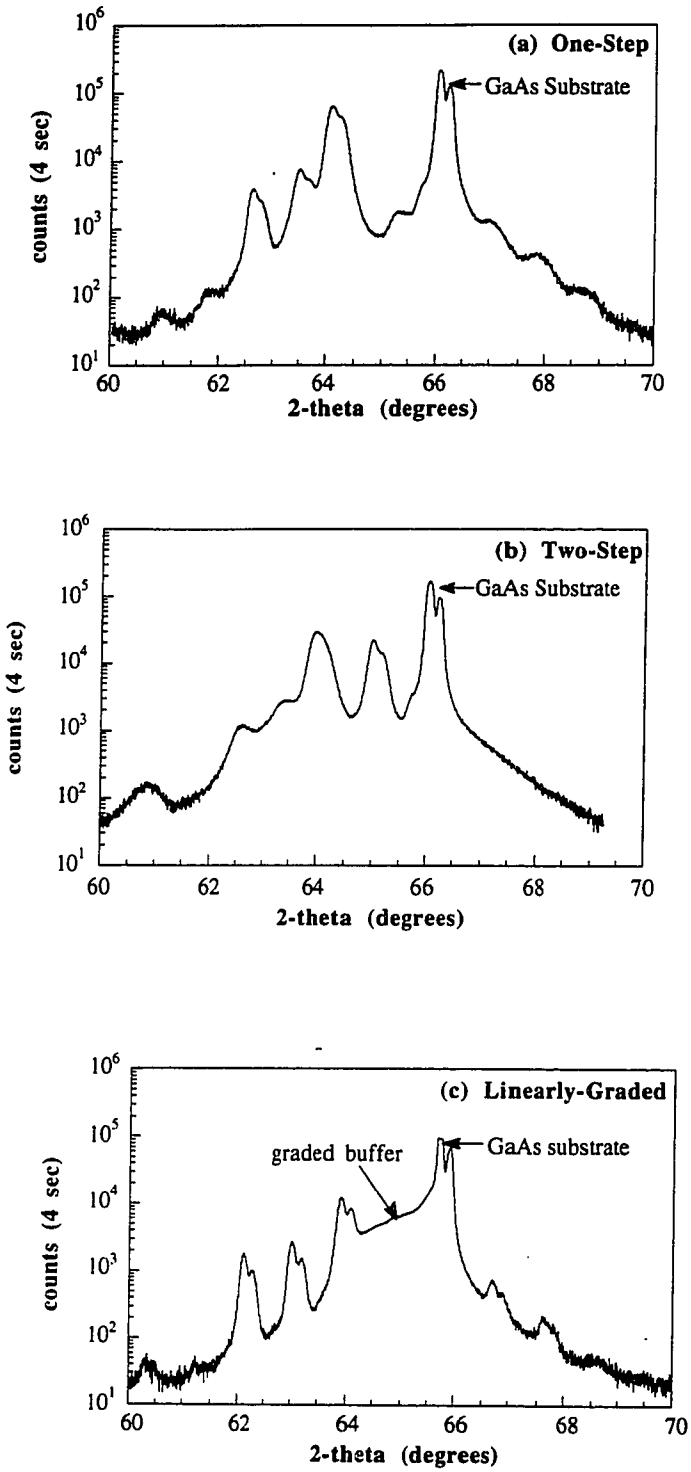

FIGURE 5.9 X-ray diffraction spectra for Samples (a) I, (b) II, and (c) III.

Solving for a_{fmeas} and substituting appropriate values of f for AlGaAs and InGaAs[133] gives the following equations:

AlGaAs: $a_{fR} = 0.52(a_{fm} + 0.9a_b)$ (5-8)

InGaAs: $a_{fR} = 0.50(a_{fm} + 1.0a_b)$ (5-9)

One may estimate the Al or In composition from the relaxed lattice constant using the equations in Chapter 2. From the position of the central satellite peak, one can determine the average lattice constant of the MQW using Bragg's law. Assuming that the ratio of the thicknesses of the individual layers is accurate (which seems reasonable from the determination of the period), one may relate the barrier lattice constant a_B to the quantum well lattice constant a_{qw} using Equation 5-9 for the case of Sample III with 75 Å quantum wells and 35 Å barriers.

$$637.274 = 75a_{qw} + 35\, a_B \qquad (5\text{-}10)$$

Then the procedure for determining In composition in the quantum wells is as follows:

1-Choose a value for a_B
2-Compute corresponding a_{qw} using Equation 5-10
3-Choose buffer lattice constant a_b
4-Compute a_{fR} for InGaAs using a_b and Equation 5-9
5-Compute In composition from Equation 2-4
6-Compute a_{fR} for AlGaAs using a_b and Equation 5-8
7-Compute Al composition from Equation 2-1
8-Apply the following constraints: $0 < [Al] < 1$ and $0 < [In] < 1$
9-Consider range closest to the targeted [Al] of 33% and find corresponding [In]
10-Repeat steps 3-9 for different buffer lattice constant a_b

Executing this procedure yields 42% In in quantum wells grown atop a 35% In buffer and 38% In in quantum wells grown atop a 29% In buffer. Of course, there is a significant amount of error in these determinations due to uncertainty in the average lattice constant from the X-ray measurement, layer thicknesses, and approximations in the procedure.

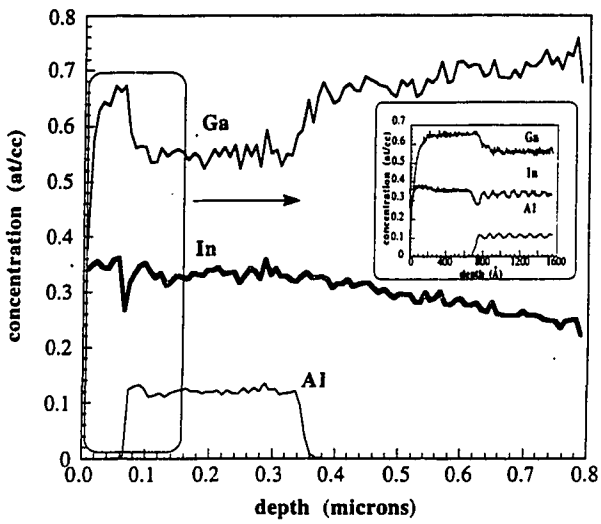

FIGURE 5.10 SIMS spectra for Sample III. Inset shows higher resolution analysis.

5.3.6. SIMS

SIMS was performed at Charles Evans and Associates using Cs^+. SIMS analysis confirms that the grading in Sample III is basically linear as shown in FIGURE 5.10. This sample was etched to remove 4000 Å of the top p-layer since SIMS resolution degrades as the sputtered depth into the sample increases. The remainder of this top layer was assumed to be the targeted composition of 35% In and used as an internal calibration for the subsequent analysis. Although it is possible to see the oscillations in In and Al concentrations which correspond to the quantum wells and barriers within the MQW, the resolution was insufficient to provide a direct estimate of the In composition in the wells. However, assuming that the ratio of the thickness of the barriers to the thickness of the wells was as targeted, one may estimate the In composition in the quantum wells from the average composition in the MQW. The measurement of the period from the SIMS data agrees with the X-ray diffraction analysis that the MQW period was indeed within a few percent of the targeted value. The average value of 33% In measured in the MQW yields 48.5% In in the quantum wells. The error is estimated[134] to be about ± 5 relative %. This gives a result of 48.5 %In ± 2.5% In. If the top layer is taken to be 29% from the electron microprobe data, the In composition in the quantum wells is about 40% ± 2% In.

5.3.7. Summary

Thus it has proven difficult to exactly determine the composition of In in the MQW, the top of the graded buffer, and the top p-type layer. A summary of the results obtained for Sample III using various techniques are presented in Table 5.1. The microprobe data for the quantum wells assumes a constant error in the In growth rate. None of the techniques are more accurate than ± 1% In. The most reasonable conclusion from this data seem to be that the quantum wells have less than the targeted 50% In. However, they have at least 40% In.

TABLE 5.1 In composition in MQW determined by various techniques.

Technique	**[In] in MQW 29% In buffer**	**[In] in MQW 35% In buffer**
Microprobe	41.5%	
300 K Absorption	41%	38%
X-ray	38%	42%
SIMS	40% ± 2%	48.5% ± 2.5%
77 K PL	48%	45%

It is worth noting that the PL peak and absorption peak will only exactly correspond if the PL peak is due to purely intrinsic features such as the bound exciton. Nonradiative recombination processes such as those involving defects can cause the PL peak to occur at lower energy than the absorption peak since the two processes are not entirely symmetric. In absorption, a single process occurs whereby a photon is absorbed, thus promoting an electron from a lower energy state to a higher energy state. In PL, a transition from a higher energy state to a lower energy state is required and there are both radiative and nonradiative processes by which this can occur. Thus, although PL may be easier to perform than absorption measurements, however, it may be more difficult to interpret since it often includes information involving defect levels rather than simply density of states information as in absorption. The difference in PL and absorption peak energy is known as a Stokes shift. If it is larger than 10 meV, Bastard[135] claims that it is unreasonable to attribute the PL peak only to intrinsic features. Rather some defects must be involved. In the comparison of the 77 K PL and 300 K absorption results here, the PL peak is indeed at a lower energy than the absorption peak. If we consider that the difference in energy

between 77 K and 300 K for our samples as the same as for GaAs, roughly 0.084 eV, then the PL peak at 300 K would be at 0.947 eV as compared with the 0.976 eV absorption peak. This difference of about 30 meV between the PL and absorption peaks is certainly in the range where defects should be considered. This is not surprising since InGaAs/AlGaAs is known to have significant nonradiative recombination.[136] So perhaps the PL data overestimates the amount of In in the MQW by underestimating the energy of the bandgap.

Auger Electron Spectroscopy (AES) might be the technique best suited to give an accurate quantitative result for the In concentration in the MQW. However, due to the thickness of the sample, it would be quite costly.[137] High resolution X-ray diffraction is also a promising technique and will be discussed in the analysis in Chapter 6.

5.4. Device Performance

After the growth of the p-i-n structure, the samples were etched down to the n-layer to form 500 x 500 μm square mesas. Electrical connections were made through an alloyed Au/Ge/Au contact to the n-type layer and an annular Ti-Au contact to the top of the mesas. The devices were packaged and wire bonded into a drilled chip carrier and the optical transmission and photocurrent measured with a half-meter spectrometer and a white light source. Measurements of the optical power into the sample were performed with a calibrated Ge infrared (IR) detector.

5.4.1. Electroabsorption Modulator

5.4.1.1. Photocurrent

Both of the samples with step-graded buffers exhibited no excitonic behavior during 300 K photocurrent measurements. Rather they had extremely broad absorption edges with no evidence of voltage-dependent shifts. This is in marked contrast to the excellent excitonic features and accompanying QCSE observed in photocurrent measurements of Sample III.

5.4.1.2. Quantum Confined Stark Effect

Room temperature optical absorption spectra at various applied biases for Sample III with the linearly-graded buffer layer are shown in FIGURE 5.11. Samples I and II exhibited no voltage dependence and thus their spectra under an applied voltage are identical to those in FIGURE 5.7 for zero field. Application of an electric field up to 300 kV/cm causes the exciton peak to red shift while the half-width at half-maximum (HWHM) of the exciton resonance remains less than 25 meV. The total shift obtained was about 600 Å yielding an

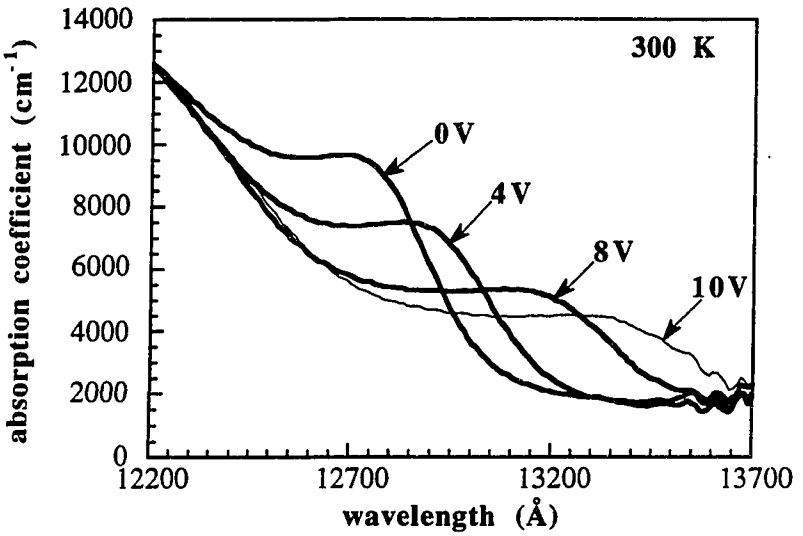

FIGURE 5.11 300 K absorption spectra for Sample III at various reverse bias voltages.

exciton at 1.33 μm. Although these resonances are considerably broader than those obtained in high quality low In content InGaAs/GaAs or AlGaAs/GaAs MQW, they certainly are promising for devices.

5.4.1.3. Transmission

The change in absorption and thus transmission as a function of voltage, as seen in FIGURE 5.11, makes the quantum wells in Sample III suitable for an electroabsorption modulator. The device functions as a transmission modulator with an insertion loss of about 4 dB. This relatively high value of insertion loss could easily be reduced by adding something as simple as an anti-reflection coating. The relative transmission ($\Delta T/T_0$) as a function of wavelength at various reverse biases is shown in FIGURE 5.12. If one operates on the exciton peak at 1.27 μm, a normally off modulator with a maximum $\Delta T/T_0$ of 17% is produced. Operation at 1.32 μm, where the initial absorption is zero, yields a normally on modulator with a $\Delta T/T_0$ of 12%.

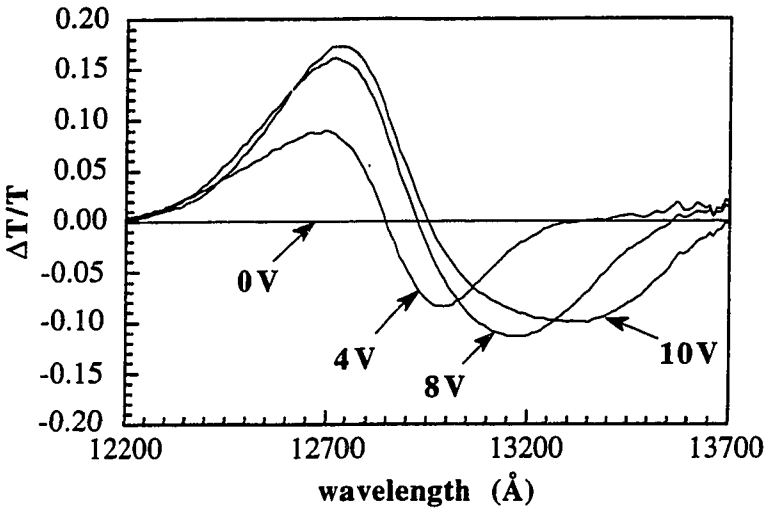

FIGURE 5.12 Relative transmission versus wavelength at various reverse bias voltages for Sample III.

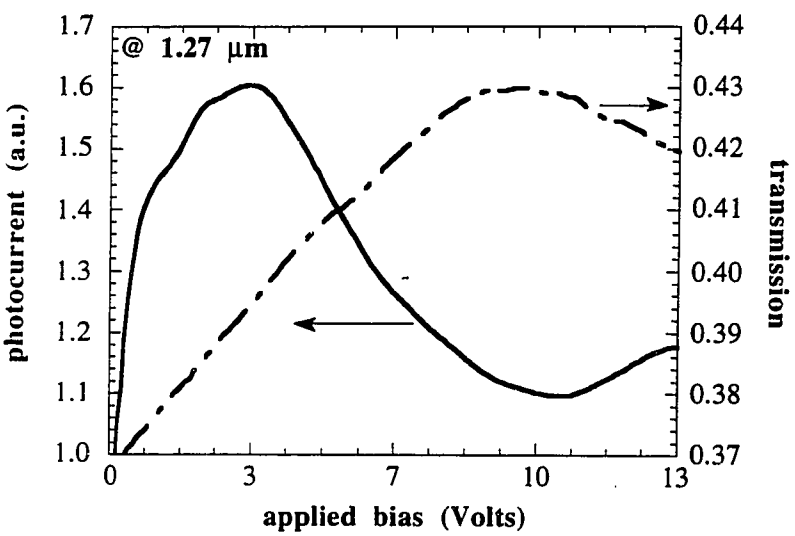

FIGURE 5.13 Photocurrent and transmission as a function of voltage at 1.27 μm for Sample III.

5.4.1.4. SEED Potential

Photocurrent measurements versus voltage exhibit the negative differential conductivity which is necessary for optical bistability. This suggests that the device is useful for operation as a self electro-optic device (SEED) at 1.27 μm. FIGURE 5.13 shows photocurrent and transmission versus voltage at 1.27 μm. There is about a 30% maximum decrease in photocurrent as the transmission through the device increases in the region from about 4 V to 10 V applied bias. Of course, better performance can be obtained by either anti-reflection coating both sides of the wafer or incorporating a Fabry-Perot cavity.

5.4.2. Photodetector

5.4.2.1. Leakage Current

The samples with step-graded buffers exhibited significantly higher leakage currents than that of the graded buffer sample. For 500 x 500 μm devices under 9 V reverse bias at room temperature, the leakage currents were roughly 30 mA/cm^2, 400 mA/cm^2, and 80 $\mu A/cm^2$ for Samples I, II, and III, respectively. The excellent leakage characteristics of Sample III are at least an order of magnitude lower than those reported by Tzeng et al.[97] for a bulk $In_{0.4}Ga_{0.6}As$ photodetector.

5.4.2.2. Responsivity and Quantum Efficiency

The high leakage currents in Samples I and II make them poor candidates for a photodetector. However, Sample III could also be used as photodetector offering advantages over the bulk photodetectors on GaAs that have been produced for operation in this wavelength regime described in Section 3.2.2.2. We have measured the quantum efficiency and corresponding responsivity of Sample III to characterize its performance as a photodetector. Quantum efficiency was calculated as described in Chapter 2 using the measured photocurrent, input optical power, and the measured values of α from FIGURE 5.11.[138] Using the 1.3147 μm line of a Nd:YAG laser,[139] the maximum external quantum efficiency measured was 14% at 8.65 V. The corresponding internal quantum efficiency was 80-100% depending on whether an α of 4000 or 3000 cm^{-1} was used. The corresponding external and internal responsivities were 0.15 and 0.85-1.06 A/W, respectively. The maximum values obtained using a white light source are tabulated in TABLE 5.2. For each reverse bias, the wavelength at which this maximum occurred, the external quantum efficiency (QE_{ext}) and internal quantum efficiency (QE_{int}) are shown. The 8V data shows lower efficiency than that measured with the laser. This is probably due to the difficulty of accurately performing the measurement with a white light source.

TABLE 5.2 Quantum efficiency for Sample III.

V(V)	λ(μm)	QE_{ext}	QE_{int}
0	1.27	0.05	0.24
4	1.28	0.09	0.54
8	1.31	0.07	0.58
10	1.33	0.06	0.58

These InGaAs quantum efficiencies are reasonably close to the ideal 100% quantum efficiency which is often realized in GaAs/AlGaAs devices. These quantum efficiencies are quite good compared to the 30% at 15 V bias reported by Zimgibl and Ilegems[103] for their metal-semiconductor-metal (MSM) photodetector with 48% In quantum wells. They suggest that the low value for quantum efficiency may be due to fast recombination within the active area of the device. As compared with their GaAs barriers, the higher AlGaAs barriers in these samples may contribute to a lower efficiency due to the longer time allowed for interaction of carriers with traps[140] as well as the larger defect concentration within AlGaAs.[141] However, the AlGaAs barriers also contribute to lower leakage currents which are advantageous for photodetectors.

5.5. Conclusions

In this chapter, sharp excitonic resonances were achieved near 1.3 μm in InGaAs quantum wells grown on a GaAs substrate by molecular beam epitaxy using a linearly-graded InGaAs buffer layer. Our results indicate that linear grading is preferable to step grading for high In composition InGaAs on GaAs. SIMS results confirm the linearity of the grading. Cross-section TEM analysis of the graded sample reveals dislocations within the buffer layer but none which thread up to reach the quantum wells. In addition to a well-defined exciton at 1.27 μm under zero bias, pronounced quantum confined Stark effect is observed in the absorption spectrum of a sample including a linearly-graded buffer, while the spectra from samples with step-graded buffers exhibit no excitonic features. A transmission electroabsorption modulator with a relative transmission modulation ($\Delta T/T_0$) of 17% at 1.27 μm and 12% at 1.32 μm is demonstrated. A photodetector with low leakage current and high quantum efficiency at 1.3 μm on GaAs was also reported. The results from the linearly-graded sample in this chapter illustrate the usefulness of such buffers for producing good quality quantum wells in a highly mismatched materials system.

6. EFFECT OF GRADIENT OF LINEARLY-GRADED BUFFER LAYERS

6.1. Overview

This chapter describes an investigation into the effect of varying the gradient of the linearly-graded buffer. The first section discusses the structure and MBE growth of the samples. Then, characterization of the samples by various techniques including microscopy, double crystal X-ray diffraction (XRD), and electron microprobe will be presented. Finally, device performance as an electroabsorption transmission modulator and a photodetector will be reported.

6.2. Structure and MBE Growth

All samples were grown on semi-insulating GaAs substrates by MBE at 450 °C using As_2. The use of As_2 and low substrate temperature are particularly important for the successful growth of high In compositions as described in the previous two chapters. A schematic of the targeted structures is shown in FIGURE 6.1. After a 500 Å GaAs buffer layer, an n-type InGaAs buffer layer was grown where the In composition was graded from 0 to 35% at a rate of 7.5%, 15%, or 30% In/μm for Samples I, II, and III, respectively. The mismatch, thickness, and time for growth of the buffers in these samples are summarized in TABLE 6.1. On top of the buffer, MQW consisting of thirty 75 Å $In_{0.50}Ga_{0.50}As$ quantum wells with thirty-one 35 Å $Al_{0.33}Ga_{0.67}As$ barriers were grown. To complete the p-i-n structures, 5000 Å of p-type $In_{0.35}Ga_{0.65}As$ was grown on top.

TABLE 6.1 Buffer descriptions for Samples I through V.

	Buffer Gradient		**Buffer**	
Sample	**%In/μm**	**%mismatch /μm**	**Thickness (μm)**	**Time (h)**
I	7.5	0.5	4.6	5.40
II	15	1.0	2.3	2.70
III	30	2.0	1.15	1.35
IV	60	4.0	0.57	0.68
V	30 + 2.5 μm		3.65	3.85

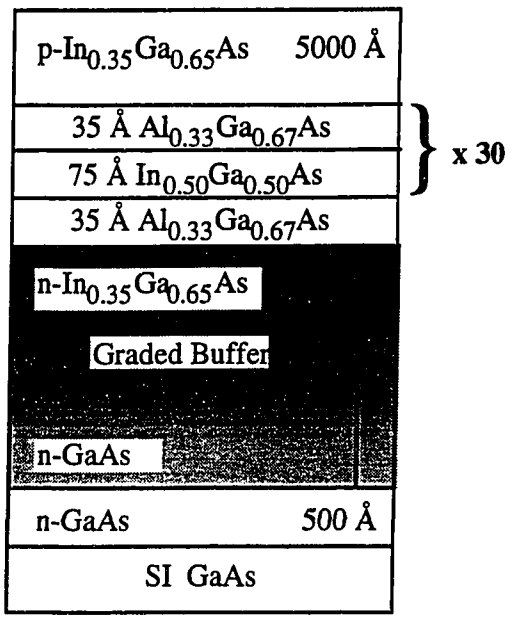

FIGURE 6.1 Schematic of MBE-grown structures.

To obtain a more accurate measure of the In concentration in the MQW, a calibration sample, CalA, was grown in the same series of growths as Samples I, II, and III. This calibration sample consisted of a 1 μm thick layer of InGaAs at the same composition as the MQW. Since it is so thick, the 1 μm InGaAs layer should be fully relaxed and X-ray can easily be used to determine the In concentration.

In a later growth run, several other samples were grown. These included CalB, a calibration sample with 0.7 μm of InGaAs, Sample IV with a structure like Samples I, II, and III but with a 60% In/μm gradient, and Sample V with a 30% In/μm gradient followed by a 2.5 μm thick layer of constant composition $In_{0.35}Ga_{0.65}As$. TABLE 6.1 also includes information on the buffers for Samples IV and V.

The wide range of gradients represented by Samples I, II, III, and IV was chosen to explore the effect of different gradients as well as the question of a critical gradient above which the benefits of grading are no longer observed i.e. no excitons can be seen for quantum wells grown atop such a buffer. The design of Sample V was chosen to permit investigation of the effect having the same gradient but different thickness (by comparing Samples III and V) and similar buffer thickness but different gradient (by comparing Samples I and V). Thus Sample V should provide some insight into the roles of thickness

and gradient of the buffer layer in determining the quality of the subsequently grown MQW.

6.3. Materials Characterization

6.3.1. Microscopy

6.2.1.1. Scanning Electron Microscopy (SEM)

The thick calibration layers showed very rough morphology as seen in FIGURE 6.2. This provides a good example of the poor surface morphology exhibited by thick layers of high In content InGaAs grown on GaAs without graded buffer layers.

In contrast to the surface of the calibration samples, the surface morphology of all the linearly-graded samples showed strong crosshatching under optical and scanning electron microscopy. SEM images are shown in FIGURE 6.3. Although lines are visible in two perpendicular directions, a strong preference is observed in the direction perpendicular to the substrate's major flat, the (011). The samples grown in the later run, IV, V, and CalB, showed considerably more surface defects than those grown in the first run. This could be related to the condition of the source material or the MBE system itself.

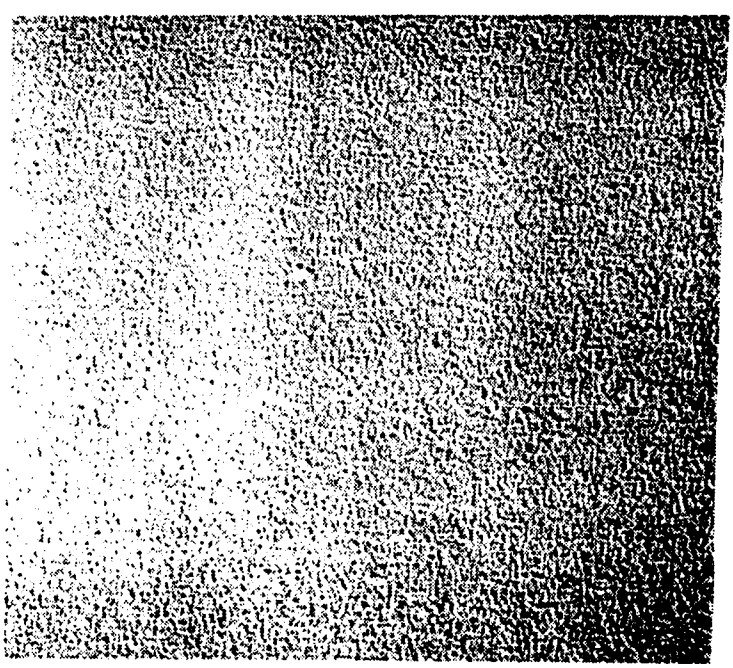

FIGURE 6.2 SEM image (860X) of the surface of calibration sample (CalA) with 1 μm InGaAs.

(a) Sample I
7.5 %In/μm

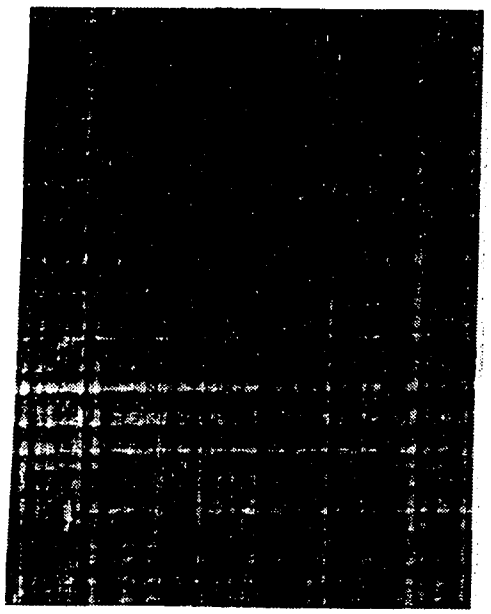

(b) Sample II
15 %In/μm

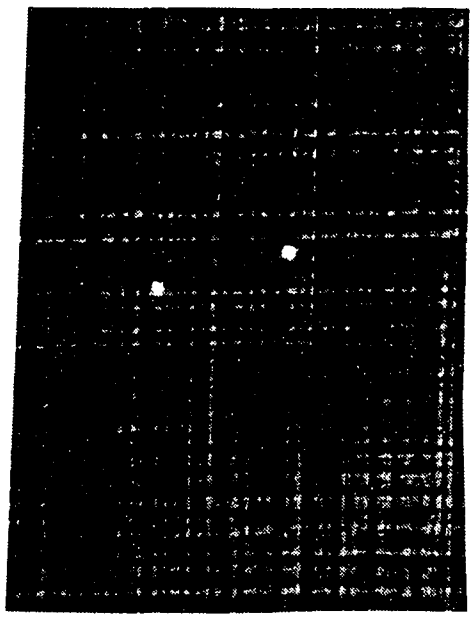

(c) Sample III
30 %In/μm

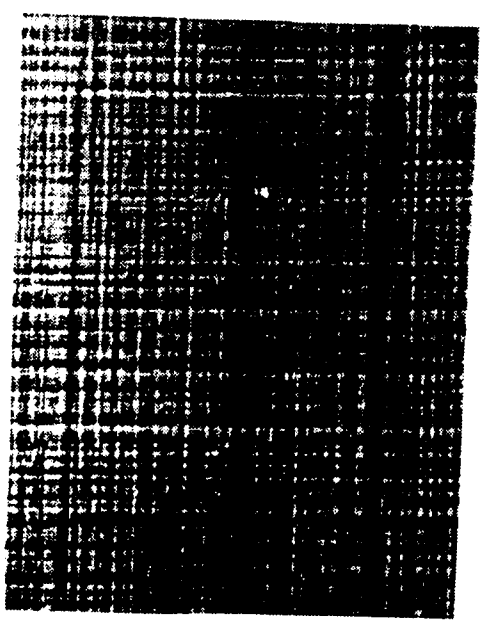

(d) Sample IV
60 %In/μm

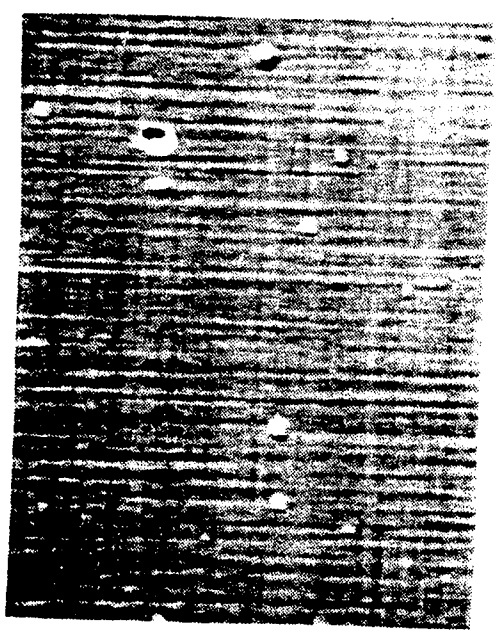

FIGURE 6.3 SEM images (860X) of Samples (a) I, (b) II, (c) III, and (d) IV.

6.2.1.2. Atomic Force Microscopy (AFM)

AFM was performed on a Digital Instruments Nanoscope II Scanning Probe Microscope. FIGURE 6.4 shows the images from Sample I and Sample III. Analysis by AFM revealed features of maximum height 400 Å perpendicular to the preferred (110) crosshatch direction and 250 Å parallel to the preferred direction. Average surface roughness on all samples was about 50 Å perpendicular to and 30 Å parallel to the preferred direction. The spacing between the crosshatch lines ranged from about 1 μm to 5 μm between the preferred lines. Such crosshatch spacing is consistent with other reports[142,73] of crosshatch in mismatched systems. These spacings between the preferred lines were larger for the sample with the slower grading. Sample I had a spacing of about 3 μm while Sample III had a spacing of about 1.5 μm. However, Sample II had a spacing of about 3.5 μm. The spacing between the nonpreferred lines was more uniform and on the order of 5000 Å. The crosshatch features on the surface do not show a one to one correspondence with dislocations as observed in TEM. Rather the surface features seem to be indicative of a gradual modulated strain over a large area.

The origin of this crosshatch morphology is not well understood. InGaAs and GaAs do have different thermal expansion coefficients which could introduce dislocations from the top surface during the cooling process after MBE growth. The driving force for introduction of such dislocations may be described as the difference between the amount of strain due to thermal mismatch and that accommodated elastically (i.e. the yield strain). The yield strain may be estimated[143] using the analysis in Nix.[65] For a 5000 Å thick film of $In_{0.35}Ga_{0.65}As$, the yield stress is about 4 $\times 10^8$ dynes/cm^2 which corresponds to a strain of 3.1 $\times 10^{-4}$. The strain due to thermal expansion mismatch for $In_{0.35}Ga_{0.65}As$ on GaAs cooling from 450 °C to 25 °C is roughly between 2.2 $\times 10^{-4}$ and 3.5 $\times 10^{-4}$ depending on chosen values for the thermal expansion coefficients.[12,144] Thus the driving force for introducing dislocations due to thermal mismatch is insufficient to account for the density of dislocations observed at the top/p-type interface or the surface.

The surface morphologies reported in this chapter are consistent with the results reported by Hsu et al[145] on relaxed SiGe films. They also observed that the roughness on the surface increased as the grading rate was increased. They propose that the crosshatch is due to inhomogeneous strain fields surrounding the underlying misfit dislocations combined with the surface diffusion. During growth of the graded region, the large strain fields near the growing surface facilitate nonuniform growth rates reducing strain energy at the cost of adding roughness. When a thick constant composition layer is grown atop such

a graded buffer, there is some planarization but the crosshatch remains. For the samples described in this chapter, the MQW and top p-type layer separate the underlying misfit dislocations from the surface. Thus the crosshatch pattern is similar to a far field pattern of the dislocation strain fields.

(a) Sample I
7.5 % In/μm

(b) Sample III
30 %In/μm

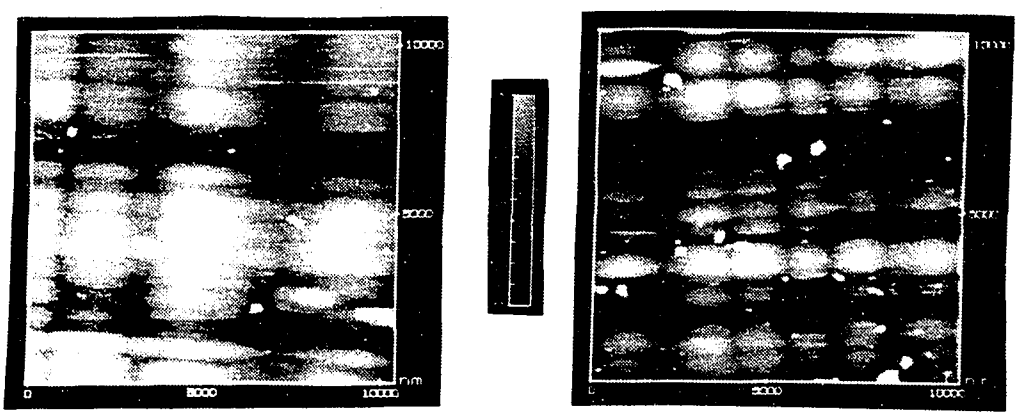

FIGURE 6.4 AFM image of (a) Sample I and (b) Sample III. Note that shading corresponds to surface height with the brightest portions of the image being 35 nm higher than the darkest portions.

6.2.1.3. Plan-View Transmission Electron Microscopy

Plan-view TEM analysis was performed using a Philips EM400 at 120 kV operating voltage. FIGURE 6.5 shows a plan-view image of Sample III. An array of perpendicular (110) dislocations is observed. This dislocation network begins at the interface between the top p-type layer and the MQW. The alternating contrast characteristic of MQW is observed in FIGURE 6.5. However, due to the geometry of the sample, the MQW are only visible through the top-p-type layer. Beneath the MQW, the sample becomes too thick for reliable TEM images. Thus these images can not be used to identify the exact location of the dislocation array.

The form of this network resembles the surface crosshatching seen in SEM and AFM. However, the spacing between the dislocation lines is much smaller than that between the crosshatch lines. Qualitatively, the surface crosshatch and the misfit dislocation network share the appearance of a preferential (110) direction as well as irregular spacings with

some dislocations coming in pairs while others are single. The clustering of some of the dislocations is consistent with the cross-section TEM results.

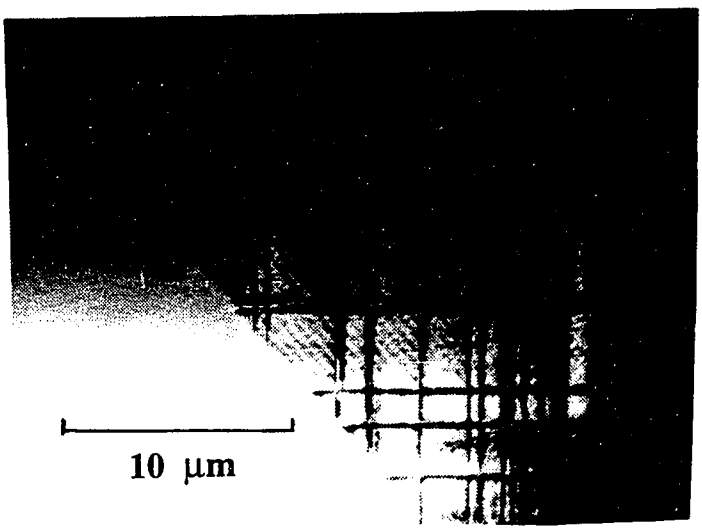

FIGURE 6.5 Plan-view TEM image of Sample III.

6.2.1.4. Cross-Section Transmission Electron Microscopy

Cross-sectional TEM analysis was also conducted using a Philips EM400 at 120 kV operating voltage. Samples were prepared as described in Chapter 5. Cross-sectional TEM was used to analyze the structural quality of these samples. All of the graded samples show similar structure with smooth MQW, a clear region immediately beneath the MQW, and a number of lateral dislocations deeper within the buffer layer. Similar character dislocations were observed in all cases with the dislocation lines lying along (110) directions. FIGURE 6.6 shows images of samples with 7.5% and 30% In/μm gradients. These images include the top portion of the graded buffer layer, the MQW, and some of the top p-type layer. Although there are a considerable number of dislocations within the buffer layer, most of them propagate horizontally and none, within the observed areas, appear to thread up through the MQW. In fact, for all of the samples studied, only rarely is a vertically threading dislocation observed. Again, as described in Chapter 5, the horizontal dislocations suggest that efficient relaxation has occurred within the buffer.

(a) Sample I (b) Sample III

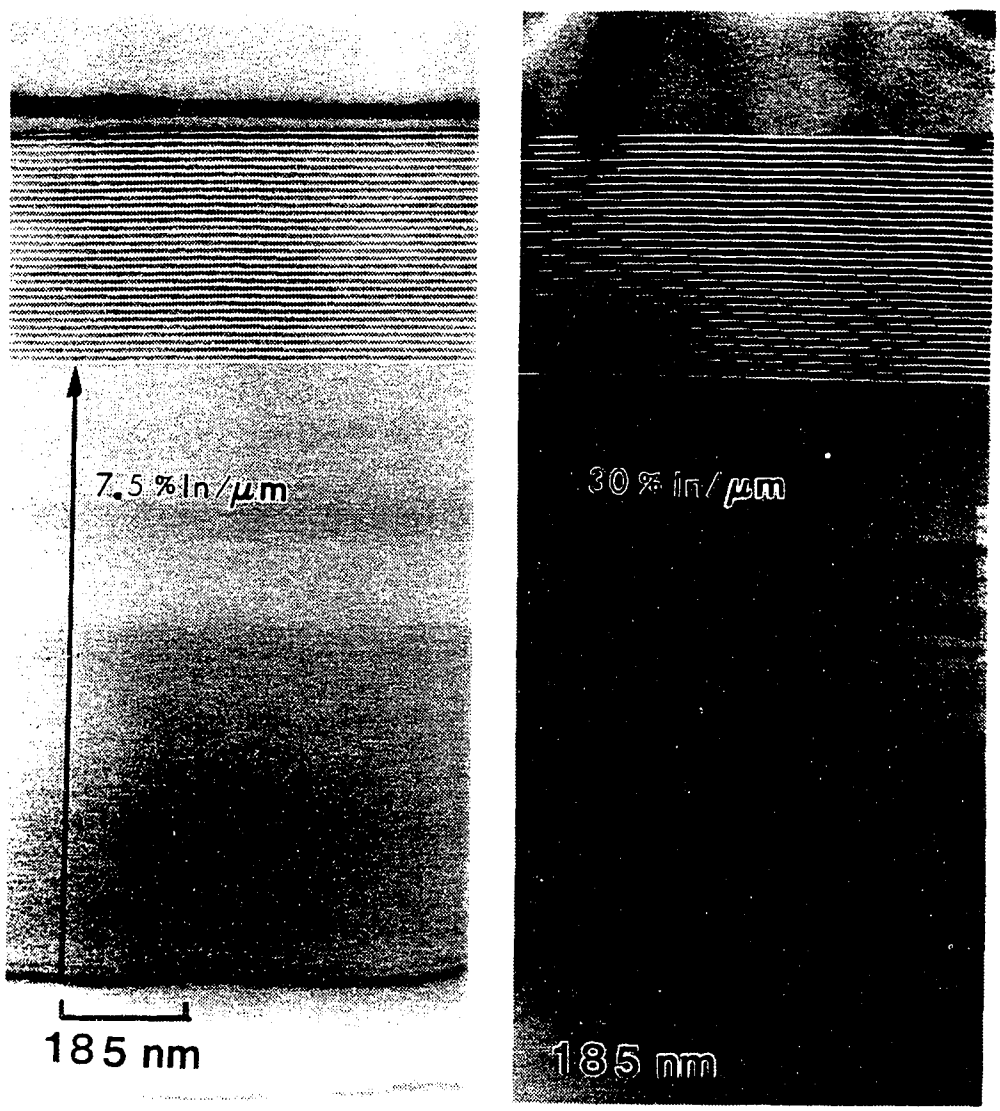

FIGURE 6.6 Cross-section TEM images of Samples (a) I and (b) III.

The most obvious difference among the samples with different gradients is the difference in the thickness of the dislocation-free region beneath the MQW.[146] Note that the In composition grading does continue throughout this region. As the buffer gradient decreases, the thickness of this clear region increases. TABLE 6.2 summarizes the

thickness of this region for the various samples and the corresponding percentage change of In that occurs in the clear region. It seems reasonable that the width of this region should depend on the gradient as it could be a function of reaching a certain In composition and thus dropping below a certain threshold for the nucleation of new dislocations. The last column of TABLE 6.2 estimates the In concentration at the start of the clear region assuming that the top of the buffer is 35% In and suggests that this critical In composition is about 28%. The data for the 15% grading was taken from the linearly-graded sample discussed in Chapter 5. Thus we expect it to have less In than the other samples based on other materials measurements. If the top of its buffer were a few % less In, then its clear region might begin closer to 28% In.

This clear region may be explained using theory developed by Fitzgerald et al.[147] which extends the Matthews-Blakeslee model to include a composition gradient term in the calculation of a local critical thickness. This theory suggests that as growth proceeds, a dislocation-free region rides the surface.[148] Once this clear region exceeds the critical thickness for that gradient, dislocations are introduced. However, if this thickness has not exceeded when the grading is halted, the dislocation-free region is essentially frozen in place. Thus the clear region observed in the samples in this chapter could correspond to the local critical thickness for a given gradient. Fitzgerald's theory predicts that as the grading rate decreases, the local critical thickness increases. This is consistent with the results from Samples I, II, III, and IV that the thickness of the clear region increases as the buffer gradient decreases. Remembering the discussion of the crosshatch as a "far field" of the dislocation strain fields from Section 6.1.2.1, it seems reasonable that the surface crosshatch lines are spread farther apart for the slower grading since the dislocations are deeper below the surface.

TABLE 6.2 Characteristics of clear region.

Gradient	Clear Region (Å)	% In change in Clear Region	% In at start of Clear Region
7.5	8200-8865	6-7	28-29
15	3375	5	30
30	2250-3000	7-9	26-28
60	1430-1610	9-10	25-26

The interfaces of the MQW in FIGURE 6.6a and 6.6b look quite nice. No visible dependence of the interfaces on the gradient is observed. In both samples shown in FIGURE 6.6, some dislocations are visible at the MQW/p-type top interface. It is difficult to positively identify them as dislocations from these pictures but further analysis by tilting the sample showed lines characteristic of dislocations. However, no dislocations were visible at the buffer/MQW interface under any diffraction conditions. The dislocations at the MQW/p-type interface could perhaps be explained in terms of continuing relaxation. More of these dislocations are observed for the samples with the faster grading which would be consistent with such a model. For the slower gradient, most of the relaxation happens within the graded buffer. For the faster gradient, measurable strain may exist at the top of the buffer. Throughout the MQW, this remaining strain is not relieved due to the presence of multiple interfaces. However, once the p-type layer begins, there are no additional interfaces and all of the remaining mismatch is relieved at the MQW/p-type interface.

The TEM image of Sample V is similar to those of Samples I through IV. The MQW are distinct and their interfaces appear quite flat. This sample shows a very thick region which is dislocation-free. The thickness is about 2.3 μm. The lateral dislocations cover a vertical distance of roughly 1.3 μm. Since the graded region of this sample was only 1.15 μm, this suggests that the dislocations extended throughout the entire graded region and even a little bit into the constant composition layer. Thus perhaps the MQW are somehow contributing to the clear region. But the effect is not simply that the presence of MQW repels the dislocations to a certain distance since the gradient and structure of the buffer layer also contribute to the thickness of the clear region.

6.3.2. X-ray Diffraction

XRD on CalA and CalB were performed using a Picker Cu powder diffractometer. Because the layers of InGaAs in these samples are so thick, they may be assumed to be fully relaxed. Thus from the X-ray peak observed, one may estimate the In composition of the layer to within about 1% In using Equation 2.4. This yields 51% In for CalA and 50% In for CalB in excellent agreement with the targeted 50% In.

XRD on Samples I, II, and III was performed using a Bede diffractometer with Cu $K_{\alpha 1}$ radiation and a GaAs reference crystal. Satellite peaks were visible on all samples which indicates reasonably good quality MQW. A representative spectra from the 7.5% In/μm sample is shown in FIGURE 6.7. However, the peaks were broad compared with high

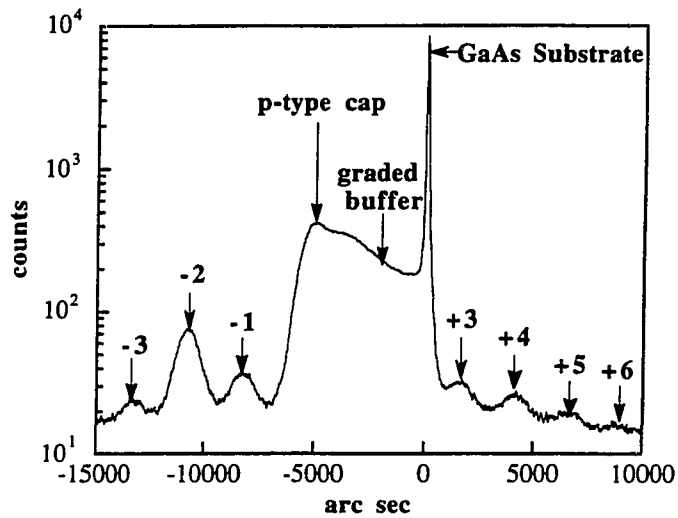

FIGURE 6.7 X-ray spectrum from Sample I with 7.5% In/μm graded InGaAs buffer.

quality GaAs/AlGaAs or even low In content InGaAs/GaAs MQW. Satellite peak full widths at half maximums (FWHM) of approximately 1470 arcsec were measured for all samples with no significant differences among peak widths corresponding to grading rate. This is considerably broader than the 560 arcsec FWHM reported for $In_{0.24}Ga_{0.76}As$/GaAs MQW[7] which the authors concluded corresponds to a grain size of about 1000 Å. Thus we expect the domains of high quality material in our samples to be less than 1000 Å.

The period of the MQW was determined from the satellite peak spacing, as described in Chapter 5, to be within 5% of the targeted value indicating fairly good control in the growth process in agreement with the measured value of 51% In for the targeted 50% Sample CalA. Satellite peaks up to fourth order were visible on all samples. For the (115) reflection, the sixth order positive reflection was visible on the sample with the 7.5% grading and indistinguishable on the samples with higher grading rates. This supports the trend that the quality of the material increases as the gradient of the grading decreases. The decrease in intensity of the higher order peaks may be attributed to interface roughness.[149]

The amount of relaxation in these structures was difficult to assess. Determining the amount of strain in the MQW is complicated by the overlap of the n=0 peak from the MQW and the signals from the top p-type $In_{0.35}Ga_{0.65}As$ cap layer and the top of the graded layer

which is also $In_{0.35}Ga_{0.65}As$. Glancing incidence and glancing exit conditions were used on the top p-type cap and its relative relaxation on GaAs was estimated to be 78%, 84%, and 82% for the 7.5%, 15%, and 30% In/μm samples, respectively. The satellite peaks could only be seen in the glancing incidence condition and thus data from two asymmetric peaks, the (224) and (115), was used to estimate the relaxation in the MQW, which was roughly 80% relative to GaAs. This probably indicates that the top cap and the MQW are at roughly the same lattice constant with most of the relaxation occurring in the graded buffer as designed.

From one-dimensional kinematic simulations[150] on Sample III, the lattice constants for the AlGaAs barriers and InGaAs quantum wells were determined to be 5.58 Å and 5.95 Å, respectively. These correspond to an In concentration of 48% and an Al concentration of 33% on a 33% In buffer using the analysis described in Section 5.2.4. This suggests that the In concentrations were within 4-6% of the targeted values. Reasonable agreement with design parameters was achieved.

6.3.3. Electron microprobe

Electron microprobe analysis was performed on the surfaces of Samples I, II, III, IV, V and CalA and CalB. The analysis was performed at 15 keV and 40 degrees resulting in a penetration depth of about 4000-5000 Å. Thus for Samples I-V, microprobe will sample only the top p-type cap layer. For the calibration samples, the top half of the thick layer will be sampled. The results are shown in TABLE 6.3. Two values are given for CalA because the analysis was performed twice at two separate times on different pieces of the wafer. Although some composition variation would be expected across the wafer, 7% is much larger than is usually observed. It seems more likely that the error in the microprobe concentration determination could be as large as 7%. CalA and CalB were determined to contain 51% In and 50% In, respectively, by X-ray diffraction. These values are closer to the targeted 50% and seem more reasonable Both the microprobe and the X-ray data show that CalB has less In than CalA. However, the microprobe seems to have a larger error. Samples I, II, and III were analyzed at the same time as the 55.5 % In determination for CalA. Samples IV, V, and CalB were done with the 48% determination for CalA. This suggests that the first series of measurements may have all been a bit high while the next series were a bit low in their In composition determinations.

TABLE 6.3 Microprobe results.

Sample	Gradient (%In/μm)	[In] at center
I	7.5	36
II	15	38
III	30	36
IV	60	32
V	30 + 2.5 μm	32
CalA	none	55.5/48
CalB	none	45

6.4. Device Performance

After growth, the samples were etched down to the n-layer to form 500 x 500 μm square mesas. Electrical connections were made through an alloyed Au/Ge/Ni/Au contact to the n-type layer and an annular Ti-Au contact to the top of the mesas. The devices were packaged and wire bonded into a drilled chip carrier and the optical transmission measured with a half-meter spectrometer, a white light source, and a Ge detector.

6.4.1. Electroabsorption Modulator

6.4.1.1. Absorption Spectra

Zero-field optical absorption measurements at room temperature reveal well-defined excitons for all samples studied. The absorption coefficient (α) was calculated from transmission measurements as described in Section 2.3.1.5. All data was taken at room temperature using a 300 K Ge detector, 2 mm slits on the spectrometer, 5 Å/step, and 90W of white light. As seen in FIGURE 6.8, as the buffer gradient decreases, the exciton resonance becomes sharper and occurs at a longer wavelength. The exciton peak position and HWHM for all five samples are summarized in TABLE 6.4. Sharper exciton resonance widths are generally associated with higher quality material. These widths are considerably broader than those of high quality GaAs/AlGaAs quantum wells which can be as small as 5 meV HWHM limited by phonon scattering.[151] Of course, InGaAs wells also have alloy broadening which can contribute several meV so that even optimized strain relief

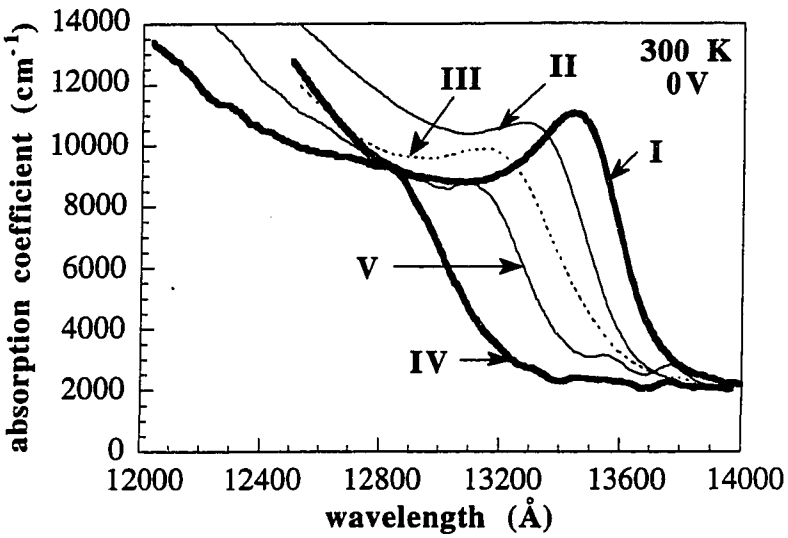

FIGURE 6.8 300 K absorption spectra for Samples I, II, III, IV, and V at 0V.

growth shows HWHM on the order of 9 meV.[94] Lower In content $In_{0.20}Ga_{0.80}As/Al_{0.33}GaAs$ MQW previously grown in the same MBE system showed a HWHM of about 7 meV.[17] Although the material in the present study is not optimized, decreasing the gradient does seem to produce higher quality material. Assuming that the In content in the InGaAs MQW is identical in all samples, the observed wavelength behavior is consistent with more relaxation occurring in the samples with slower grading. The higher quality material observed for the slower gradient may also be a result of more relaxation occurring in the buffer and thus less relaxation occurring throughout the MQW or in the top p-type layer. For the slower gradient, dislocations in the graded buffer are also further away from the MQW, lessening the influence of their strain fields.

Since Samples IV and V were not grown in the same run as Samples I, II, and III and their calibration wafers were 1% different in In composition, a direct comparison of the position of their absorption peaks is difficult. Adding the equivalent of 1% In to Samples IV and V increases the wavelengths of their peaks by about 0.01 μm bringing them closer to those of Samples I, II, and III. However, even with this adjustment, the 60% grading (Sample IV) still has a lower wavelength exciton peak than Sample III with the 30% grading in keeping with the results that a faster grading yields a shorter wavelength exciton. Also, the width of the exciton from Sample IV is quite broad supporting the trend observed for Samples I, II, and III that the width of the exciton resonance increases as the grading increases.

TABLE 6.4 Zero field exciton results for Samples I through V.

Sample	Buffer		Exciton Peak (μm)	HWHM (meV)
	Gradient (%In/μm)	Thickness (μm)		
I	7.5	4.6	1.34	11
II	15	2.3	1.33	14
III	30	1.15	1.32	17
IV	60	0.57	1.28	20
V	30 + 2.5 μm	3.65	1.31	14

Sample V is more difficult to compare with the other samples. It has a narrower width than Sample III suggesting that the thicker buffer layer plays a role in improving material quality even if it is not graded throughout. Its position appears to be similar to that of Sample III after accounting for the 1% In difference. Thus the position seems determined more by the buffer gradient than the total buffer thickness. Since the relaxation of the buffer is the parameter which would most affect the exciton position (excluding In variations), it seems to suggest that all of the relaxation occurs within the graded buffer and the extra constant composition layer simply acts to improve the material quality but the amount of strain in the MQW or relaxation in the buffer remain the same.

Samples I, II, and III exhibited the quantum confined Stark effect (QCSE) upon application of a reverse bias. FIGURE 6.9 shows the absorption spectra for Samples I, II, and III at various applied biases. Samples IV and V were not measured under applied bias. However, based on their zero field spectra, they are expected to have similar behavior to Samples I, II, and III. The best modulation should still be from Sample I since it had the sharpest exciton at zero field.

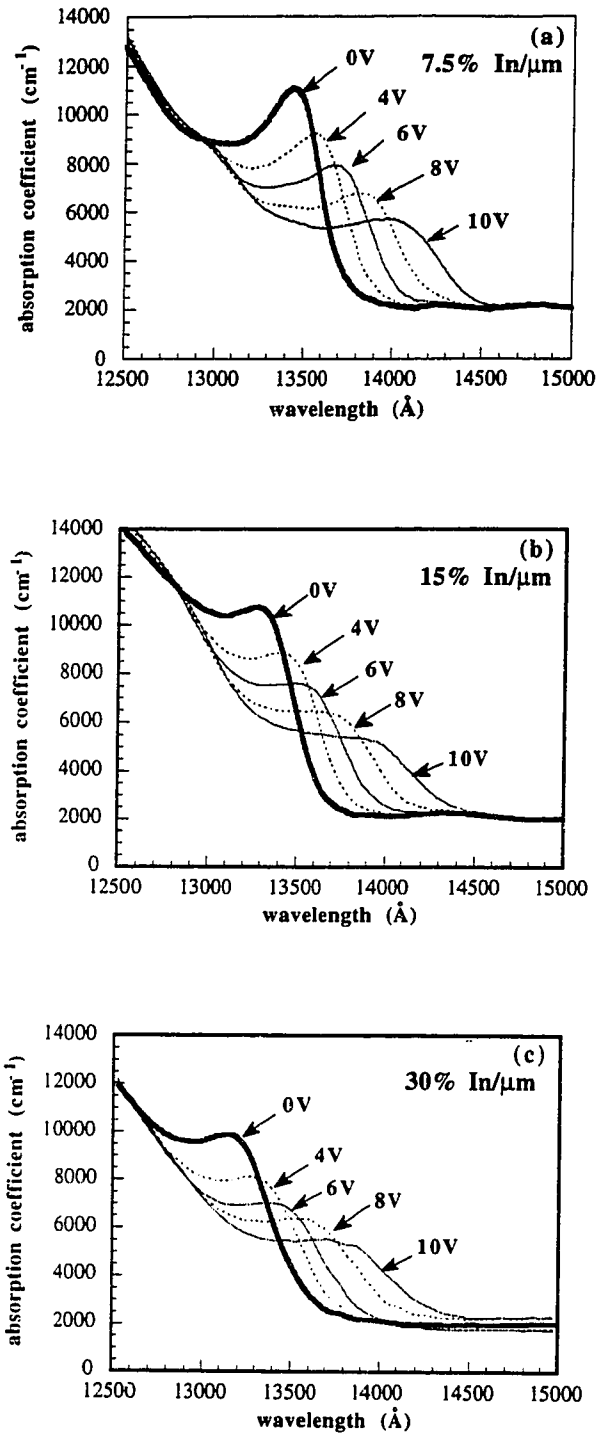

FIGURE 6.9 Absorption spectra at various reverse bias voltages for Samples (a) I, (b) II, and (c) III.

6.4.1.2. Transmission

TABLE 6.5 shows the maximum attained modulation for Samples I, II, and III for normally-off and normally-on devices. The value in % of the modulation and the wavelength in μm at which it occurred are indicated. The maximum modulation was usually obtained for the highest applied voltage i.e. 10 V. Note the trend toward larger modulation for slower gradients which is consistent with slower gradients yielding higher quality material. Of course, this improvement comes at the cost of increasing the growth time. For example, the 7.5 %In/μm buffer required 5.4 h compared to 0.68 h for the 60 % In/μm buffer. Exactly at 1.3 μm, the maximum modulation achieved is only 2, 6, and 9% for Samples I, II, and III, respectively. These values are low because the devices are not optimized for 1.3 μm operation. The modulation at 1.3 μm could be improved by adjusting the In concentration so that the zero field or high field exciton occurs exactly at 1.3 μm. The insertion loss for these three samples was about 4.7 dB. This value is reasonable considering substrate absorption and the lack of an anti-reflection coating.

TABLE 6.5 Modulation characteristics for Samples I, II, and III.

Sample	Gradient	Normally Off Max $\Delta T/T_0$ (+)		Normally On Max $\Delta T/T_0$ (-)	
	%In/μm	%	μm	%	μm
I	7.5	22	1.34	15	1.38
II	15	18	1.33	14	1.37
III	30	15	1.32	12	1.37

6.4.2. Photodetector

6.4.2.1. Leakage Current

For 500 x 500 μm devices under 9V (2.7 x 10^5 V/cm) reverse bias, typical leakage currents were 50 A/cm^2, 32 μA/ cm^2, and 1 mA/cm^2 for Samples I, II, III, respectively. A range of values for the leakage current existed across the processed quarter-wafer. Some of this nonuniformity was probably due to problems with the uniformity of the etching step. The resulting yields were not particularly good. The leakage currents were quite high for Samples IV and V. For 500 x 500 μm devices under 5V (1.3 x 10^5 V/cm) reverse bias, leakage currents were typically 40 mA/cm^2. The second processing run for Samples IV

and V had lower yield than the run for Samples I, II, and III. Thus these values for leakage current should not be taken as purely indicative of material quality.

6.4.2.2. Responsivity and Quantum Efficiency

Responsivity and quantum efficiency are directly proportional to photocurrent. The maximum photocurrent measured and thus the maximum quantum efficiency are similar for Samples I, II, and III. For all three samples, the maximum photocurrent obtained occurred at 4V (1.2 x 10^5 V/cm) reverse bias and was about 150 nA at 1.34 μm. TABLE 6.6 shows the values for peak photocurrent, wavelength, and the calculated quantum efficiencies (QE) and responsivities (R). The external quantum efficiencies and responsivities were about 10% and 11 A/W, respectively. Using Equation 2-24 with R1 and R2 equal to 32% and L equal to 3335 Å, yields internal quantum efficiencies of about 60%. These efficiencies compare well with the results obtained for the linearly-graded sample in the previous chapter. The sample with the slowest grading does have the highest quantum efficiency in keeping with previous measurements which suggest that the slower grading yields higher quality material. The high leakage currents for Samples IV and V made measurements of photocurrent difficult and unreliable.

TABLE 6.6 Photodetector performance of Samples I, II, and III.

Sample	λ (μm)	Max I_{pc} (nA)	QE_{ext}	R_{ext}	α (cm^{-1})	QE_{int}	R_{int}
I	1.35	146	0.11	0.12	6900	0.63	0.58
II	1.345	148	0.10	0.11	6600	0.55	0.51
III	1.34	130	0.09	0.10	5450	0.58	0.54

6.5. Conclusions

In this chapter, it has been shown that gradients of up to 60% In/μm or 4% mismatch/μm are useful for growth of high quality InGaAs with high In content by MBE. Excitons were observed at room temperature near 1.3 μm for samples with gradients of 7.5%, 15%, 30%, and 60% In/μm. Thus, a critical gradient above which no exciton was visible was not observed. However, since a totally abrupt step-grading was shown to yield poor material with no excitons, a critical gradient must exist somewhere above 60% In/μm. As the gradient decreases, the HWHM of the exciton resonance decreases and the resonance occurs at a longer wavelength. X-ray diffraction data also supports the trend that material

quality improves as the gradient of the grading decreases with the 7.5% In/μm sample showing the highest quality. Of course, this improvement comes at the cost of increasing the growth time. For example, the 7.5 %In/μm buffer required 5.4 h compared to 0.68 h for the 60 % In/μm buffer.

The improved material quality for the slower buffer gradient also impacted device performance. Transmission electroabsorption modulators with a maximum $\Delta T/T_0$ of 22% at 1.34 μm were demonstrated. The amount of obtainable modulator increases as the buffer gradient decreases. In addition, photodetectors operating at 1.3 μm on GaAs substrates were shown to have reasonably low leakage currents and high internal quantum efficiencies. The sample with the most slowly graded buffer exhibited the highest measured quantum efficiency.

7. COMPARISON OF AlGaAs AND GaAs BARRIERS

7.1. Overview

This chapter describes a comparison of high In content InGaAs quantum wells with AlGaAs and GaAs barriers-particularly in terms of electroabsorption. A similar and more complete study was done on lower In content (20%) InGaAs on GaAs at Stanford in this research group.[17] That work showed that although InGaAs/AlGaAs exhibits inferior luminescence properties, it exhibits superior electroabsorption properties to InGaAs/GaAs. Thus very high performance modulators were produced using InGaAs/AlGaAs MQW. The previous study also presented theoretical calculations to determine the origin of this improved behavior. Briefly, most of the improvement comes from the shrinkage of the wavefunction in the x-y plane which accompanies the greater confinement in the growth direction. The rest of the enhancement is due to the larger overlap integral between the hole and electron wavefunctions in the deeper AlGaAs/InGaAs wells, which is mostly a result of the better confinement of the lighter mass electron.

This same theory applies to the case of high In content InGaAs/AlGaAs so no theory will be presented in this chapter. Rather the growth, materials characterization, and device performance will be discussed to confirm that like the low In content InGaAs, high In content InGaAs/AlGaAs shows superior electroabsorption to InGaAs/GaAs.

7.2. Structure and MBE Growth

The structure of the MBE-grown samples used in this work were similar to those described in Chapter 6. In fact, Sample II from Chapter 6 with the 15% In/μm grade was used as the InGaAs/AlGaAs sample for this study. For the InGaAs/GaAs sample, another p-i-n structure with an identical 15% In/μm linearly-graded InGaAs buffer layer and 5000 Å p-type $In_{0.35}Ga_{0.65}As$ cap layer was grown. For that sample, the MQW consisted of thirty 75 Å $In_{0.50}Ga_{0.50}As$ quantum wells with thirty-one 35 Å GaAs barriers. Using the same buffer gradient for the two samples was important for insuring that the comparison would elucidate the effect of the different barrier materials rather than the effect of the gradient.

7.3. Materials Characterization

7.3.1. Microscopy

The surface morphology of both samples showed the familiar cross-hatching similar to that seen in Chapter 6. No transmission electron microscopy was performed on the samples

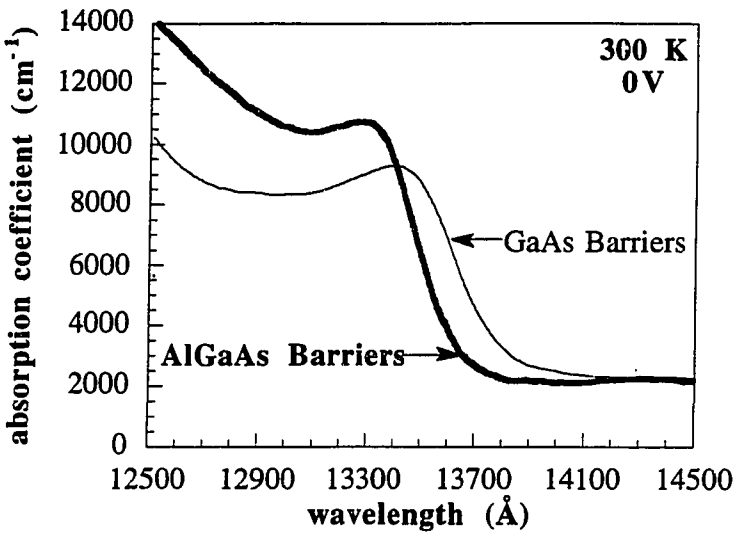

FIGURE 7.1 300 K zero field absorption spectra for samples with InGaAs/AlGaAs and InGaAs/GaAs MQW.

since they are expected to be structurally quite similar if not identical. Since the lattice constants of AlAs and GaAs are almost identical, the substitution of GaAs for AlGaAs should not make any difference in the amount of strain in the layer. We still expect the InGaAs quantum wells to be compressively strained atop the graded buffer and the AlGaAs or GaAs barriers to be tensilely strained. Thus similar morphologies in terms of dislocation structure would be expected for the GaAs and AlGaAs barrier samples.

7.3.2. Absorption Spectra

The zero field absorption spectra for both samples are shown in FIGURE 7.1. The measurements were done in the same manner as those described in Chapters 5 and 6. Both samples show a strong exciton peak. The sample with the AlGaAs barrier exhibits a sharper resonance at zero field. The HWHM of the AlGaAs barrier sample is about 14 meV compared with 18 meV for the GaAs barrier sample. The exciton peak for the AlGaAs barriers occurs at a shorter wavelength than the peak for the GaAs barrier sample in keeping with the stronger confinement due to the larger AlGaAs barriers.

7.4. Device Performance

7.4.1. Electroabsorption Modulator

7.4.1.1. Absorption Spectra

Under application of electric field, both samples exhibit the QCSE as shown in FIGURE 7.2 and may be used as electroabsorption transmission modulators. The AlGaAs sample has a stronger and sharper exciton resonance at zero field than does the GaAs sample and this continues with the application of field. At higher voltages such as 8V, the AlGaAs sample still has a well-defined exciton peak while the GaAs peak has become quite weak. Thus more field may be applied to the AlGaAs sample before the exciton dissociates and becomes too weak to produce a well-defined peak.

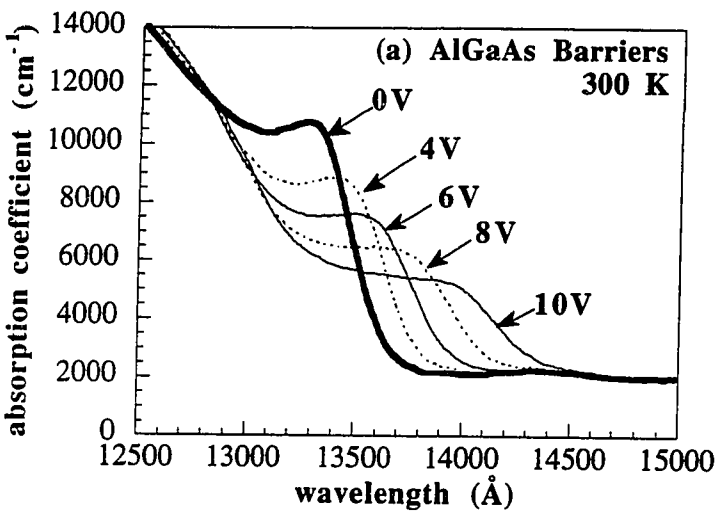

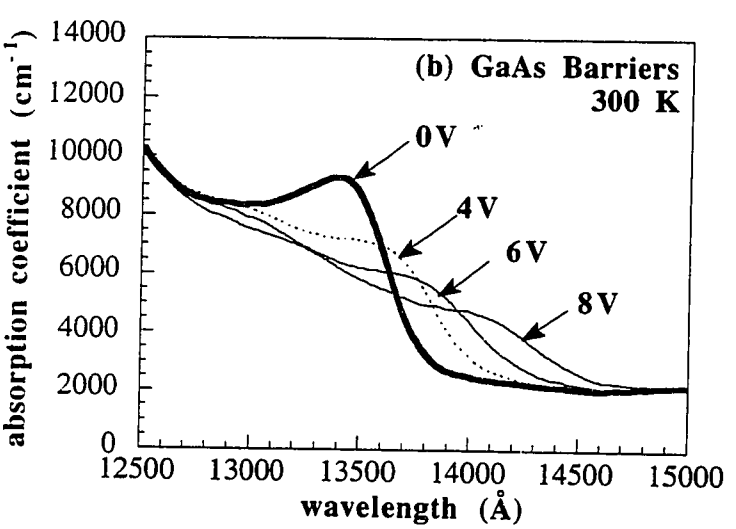

FIGURE 7.2 300 K absorption spectra at various reverse biases for (a) InGaAs/AlGaAs and (b) InGaAs/GaAs MQW.

These findings are consistent with those obtained for low In content InGaAs/AlGaAs versus InGaAs/GaAs.

7.4.1.2. Transmission

The maximum modulation achieved with the AlGaAs sample is larger than that achieved with the GaAs sample. This is largely due to the fact that a higher voltage may be applied to the AlGaAs sample without destroying the exciton. The maximum modulation for the GaAs and AlGaAs samples for normally-on and normally-off devices is indicated in TABLE 7.1. The value in % of the modulation and the wavelength in μm at which is occurred are also shown. The maximum modulation exactly at 1.3 μm was 6% and 3% for the AlGaAs and GaAs samples, respectively, at 8 V.

TABLE 7.1 Modulation characteristics for samples with GaAs and AlGaAs barriers.

Barrier	**Normally Off Max ΔT/T (+)**		**Normally On Max ΔT/T (-)**	
	%	μm	%	μm
GaAs	12	1.34	9	1.39
AlGaAs	18	1.33	14	1.37

7.4.2. Photodetector

7.4.2.1. Leakage Current

The sample with the GaAs barriers exhibited higher leakage current as expected due to the smaller confinement. For 500 x 500 μm devices under 9 V reverse bias, typical values for the leakage current were roughly 32 $\mu A/cm^2$ for the AlGaAs barriers and 1.2 mA/cm^2 for the GaAs barriers.

7.4.2.2. Responsivity and Quantum Efficiency

Since the responsivity and the quantum efficiency are directly proportional to the photocurrent, the relationships between the AlGaAs and GaAs barrier samples is illustrated in FIGURE 7.3 which shows their photocurrent versus wavelength under applied bias. Although at zero field, the efficiency and photocurrent for the GaAs barrier sample is higher, this advantage is countered by the exciton from the GaAs sample washing out with application of bias as low as 4 V. The exciton for the AlGaAs barrier sample holds together

under electric field much better than that of the GaAs sample. Since most practical devices require application of a voltage to act as a modulator, the GaAs barriers are generally a disadvantage. The GaAs sample might perhaps provide higher speed if only small absorption changes are required.

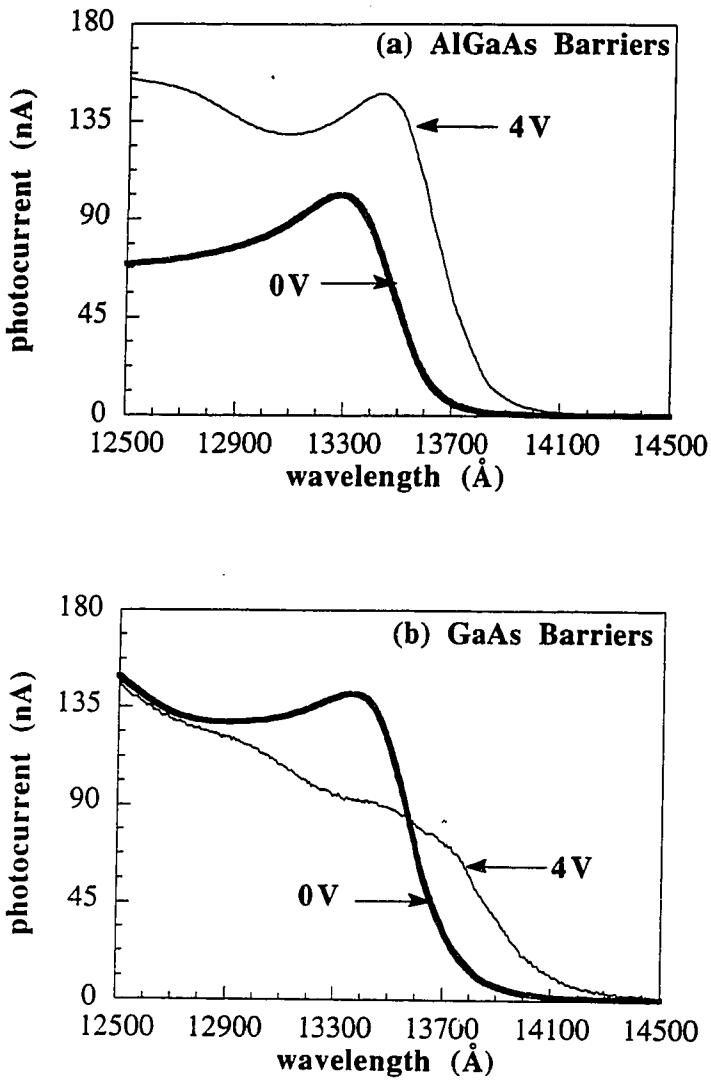

FIGURE 7.3 Photocurrent spectra at 0V (heavy line) and 4V (light line) applied bias for (a) AlGaAs barriers and (b) GaAs barriers.

Both samples had peak photocurrent of about 150 nA at 1.34 μm. This value occurred for 0V and 4V reverse bias for the GaAs and AlGaAs samples, respectively. The external

power was measured to be 1.3 μW at this wavelength. The external quantum efficiencies are calculated to be about 11% and the external responsivity 12 A/W. Both samples showed good internal quantum efficiency with peak values of 57% and 55% for the GaAs and AlGaAs samples, respectively. This suggests that there is no significant difference in efficiency between the samples with the AlGaAs and GaAs quantum wells.

7.5. Conclusions

InGaAs/AlGaAs has superior electroabsorption properties to InGaAs/GaAs for both low and high In content InGaAs grown on GaAs. This makes the InGaAs/AlGaAs samples more desirable for electroabsorption modulators. The AlGaAs barrier sample also allows for lower leakage current which is advantageous for photodetectors. The stronger confinement of the exciton with the larger AlGaAs barriers permits more voltage to be applied to the structure before washing out the resonance.

8. REFLECTION MODULATORS

8.1. Overview

Reflection modulators are capable of higher contrast ratios than transmission modulators[56] and are desirable for a number of applications. In this chapter, two techniques are described to produce reflection devices operating near 1.3 μm. The first approach involves a anti-reflection coating a transmission modulator and the second the integration of mirrors into the graded buffer layer. For each approach, the MBE growth and device performance will be discussed.

8.2. Anti-Reflection (AR) Coating

Without growing another device, the simplest approach to produce a reflection modulator is to use one of the solid gold contacts on a processed transmission device as a back mirror and then anti-reflection (AR) coat the backside to reduce the insertion loss. This involves only the deposition of the coating and subsequent measurement of the device. No new design, growth, or processing is required.

8.2.1. Structure and MBE Growth

FIGURE 8.1 shows a schematic of a reflection modulator produced by AR coating the backside of a transmission modulator. A processed device with a 15% In/μm linear gradient as described in Chapter 5 as Sample III was AR coated[152] with a single layer of Zr oxide. The profile was designed to yield a reflectivity of < 0.25% in the wavelength range from 1250 Å to 1350 Å and < 1% in the range from 1175 Å to 1425 Å. The coating was deposited at 300 °C and the epoxy[153] used in mounting the packaged device was stable. Another piece of the processed wafer was annealed for 30 min at 300 °C in a rapid thermal annealer (RTA) to simulate deposition conditions. Current-voltage measurements confirmed that no degradation took place under these conditions. Thus the deposition of the AR coating did not affect device performance.

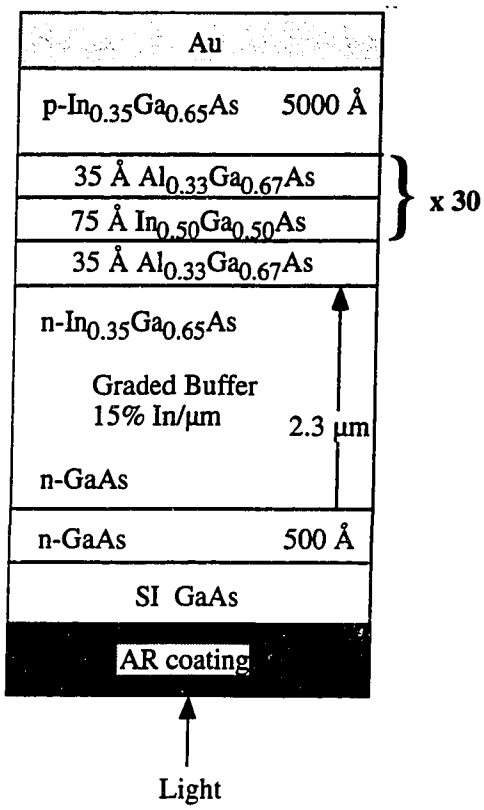

FIGURE 8.1 Schematic of AR-coated reflection modulator.

8.2.2. Reflectivity Results

During measurements, the light would be incident from the AR-coated side (previously the backside). A gold pad on the top of the device serves as one mirror. Unlike the one-pass transmission device, light incident on the AR-coated-side passes through the active area twice. This increases the degree of modulation. However, problems resulting from nonlinearities in the measurement system itself, particularly in the beam splitter and the spectrometer grating, complicate the data collection. These effects can be seen in FIGURE 8.2 which is the spectrum for the gold normalization standard. This standard is a neighboring section of the wafer comprised of the AR coating, substrate, n-type buffer, and Au contact. Thus no MQW are included in the normalization standard. The difficulty of obtaining precise values for this standard introduces an error into the determination of the exact magnitude of the reflectivity. This makes relative change in reflectivity, $\Delta R/R_0$, a

more reliable measurement than absolute reflectivity, R, or absolute change in reflectivity, ΔR, as defined by Equation 2-17.

Since the AR-coated device does not include a Fabry-Perot cavity, the observed reflectivity spectra shown in FIGURE 8.3 contains no sharp dips. The spectra are essentially the inverse of the transmission spectra observed in Chapter 5 for the transmission device with no AR coating. At low wavelengths, the reflectivity increases as wavelength increases while it becomes fairly flat at wavelengths much longer than the exciton. Several AR-coated devices were measured. Device A3 exhibited a $\Delta R/R_0$ of 22% at 1.27 μm and 1.32 μm with 20% at 1.30 μm between 0V and 10V as shown in FIGURE 8.3. These correspond to contrast ratios of 0.89 and 0.97 dB at 1.27 μm and 1.30 μm, respectively. At 1.27 μm, the insertion loss is roughly 1.87 dB. Device A2 appeared to have very high resistive losses. Accounting for this yields $\Delta R/R_0$ of 24% at 1.27 μm and 15% at 1.32 μm which is reasonable compared to the results for A3. Before AR-coating, this device was measured as a transmission modulator to have a $\Delta T/T_0$ of 17% at 1.27 μm corresponding to a contrast ratio of 0.68 dB with an insertion loss of roughly 4 dB. As expected, the performance of the device as an AR-coated reflection modulator is better than that as a transmission modulator.[154] The contrast ratio has increased while the insertion loss decreased.

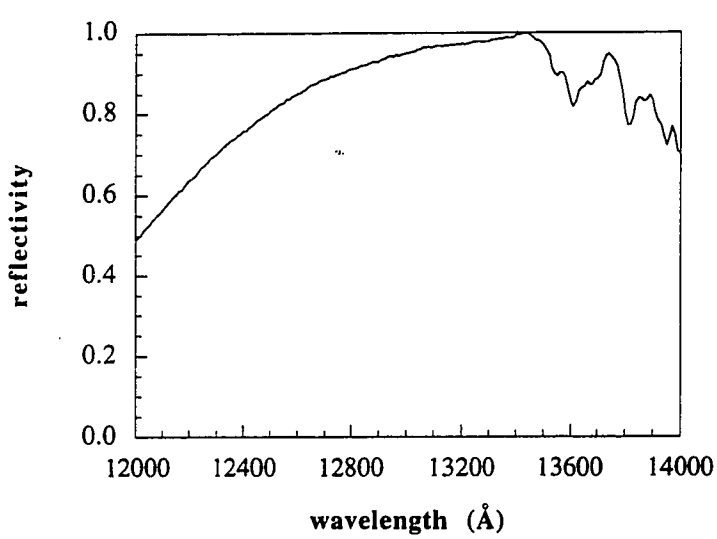

FIGURE 8.2 Reflectivity spectrum for AR-coated reflection modulator normalization standard.

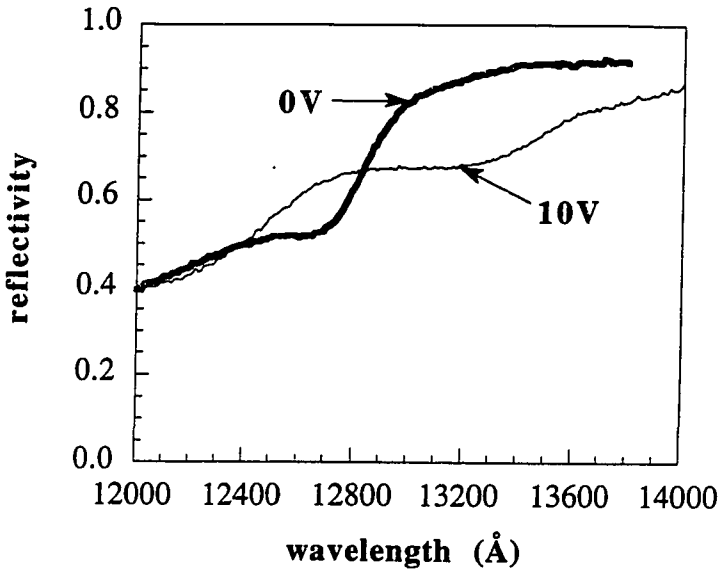

FIGURE 8.3 Reflectivity spectra for AR-coated reflection modulator at 0V (heavy line) and 10V (light line) reverse bias.

8.2.3. Discussion

AR coating the backside of a transmission device is a viable technique for the production of a reflection modulator. However, the difficulties in the measurement limit its usefulness. Also, the maximum modulation which can be expected is only twice that which can be achieved for the transmission device. Little can be done to optimize the device performance. A device which is grown as a reflection device offers more flexibility and promise.

8.3. Mirrors Integrated into Grading Layer

Reflection modulators require thick multi-layer mirror stacks to achieve sufficiently high reflectivity. As shown in Chapter 6, thicker buffer layers produce better quality InGaAs on GaAs.[155] Rather than growing separate thick layers to serve as mirror and buffer, we grew a single thick layer which served both functions. This is not a trivial procedure since the composition is changing throughout each layer which means the refractive index and the optical thickness is also changing. Experimental results for the MBE-grown device will be presented and compared with numerical simulations.

8.3.1. Structure and MBE Growth

An asymmetric Fabry-Perot (F-P) modulator was grown in a Varian Gen-II MBE system at 450 °C using As_2. A schematic of the p-i-n structure is shown in FIGURE 8.4. As shown in Chapter 4, the low growth temperature is important for high quality growth of high In content InGaAs on GaAs. The n-type region serves as both the linearly graded buffer layer and the quarter-wave mirror stack. The In composition in this region is graded from 0% In to 35% In in 45 Å steps at a rate of 7.5 %In/μm. The total thickness of the n-type region is about 4.6 μm which corresponds to 22 mirror periods where each period includes a layer of high index InAlAs and a layer of low index InGaAs. The layer thicknesses of 1140 Å InAlAs and 990 Å InGaAs are chosen to be quarter-wave for the average In composition of the graded region, i.e. 17% In. The undoped active layer of the modulator consists of thirty 75 Å $In_{0.50}Ga_{0.50}As$ quantum wells with thirty-one 35 Å GaAs barriers yielding an average MQW In composition of 34% In. 5000 Å of p-type $In_{0.35}Ga_{0.65}As$ caps the structure. The F-P cavity includes the MQW and the top p-type layer and must be an integral number of half-wavelengths for a high performance device. The InGaAs/air interface serves as the top mirror with a reflectivity of approximately 30%.

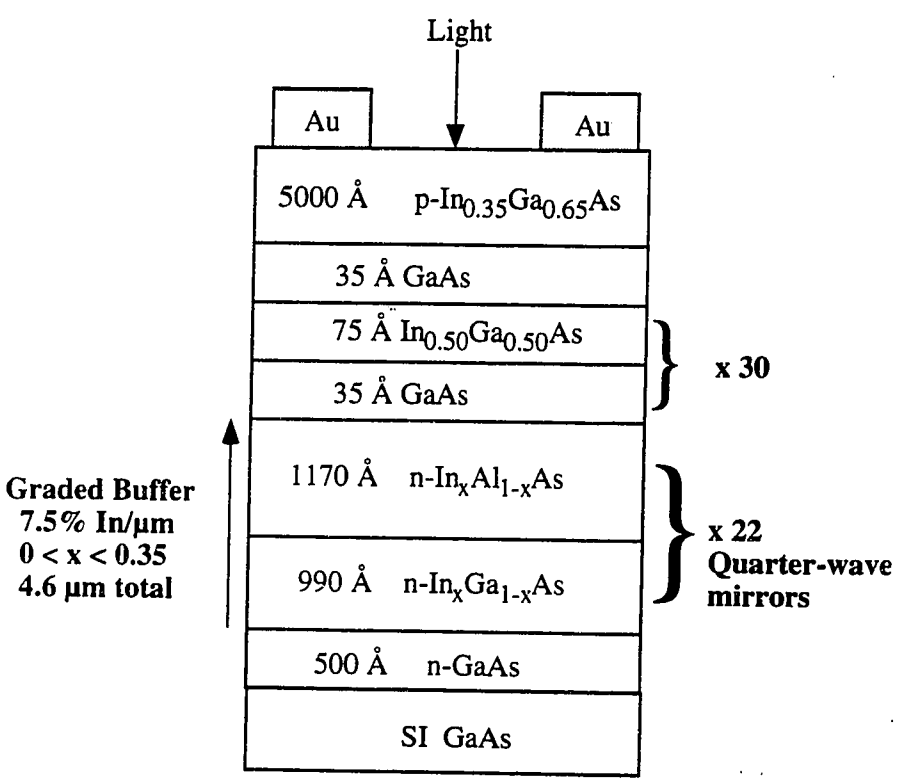

FIGURE 8.4 Schematic of integrated mirror reflection modulator.

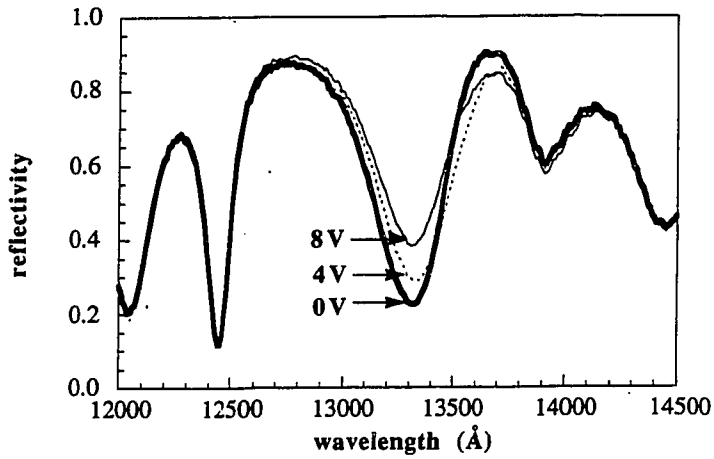

FIGURE 8.5 Reflectivity spectra for integrated mirror device at several reverse bias voltages.

After growth, the samples were etched down to the n-layer to form 500 x 500 μm square mesas. Electrical connections were made via an alloyed Au/Ge/Au contact to the n-layer and an annular Ti-Au contact to the top of the mesas. The room temperature reflectivity was measured as described in Chapter 2. Normalization was performed using a solid Au pad near the device under test as a standard. In order to match the wavelength of the F-P dip to that of the zero-field exciton, the processed device was etched in 3:1:250 H_3PO_4:H_2O_2:H_2O. Since the top mirror consists of just the semiconductor/air interface, etching this layer changes the position of the Fabry-Perot resonance without changing the top mirror reflectivity.[156] Thus the processed device was etched in 3:1:250 H_3PO_4:H_2O_2:H_2O to match the wavelength of the F-P dip to that of the zero-field exciton and optimize the cavity length. Since vertical cavity structures are quite sensitive to growth parameters, this ability to optimize the asymmetric structure after growth is very useful. Such an approach is particularly beneficial for this integrated mirror modulator since there was considerable uncertainty in the refractive index values used in designing the mirror.

8.3.2. Reflectivity: Experimental Results and Simulations

This device functions as a normally-off modulator with a large optical bandwidth as shown in the reflectivity spectra in FIGURE 8.5. A F-P dip is clearly seen at 1.33 μm where the reflectivity changes from 22% at 0V to 38% at 8V. This corresponds to a maximum modulation of 16% for ΔR and 73% for $\Delta R/R_0$. The modulation ratio (MR), defined by

Equation 2-18 as the ratio of maximum to minimum reflectivity, is 1.73. The contrast ratio, defined by Equation 2-19, is 2.38 dB. The large relative change in reflectivity, $\Delta R/R_0$, makes the device particularly attractive for application as a bistable self electro-optic device (SEED). The familiar features of a quarter-wave mirror spectrum, including a high reflectivity band from a wavelength of 12500 Å to 13900 Å and periodic dips on either side of this band, are evident. The reflectivity of this band is about 90%. Although the refractive index is changing continually due to the composition grading through the mirror layers, the accompanying variation of refractive index does not prevent the layers from forming a reliable quarter-wave mirror stack. Because the mirror was designed to be exactly quarter-wave for the average In composition of the graded region, i.e. 17%, the contributions from layers with lower and higher In content combine to yield a reasonable reflectivity spectra from the entire graded region.

Simulations were performed using the transfer matrix approach[157] which assumes abrupt changes occur at the interfaces. The same layer descriptions used in the computer control of the MBE growth were used in the computer simulations. In addition, the simulation takes into account the changing refractive index throughout the buffer layer. Comparison of the simulations with measured data is shown in FIGURE 8.6.

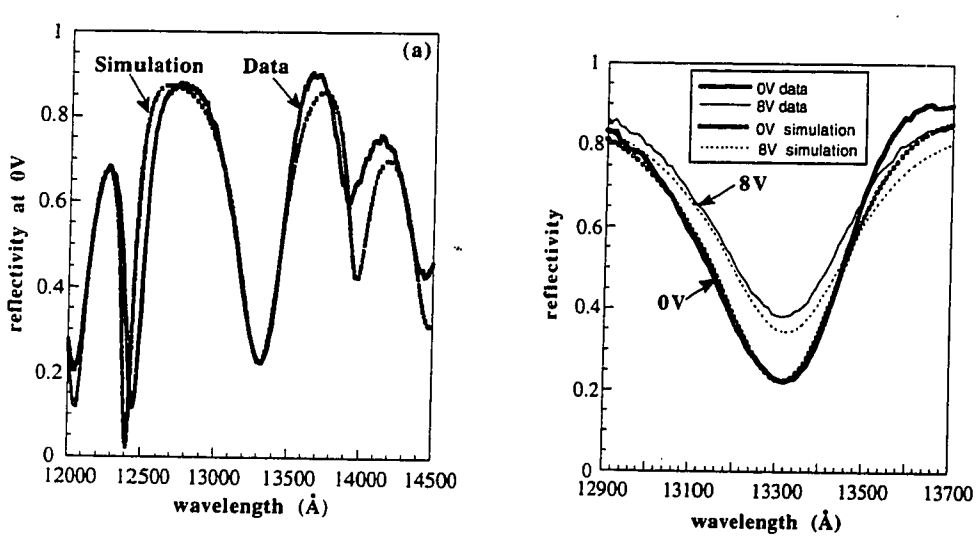

FIGURE 8.6 Comparison of reflectivity spectra for measured device (solid lines) and simulation (dotted lines) for (a) 0V applied bias and (b) 0V (heavy lines) and 8V (thin lines) applied bias.

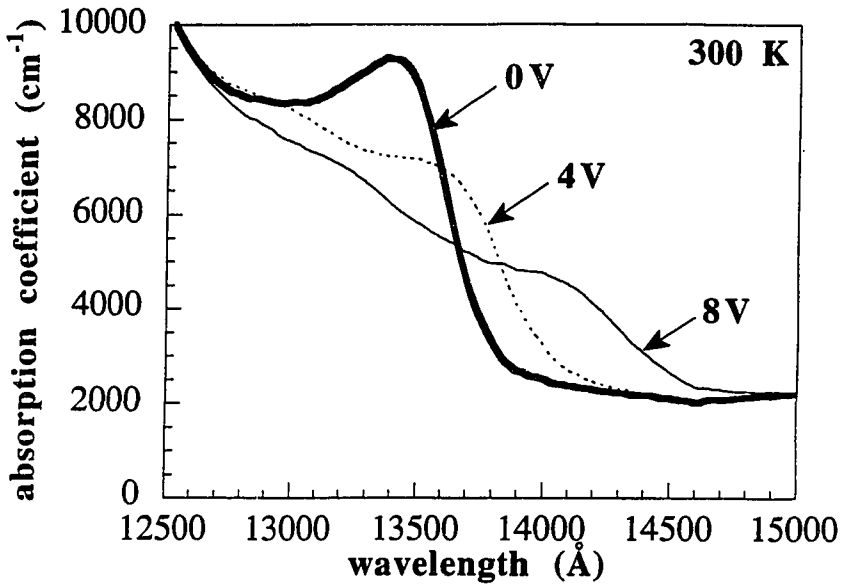

FIGURE 8.7 300 K absorption spectra for InGaAs/GaAs MQW at several reverse bias voltages.

The height of the high reflectivity band is accommodated in the simulation by adding additional absorption of about 1500 cm^{-1} in the top layer. Physically, however, this may be a result of the surface roughness, as the surface did show crosshatching which could lead to scattering or diffraction. As shown in Chapter 6, these samples have at least 40 Å of surface roughness as measured by atomic force microscopy (AFM).

In order to reasonably describe the voltage dependence of the modulator, the simulation also included absorption in the quantum wells. Data from a previously grown sample[158] with identical InGaAs/GaAs MQW grown atop a linearly graded InGaAs buffer graded at a rate of 15% In/μm was used. The absorption coefficient (α) versus wavelength at various reverse bias voltages for these MQW is shown in FIGURE 8.7. Due to variations in the In growth rate and the effect of changing the buffer gradient, the energy of the exciton peak was increased by 12.5 meV in the simulation to fit the data for the present device. The wide exciton resonances and their instability under high fields certainly limit the performance of the reflection modulator. At the zero field exciton position, the maximum $\Delta\alpha/\alpha$ estimated from FIGURE 8.7 is 34% or $\alpha_{max}/\alpha_{min}$ of 1.52. This relative

absorption change and the measured 38% maximum reflectivity, R_{max}, predict[56] a maximum MR of 1.72 in excellent agreement with the measured value of 1.73.

Design and simulation of the structure is complicated by the lack of reliable data for the refractive indexes of InGaAs and InAlAs as a function of composition and wavelength as described in Sections 2.2.2 and 2.2.3. Adjusting the values for refractive index given in those sections by 5% yields excellent agreement between the simulation and data for wavelengths close to the F-P dip as seen in FIGURE 8.6b. The simulation for 4V (not shown) is also in excellent agreement. The slight difference between the data and simulation for 8V may be due to differences in the exact electric field applied for the quantum wells used in the simulation and the modulator. Good qualitative agreement between the simulation and data in the wavelength range from 12000 Å to 14500 Å is shown in FIGURE 8.6a. The deviations away from the F-P dip may be explained by uncertainties in the dispersion for the mirror layers and possibly dispersion in the quantum wells which was not included in the simulation. In addition, this simulation technique itself is most accurate in the region close to the F-P dip. The simulation becomes more difficult for regions where the phase contributions from the bottom mirror become significant i.e. in regions where the phase is changing rapidly. Since this is also the region of interest for the operation of devices, this simulation is useful for predicting the behavior of practical devices.

8.3.3. Discussion

Device performance may be optimized in several ways. Adjustment of the In composition in the MQW could maximize the modulation at 1.3 μm. Using AlGaAs rather than GaAs barriers would enhance the electroabsorption of the MQW and increase the ratio of maximum to minimum absorption.[17] Increasing the cavity length would also improve the modulation ratio but would necessitate operating at a higher voltage. Incorporating a quarter-wave stack to increase the front mirror reflectivity would sharpen the F-P dip and improve contrast if the front mirror reflectivity were matched to the effective back mirror reflectivity (R_b plus cavity absorption). However, the higher front mirror reflectivity would also lower the optical bandwidth.

Simply incorporating a quarter-wave stack to increase the front mirror reflectivity will not necessarily improve the device's performance. For example, using a similar low temperature linearly-graded InGaAs buffer, Fritz et al.[159] reported a normally-on reflection modulator operating at 1.33 μm. In their asymmetric Fabry-Perot structure, the top mirror

included 4 periods for a targeted reflectivity of 72%. Higher performance might be expected from their more complicated structure. However, their maximum reported $\Delta R/R$ is only 68% which is comparable to our value of 73%. An advantage of our structure with the lower front mirror reflectivity is the ability to optimize after growth by etching. The breakdown field for the device reported by Fritz et al. was approximately 1.0×10^5 V/cm which is three times smaller than that observed for our integrated mirror device. Their modulator was considerably thicker than ours as it included separate layers for the buffer and the mirror. Their bottom mirror, composed of layers of InGaAs and InAlAs, was 4.1 μm thick. In addition, their buffer included a 2.5 μm graded layer plus a 2000 Å constant composition layer of $In_{0.33}Ga_{0.67}As$. Even with their mirror and buffer separated, the magnitude of their high reflectivity band was similar to our observed 90%. These results suggest that our scheme of integrating the mirror into the graded buffer has not compromised device performance while significantly reducing both thickness and growth time. The reduced thickness is especially important for monolithic integration of modulators with other devices for applications such as smart pixels.

8.4. Conclusions

Electroabsorption reflection modulators operating at the 1.3 μm telecommunications wavelength have been demonstrated on GaAs substrates using two techniques: AR coating and integrating mirrors into the linearly-graded buffer. We demonstrated that quarter-wave mirrors may be grown in a linearly-graded region which also serves as a buffer to permit growth of high In content InGaAs. The high reflectivity band, from such a mirror, is reasonably flat and its position, width, and height agree well with simulations. Due to its flexibility and potential for improved performance and integration with other devices, the integrated mirror approach appears more promising for future applications. At 1.33 μm, a normally-off reflection modulator with an integrated mirror exhibited a $\Delta R/R_0$ of 73% , a contrast ratio of 2.38 dB, and an insertion loss of 4 dB. Comparing our integrated mirror Fabry-Perot device to our AR-coated reflection device reveals an improvement of 1.52 dB in contrast ratio with a penalty of about 2 dB in insertion loss. A significant advantage of this novel integrated approach is the reduction in MBE growth time and device thickness. Such integrated mirrors could be incorporated into a variety of devices including vertical cavity surface emitting lasers and might prove useful for long wavelength operation of such devices.

9. CONCLUSIONS

9.1. Summary

In this thesis, the growth of high In content InGaAs on GaAs substrates for optical applications has been demonstrated. Low temperature growth was shown to be particularly important for the growth of high In content InGaAs on GaAs. This work includes the first reported observation of excitons and the quantum confined Stark effect at 1.3 μm on GaAs substrates which significantly extends the usable wavelength for optical devices on GaAs. The key to this achievement is the incorporation of a linearly-graded buffer layer beneath the multiquantum wells. Linear-grading was shown to be superior to step-grading for producing good quality high In content InGaAs on GaAs. Although dislocations were observed within the linearly-graded buffer layers, under transmission electron microscopy, none were observed to be threading up through the multiquantum wells. Thus they exhibited no deleterious effects on the active layer. Linear gradients of up to and including 4% mismatch/μm (60% In/μm) were shown to yield material with reasonable excitonic behavior. No critical gradient was observed above which excitons were not visible. However, material grown with an abrupt step grading exhibited no excitonic effects. Thus a critical gradient does exist somewhere above 4% mismatch/μm. As the buffer gradient decreases, the material quality improved. This may be due to more relaxation occurring within the buffer layer for the more slowly graded samples.

These good quality high In content InGaAs multiquantum wells grown atop linearly-graded buffers were also used in devices. This work included the first demonstration of an electroabsorption modulator operating at 1.3 μm on GaAs. This was a transmission device. The improved material quality for the slower buffer gradient impacted device performance. The amount of obtainable modulator increased as the buffer gradient decreased with the maximum reported $\Delta T/T_0$ being 22% at 1.34 μm. In addition, photodetectors operating at 1.3 μm on GaAs substrates were shown to have reasonably low leakage currents and high internal quantum efficiencies. The sample with the most slowly graded buffer exhibited the highest measured quantum efficiency. The use of GaAs and AlGaAs as barrier materials for high In content InGaAs quantum wells was investigated. This work confirmed that high In content InGaAs/AlGaAs exhibits superior electroabsorption properties to GaAs/AlGaAs.

Electroabsorption reflection modulators operating at 1.3 μm on GaAs substrates were demonstrated using two techniques: AR coating a transmission modulator and integrating

mirrors into the linearly-graded buffer. Due to its flexibility and potential for improved performance and integration with other devices, the integrated mirror approach appears more promising for future applications. At 1.33 μm, a normally-off reflection modulator with an integrated mirror exhibited a $\Delta R/R_0$ of 73% , a contrast ratio of 2.38 dB, and an insertion loss of 4 dB. This is the first demonstration that quarter-wave mirrors may be grown in a linearly-graded buffer region of a device. A significant advantage of this novel integrated approach is the reduction in MBE growth time and device thickness.

9.2. Suggestions for Future Work

A number of interesting areas for future research are suggested by the work presented in this dissertation. InGaAs devices operating on GaAs at the 1.55 μm loss minima for silica fibers should also be possible using this technique of linear grading. In addition, further materials optimization might permit the production of other optical and electronic devices on GaAs with high In content including 1.3 μm lasers. Although this work focused on MBE growth, the technique should be applicable to other epitaxial growth methods.

To optimize devices operating exactly at 1.3 μm, a careful study would need to be conducted to gain better control over the process. More information would be needed on the degree of relaxation occurring within the buffers. RHEED done during the growth, perhaps after the growth of the buffer, might be useful. Further X-ray diffraction work on structures with only graded buffers would also be helpful.

Further efforts to optimize the material quality of high In content InGaAs grown on GaAs might include investigating variations of traditional MBE, such as migration enhanced epitaxy (MEE) or use of growth interruptions. Adjustments to the Group V/Group III flux ratio might prove beneficial. Annealing (in situ or ex situ) might prove useful. Studies of the effect of arsenic species (As_2 vs. As_4) might prove interesting. More TEM work would certainly be useful to fully understand the novel mechanisms of dislocation nucleation and interaction in this system. Efforts to understand and eliminate the surface crosshatching would be particularly valuable for array applications. More accurate characterization of the defect densities and reducing them to below levels observed in GaAs/Si (about 10^7 cm^{-2}) would extend the practicality of these materials for device applications. Extending this to the growth of InGaAs on silicon substrates is another promising area for study. Finally, the modulators and photodetectors could be optimized for specific device applications including extending the thickness of the intrinsic quantum well region to about 1 μm.

The ability to grow good quality high In content InGaAs on GaAs offers a range of possibilities for applications beyond those presented here. For example, intersubband transitions in the conduction band of such materials may be used as long wavelength (3-5 μm) quantum well infrared photodetectors (QWIP).[160] Intersubband transitions within the valence band present interesting physics as well as device applications. This technique could also be used to make electronic transport devices such as heterojunction bipolar transistors (HBTs).

The importance of this thesis work extends beyond the results achieved. The successful incorporation of highly mismatched layers into a device is promising for extending strained layer epitaxy beyond materials systems involving only small mismatches. This enhances the possibilities for growth of a multitude of technologically interesting materials on the relatively small number of available high quality substrates.

APPENDIX PROCESSING FOR P-I-N STRUCTURES

•Cleave quarter-wafer
•DI rinse-put sample in boat
•Degrease
-acetone
-methanol
-blow both sides dry with N2
Always blow dry methanol not acetone

•Singe in VWR 1300U oven at 170°C for about 10 minutes to drive off water

•Blow dry (remove any dust from oven)
•APPLY PR
•Clean the spinner chuck with acetone
•Place wafer on chuck. Turn on vacuum. Apply primer. Spin for 30 sec
•Apply Shipley 1813 Photoresist (PR) to cover wafer. Spin for 30 sec.
For structures including AlAs layers, use 3500 rpm; otherwise use 5000 rpm
•Remove wafer from chuck. Clean off the back with acetone on a piece of folded clean wipe-don't want uneven PR on backside later.
•20 min in 80°C oven

FIRST MASK STEP- use ETCH

blow off mask with N2
silver side of mask down on aligner (letters backwards through microscope)
make note of orientation of wafer on chuck (to make it easier for next mask step)
align wafer 90° to the pattern (rectangles 90° to flat, align edge of wafer to long lines)
Be sure mask is straight first-be sure both eyepieces are looking at same row on wafer.
move whole eyepiece assembly if not. (silver knob in back to adjust)
don't look at aligner when lamp is on
only need to align on 5X eyepiece for this step, adjust half with xy, and half with theta
Look at log to see times people are using for exposure
Might want to expose a dummy wafer first

•For 3500 rpm resist, use 8 sec exposure. For 5000 rpm resist, use 5 sec exposure.

•After developing for about 50 sec, rinse in DI for at least 3 minutes while swirling. Blow top dry with N2.

•20 min in 88°C oven or about 10 min in 120°C oven
•Measure height of PR on Dektak (so can check depth of etch)

•**ETCH** down through p and intrinsic layers to reach about one-quarterway in n layer

For structures not involving AlAs, use

3:1:50 H_3PO_4:H_2O_2:H_2O	at 20°C this etches	GaAs	750Å/min
		$Al_{0.3}GaAs$	1000Å/min

For structures involving AlAs, use

5:1:1 H_2SO_4:H_2O_2:H_2O	at 20°C	GaAs	240Å/s

To prepare solution mix acid and water. Let sit in bath for a while until cooler. Then add peroxide.

•Rinse in DI
•Check etch depth on Dektak, make sure it is sufficient at several points on wafer
•Repeat etch if necessary
•When satisfied with etch, soak in acetone to remove PR
•Methanol rinse, blow dry with N2
•15 min in 120°C oven

<u>SECOND MASK STEP-use OHMIC 2</u>

Devices on n+ substrates have backside contacts. Don't need OHMIC2 mask step.
Devices on SI substrates need front contacts made using OHMIC2.

•Spin on primer, then PR @ 3500 rpm
•Remove PR from backside of wafer
•20 min in 88°C oven

•**ALIGN**

Be sure that mask is aligned first with itself i.e. straight line across both eyepieces (use silver knob on back right to adjust this)
Mask Frame Lock on when aligning
If wafer too small to see in both eyepieces

Choose a big box on the mask. Align one corner of the wafer using x and y. Move to another edge and use tilt to adjust. Repeat this using the tilt for half of the adjustment and x-y for the rest until all aligned. Do this on 5X. Then repeat on 10X with alignment marks.

For first alignment, there are 3 alignment patterns with Es in them. Align the center one of these with the appropriate box with a P above it. Get all 4 rectangles within the box.

If wafer not straight, may need to contact to look at it, then release to adjust it. consider using Chuck release also when exposing.

Adjust tilt of wafer (rotation)

Adjust position (x-y)

•**EXPOSE**

•Develop for about 50 sec

•DI Rinse for a minimum of 3 minutes

•**FORM N-TYPE CONTACT IN EVAPORATOR**

use Au/Ge/Ni/Au 400/100/125/1500 Å

•Remove PR/Lift-off metal using acetone. May need to let sit for a while. Overnight is best. Needs several hours at the least. Squirt with acetone but do not use tweezers as they scratch the gold. Use ultrasonic shaker. Can heat acetone but it boils at 56°C so be careful. Can use small Q-tips if careful and PR is being stubborn.

•Be sure that backside is clean (especially if interested in transmission measurements)

• Alloy in RTA-410°C for 30 sec (use program bard.RCP for example)

•Check contacts with hp 4145 semiconductor parameter analyzer in McC 61. Check for connection between gold on different dies.

<u>THIRD MASK STEP-use OHMIC 1</u>

•Rinse in DI

•Degrease (acetone, methanol, blow dry with N2)

•15 min in 120°C oven

•Spin on primer, then PR

•Remove PR from backside of wafer

•20 min in 88°C oven

•**ALIGN**

•EXPOSE

•Develop for about 50 sec
•DI Rinse for a minimum of 3 min
•(optional: 10 min in 88°C oven)
•10 sec in 1:10 HCl:H_2O (to remove oxide to facilitate making a better contact)
•Rinse in DI (NO Methanol)
•Blow dry with N2
•Immediately put in evaporator
•Let evaporator pump down for a while to get to good base pressure

•FORM p-type contact in evaporator

use Ti/Au 400/1200 Å (Ti helps Au stick) NO anneal

•Remove PR/Lift-off metal using acetone. May need to let sit for a while. Overnight is best. Needs several hours at the least. Squirt with acetone but do not use tweezers as they scratch the gold. Use ultrasonic shaker.

•Use micromanipulator and hp 4145 to verify that devices really are diodes before doing any further testing!

General Information

Developer mixture is 50:50 developer:water
To clean PR syringe, rinse in acetone and methanol. Bake at 120 °C.
If spinner won't hold vacuum, clean out vacuum line with acetone after disconnecting hose carefully.
Primer is not diluted.
Masks designed by Dominique Thomas.

REFERENCES

[1]At 1.3 μm, dispersion as low as ps/nm-km achieved. For example, see J. Wilson and J. F. B. Hawkes, *Optoelectronics: An Introduction*, (Prentice-Hall International, Englewood Cliffs, New Jersey, 1983), p. 390.

[2]B. Pezeshki, R. B. Apte, S. M. Lord, and J. S. Harris, Jr., IEEE Photon. Technol. Lett. **3**, 790 (1991).

[3]U. Keller, G. W.'t Hooft, W. H. Knox, and T. K. Woodward, Paper WB2 in Proc. OSA Quantum Optoelectronics Top. Meet., Salt Lake City, UT, 1991.

[4]D. A. B. Miller, Int. J. High Speed Electron. **1**, 19, (1990).

[5]D. W. Anthon, A. T. Eggleston, S. G. Grubb, J. G Kwasegroch, P. A. Leilabady, and D. L. Snipes, Paper TuT1 in OSA Annual Meeting Technical Digest 1992 (Optical Society of America, Washington D.C., 1992), Vol. 23, p.64.

[6]T. K. Woodward, T. Sizer, II, D. L. Sivco, and A. Y. Cho, Appl. Phys. Lett. **57**, 548 (1990).

[7]J. E. Cunningham, K. W. Goossen, M. Williams, and W. Y. Jan, Appl. Phys. Lett. **60**, 727 (1992).

[8]after J. C. Bean in *High Speed Semiconductor Devices*, S. M. Sze, Ed, (Wiley-Interscience, New York, 1990), p.25.

[9]H. Tanaka and M. Mushiage, J. Cryst. Growth **111**, 1043 (1991).

[10]for example, see D. K Ferry, ed. *Gallium Arsenide Technology*, (W. Sams, Indianapolis, Indiana, 1985).

[11]For example, see E. C. Larkins and J. S. Harris, Jr., "Molecular Beam Epitaxy of High Purity GaAs and AlGaAs," to be published in R. Farrow and J. Arthur, Ed., *Molecular Beam Epitaxy*, (Noyes Publications, New Jersey).

[12]S. Adachi, J. Appl. Phys. **58**, R1 (1985).

[13]J.-P. Reithmaier, R. Hoger, H. Riechert, P. Hiergeist, G. Abstreiter, and G. Weimann, Appl. Phys. Lett. **56**, 536 (1990).

[14]P. Win, Y. Druelle, P. Legry, S. Lepilliet, A. Cappy, Y. Cordier, and J. Favre, Electr. Lett. **29**, 169 (1993) and examples from the 13th Annual GaAs IC Symposium Technical Digest, Monterey, CA, Oct. 1991.

[15]H. Ito and J. S. Harris, Jr., Electr. Lett. **28**, 655 (1992).

[16]L. E. Eng, A. Sa'ar, T. R. Chen, I. Grave, N. Kuze, and A. Yariv, Appl. Phys. Lett. **58**, 2752 (1991).

[17]B. Pezeshki, S. M. Lord, and J. S. Harris, Jr., Appl. Phys. Lett. **59**, 888 (1991).

[18]A. Fischer-Colbrie, J. N. Miller, S. S. Laderman, S. J. Rosner, and R. Hull, J. Vac. Sci. Technol. B **6**, 620 (1988).

[19]B. Laikhtman, R. A. Kiehl, D. J. Frank, J. Appl. Phys. **70**, 1531 (1991).

[20]G. H. Olsen, C. J. Neuse, and R. T. Smith, J. Appl. Phys. **49**, 5523 (1978).

[21]C. P. Kuo, D. Hou, S. J. Lee, D. L. Miller, and R. J. Anderson, GaAs IC Symposium Technical Digest 162 (1983).

[22]J. Massies and M. Sauvage-Simkin, Appl. Phys. Lett. **43**, 8465 (1983).

[23]R. K. Willardson and A. C. Beer, Eds. *Semiconductors and Semimetals*, Vol. 33 (Academic Press, New York, 1991), p.88.

[24]S. Adachi, J. Appl. Phys. **53**, 8775 (1982).

[25]This does not include possible increases in $\Delta E_C/\Delta E_V$ at larger compressive strains reported by M. J. Joyce, M. J. Johnson, M. Gal, and B. F. Usher, Phys. Rev. B **38**, 10978 (1988) and B. Jogai, Appl. Phys. Lett. **59**, 1329 (1991).

[26]E. D. Palik, ed., *Handbook of Optical Constants of Solids*, (Academic Press, New York, 1985).

[27]H. W. Dinges, H. Burkhard, R. Losch, H. Nickel, and W. Schlapp, Appl. Surf. Sci. **54**, 477 (1992).

[28]T. Takagi, Jap. J. Appl. Phys. **17**, 1813 (1978).

[29]S. H. Wemple and M. DiDomenico, Jr., Phys. Rev. B **3**, 1338 (1971).

[30]M. A. Afromowitz, Solid State Comm. **15**, 59 (1974).

[31]J. R. Arthur and J. J. LePore, J. Vac. Sci. Technol. **6**, 545 (1969).

[32]A. Y. Cho, Surf. Sci. **17**, 494 (1964).

[33]A. Y. Cho and J. R. Arthur, Proc. Solid State Chem. **10**, 157 (1975).

[34]J. R. Arthur, J. Appl. Phys. **39**, 4032 (1968).

[35]L. L. Chang and K. Ploog, *Molecular Beam Epitaxy and Heterostructures*, (Martinus Nijhoff Publishers, Boston, 1985).

[36]E. C. Larkins and J. S. Harris, Jr., "Molecular Beam Epitaxy of High Purity GaAs and AlGaAs," to be published in R. Farrow and J. Arthur, Ed., *Molecular Beam Epitaxy*, (Noyes Publications, New Jersey).

[37]J. J. Harris, B. A. Joyce, and P. J. Dobson, Surf. Sci. **103**, L90 (1981).

[38]J. H. Neave, B. A. Boyce, P. J. Dobson, and N. Norton, Appl. Phys. A. **31**, 1 (1983).

[39]D. G. Schlom, personal communication.

[40]R. -L. Lee, W. J. Schaffer, Y. G. Chai, D. Liu, and J. S. Harris, Jr., J. Vac. Sci. Technol. B **4**, 568 (1986)

[41]J. C. Garcia, A. Barski, J. P. Contour, and J. Massies, Appl. Phys. Lett. **51**, 593 (1987).

[42]C. T. Foxon and B. A. Joyce, Surface Science **50**, 434 (1975).

[43]C. T. Foxon and B. A. Joyce, Surface Science **64**, 293 (1977).

[44]R. N. Sacks, D. W. Eichler, R. A. Pastorello, and P. Colombo, J. Vac. Sci. Technol. B **8**, 168 (1990).

[45]C. T. Foxon, P. Dawson, and G. Duggan, Coll. Papers 2nd Int. Symposium on MBE and Related Clean Surf. Techniques, 81 (1982).

[46]E. C. Larkins, E. S. Hellman, D. G. Schom, J. S. Harris, Jr., M. H. Kim, and G. E. Stillman, J. Cryst. Growth **81**, 344 (1987).

[47]W. Tsang, IEEE Circuits and Devices Magazine, September 1988, p.18.

[48]R. G. Hunsperger, *Integrated Optics: Theory and Technology*, (Springer-Verlag, New York, 1985), ch. 8, p.120.

[49]For example, see the proceedings from the OSA Topical Meetings on Quantum Optoelectronics, Palm Springs, CA, March 1993 or Salt Lake City, UT, March 1991.

[50]G. Bastard, *Wave Mechanics Applied to Semiconductor Heterostructures*, (Les Editions de Physique, France 1988), p. 71.

[51]G. Bastard, E. E. Mendez, L. L. Chang, and L. Esake, Phys. Rev. B **26**, 1974 (1982).

[52]R. C. Miller and D. A. Kleinman, J. Luminescence **30**, 520 (1985).

[53]A. M. Fox, D. A. B. Miller, G. Livescu, J. E. Cunningham, J. E. Henry, and W. Y. Jan, Appl. Phys Lett. **57**, 2315 (1990).

[54]D. A. B. Miller, D. S. Chemla, T. G. Damen. A. C. Gossard, W. Wiegmann, T. H. Wood, and C. A. Burrus, Phys. Rev. B **32**, 1043 (1985).

[55]The quantum wells shown are Type I quantum wells where the electrons and holes are localized in the same material. InGaAs/AlGaAs forms Type I quantum wells so only Type I are described in this thesis. Type II quantum wells do exist for some materials systems. For more information, see for example, G. Danan, B. Etienne, F. Mollot, R. Planel, A. M. Jean-Louis, F. Alexandre, B. Jusserand, G. Le Roux, J. Y. Marzin, H. Sarary, and B. Sermge, Phys. Rev. B **35**, 6207 (1987) or J. Ihm, Appl. Phys. Lett. **50**, 1068 (1987).

[56]B. Pezeshki, D. Thomas, and J. S. Harris, Jr. Appl. Phys. Lett. **57**, 1491 (1990).

[57]Transmission for wavelengths around GaAs may be done with monochromatic light (light in end of spectrometer), focused through a camera lens on the sample. Using an IR viewer, one can view where the light is hitting and insure that only the desired device is

illuminated. A photodetector is placed above the sample to collect the signal. However, for the long wavelength devices discussed in this work, this method does not work because insufficient light can be seen through the device with the IR viewer available at Stanford although perhaps an IR viewer with a longer wavelength range would make it possible.

[58] Also assumes normal incidence and monochromatic light.

[59]S. M. Sze, *Physics of Semiconductor Devices*, (Wiley-Interscience, New York, 1981), ch. 13, p.743.

[60]G. C. Osbourn, J. Appl. Phys. **53**, 1586 (1982).

[61]R. K. Willardson and A. C. Beer, Eds., *Semiconductors and Semimetals*, Vol. 32 "Strained Layer Superlattices: Physics," (Academic Press, New York, 1991).

[62]R. K. Willardson and A. C. Beer, Eds., *Semiconductors and Semimetals*, Vol. 33 "Strained-Layer Superlattices: Materials Science and Technology," (Academic Press, New York, 1991).

[63]G. C. Osbourn, Phys. Rev. B **27**, 5126, (1983).

[64]J. W. Matthews and A. E. Blakeslee, J. Cryst. Growth **27**, 118 (1974).

[65]W. D. Nix, Metallurgical Trans. A, **20A**, 2217 (1989).

[66]I. J. Fritz, S. T. Picraux, L. R. Dawson, T. J. Drummond, W. D. Laidig, and N. G. Anderson, Appl. Phys. Lett. **46**, 967 (1985).

[67]T. G. Andersson, Z. G. Chen, V. D. Kulakovskii, A. Uddin, and J. T. Vallin, Appl. Phys. Lett. **51**, 752 (1987).

[68]T. G. Andersson, M. J. Ekenstedt, V. D. Kulakovskii, S-M. Wang and J-Y. Yao, Proc. SPIE **1361**, 434 (1990).

[69]M. J. Ekenstedt, S. M. Wang, and T. G. Andersson, Appl. Phys. Lett. **58**, 854 (1991).

[70]P. R. Berger, K. Chang, P. K. Bhattacharya, and J. Singh, J. Vac. Sci. Technol. B **5**, 1162 (1987).

[71]J. Y. Yao, T. G. Andersson, and G. L. Dunlop, Appl. Phys. Lett. **53**, 1420 (1988).

[72]B. Elman, E. S. Koteles, P. Melman, and M. Rothman, Proc. SPIE **1361**, 362 (1990).

[73]K. H. Chang, R. Gibala, D. J. Srolovitz, P. K. Bhattacharya, and J. F. Mansfield, J. Appl. Phys. **67**, 4093 (1990).

[74]R. People and J. C. Bean, Appl. Phys. Lett. **47**, 322 (1985) and **49**, 229 (1986).

[75]B. W. Dodson and J. Y. Tsao, Appl. Phys. Lett. **51**, 1325 (1987), **52**, 852 (1988), and **53**, 848 (1988).

[76]C. W. Snyder, J. F. Mansfield, and B. G. Orr, Phys. Rev. B **46**, 9551 (1992).

[77]see for example MRS Fall Meeting 1992, Boston, MA, Symposium B and R. K. Willardson and A. C. Beer, Eds., *Semiconductors and Semimetals*, Vol. 33 "Strained-

Layer Superlattices: Materials Science and Technology," (Academic Press, New York, 1991), Ch. 3.

[78]E. A. Beam III and Y. C. Kao, J. Appl. Phys. **69**, 4253 (1991).

[79]E. A. Fitzgerald, G. P. Watson, R. E. Proano, D. G. Ast, P. D. Kirchner, G. D. Pettit, and J. M. Woodall, J. Appl. Phys. **65**, 2220 (1989).

[80]J. W. Matthews, A. E. Blakeslee, and S. Mader, Thin Solid Films **33**, 253 (1976).

[81]P. Ribas, V. Krishnamoorthy, and R. M. Park, Appl. Phys. Lett. **57**, 1040 (1990).

[82]V. Krishnamoorthy, Y. W. Lin, and R. M. Park, MRS Spring Meeting 1992, San Francisco, CA, Paper F7.9.

[83]P. Melman, B. Elman, C. Jagannath, E. S. Koteles, A. Silletti, and D. Dugger, Appl. Phys. Lett. **55**, 1436 (1989).

[84]O. Brandt, L. Tapfer, K. Ploog, M. Hohenstein, and F. Phillipp, J. Cryst. Growth **111**, 383 (1991).

[85]T. C. Hasenberg, D. S. McCallum, X. R. Huang, A. L. Smirl, M. D. Dawson, and T. F. Boggess, J. Cryst. Growth **111**, 388 (1991).

[86]M. Yano, K. Yoh, T. Iwawaki, Y. Iwai, and M. Inoue, J. Cryst. Growth **111**, 397 (1991).

[87]H. Toyoshima, K. Onda, E. Mizuki, N. Samato, M. Kuzuhara, T. Itoh, A. Okamoto, TY. Anan, and T. Ichihashi, J. Appl. Phys. **69**, 7697 (1991).

[88]J. Lopata, N. K. Dutta, and N. Chand, MRS Fall Meeting 1992, Boston, MA, Paper D5.42.

[89]E. J. Roan and K. Y. Chang, Appl. Phys. Lett. **59**, 2688 (1991).

[90]S. Niki, W. S. C. Chang, H. H. Wieder, and T. E. Van Eck, J. Cryst. Growth **111**, 419 (1991).

[91]S. Niki, A. Cheng, J. C. P. Chang, W. S. C. Chang, and H. H. Wieder, Jap. J. Appl. Phys. **29**, L1833 (1990).

[92]T. E. Van Eck, S. Niki, P. Chu, W. S. C. Chang, H. H. Wieder, A. J. Mardinly, K. Aron, and G. A. Hansen, Paper WA3-1 in Quantum Wells for Optics and Optoelectronics Topical Meeting, Salt Lake City, UT, 1989.

[93]J. Aspell, Paper CMB1 in Conference on Lasers and Electro-Optics 1992 Technical Digest, (Optical Society of America, Washington, D. C. 1992), Vol. 12, p.6.

[94]J. E. Cunningham, K. W. Goossen, M. Williams, and W. Y. Jan, J. Vac. Sci. Technol. B. **10**, 949 (1992).

[95]K. W. Goossen, J. E. Cunningham, and W. Y. Jan, Elec. Lett. **28**, 1833 (1992).

[96]I. J. Fritz, D. R. Myers, G. A. Vawter, T. M. Brennan, and B. E. Hammons, Appl. Phys. Lett. **58**, 1608 (1991).

[97]Y. C. Tzeng, S. S. Li, Y. W. Lin, P. Ribas, and R. M. Park Appl. Phys. Lett. **58**, 2396 (1991).

[98]A. C. Warren, J. H. Burroughes, J. M. Woodall, D. T. McInturff, R. T. Hodgson, and M. R. Melloch, IEEE EDL-**12**, 527 (1991) and M. R. Melloch, N. Otsuka, J. M. Woodall, A. C. Warren, and J. L. Freeouf, Appl. Phys. Lett. **57**, 1531 (1990).

[99]D. L. Rogers, J. M. Woodall, G. D. Pettit, and D. McInturff, IEEE EDL-**9**, 515 (1988).

[100]A. G. Dentai, J. C. Campell, C. H. Joyner, and G. J. Qua, Electron. Lett., **23** (1987).

[101]B. Elman, C. Jagannath, A. N. M. Masum Choudhury, A. Silletti, A. Negri, and J. Powers, SPIE **1362**, 610 (1990).

[102]M. Zirngibl, J. C. Bischoff, D. Theron, and M. Ilegems, IEEE EDL-**10**, 336 (1989).

[103]M. Zirngibl and M. Ilegems, J. Appl. Phys. **69**, 8392 (1991).

[104]E. A. Fitzgerald , Y. -H. Xie, M. L. Green, D. Brasen, A. R. Kortan, J. Michel, Y. -J. Mii, and B. E. Weir, Appl. Phys. Lett. **59**, 881 (1991).

[105]F. K. LeGoues, B. S. Meyerson, and J. F. Morar, Phys. Rev. Lett. **66**, 2903 (1991).

[106]F. K. LeGoues, B. S. Meyerson, J. F. Morar, and P. D. Kirchner, J. Appl. Phys. **71**, 4230 (1992).

[107]D. Hull and D. J. Bacon, *Introduction to Dislocations*, (Pergammon Press, New York,1984), p. 168.

[108]G. S. Green, B. K. Tanner, S. J. Barnett, M. Emeny, A. D. Pitt, C. R. Whitehouse, and G. F. Clark, Philos. Mag. Lett. **62**, 131 (1990).

[109]A. Lefebvre, C. Herbeaux, and J. DiPersio, Philos. Mag. A **63**, 471 (1991).

[110]W. Hagen and H. Strunk, Appl. Phys. **17**, 85 (1978).

[111]J. Tersoff, Appl. Phys. Lett. **62**, 693 (1993).

[112]J. C. Bravman and R. Sinclair, J. Electr. Microscopy Techn. **1**, 52 (1984).

[113]J.-P. Reithmaier, H. Riechert, H. Schlotterer, and G. Weimann, J. Cryst. Growth **111**, 407 (1991).

[114]H. Ito and T. Ishibashi, Jap. J. Appl. Phys. **25**, L421 (1986).

[115]M. T. Emeny, L. K. Howard, K. P. Homewood, J. D. Lambkin, and C. R. Whitehouse, J. Cryst. Growth **111**, 413 (1991).

[116]R. K. Willardson and A. C. Beer, Eds., *Semiconductors and Semimetals*, Vol. 33 "Strained-Layer Superlattices: Materials Science and Technology," (Academic Press, New York, 1991), p.32.

[117]R. K. Willardson and A. C. Beer, Eds., *Semiconductors and Semimetals*, Vol. 33 "Strained-Layer Superlattices: Materials Science and Technology," (Academic Press, New York, 1991), p.90-91.

[118]R. K. Willardson and A. C. Beer, Eds., *Semiconductors and Semimetals*, Vol. 33 "Strained-Layer Superlattices: Materials Science and Technology," (Academic Press, New York, 1991), p.20-21.

[119]R. K. Willardson and A. C. Beer, Eds., *Semiconductors and Semimetals*, Vol. 33 "Strained-Layer Superlattices: Materials Science and Technology," (Academic Press, New York, 1991), p.55.

[120]G. Bastard, *Wave Mechanics Applied to Semiconductor Heterostructures*, (Les Editions de Physique, France, 1988), p. 296.

[121]N. G. Anderson, W. D. Laidig, R. M. Kolbas, and Y C. Lo, J. Appl. Phys. **60**, 2361 (1986).

[122]S. M. Wang, T. G. Andersson, and M. J. Ekenstedt, Appl. Phys. Lett. **59**, 2156 (1991).

[123]G. Bastard, *Wave Mechanics Applied to Semiconductor Heterosturctures*, (Les Editions de Physique, France 1988), p. 313.

[124]B. Elman, E. S. Koteles, P. Melman, C. Jagannath, C. A. Armiento, and M. Rothman, J. Appl. Phys. **68**, 1351 (1990).

[125]P. Berger, K. Chang, P. Bhattarcharya, J. Singh, and K. K. Bajaj, Appl. Phys. Lett. **53**, 684 (1988).

[126]R. K. Willardson and A. C. Beer, Eds., *Semiconductors and Semimetals*, Vol. 33 "Strained-Layer Superlattices: Materials Science and Technology," (Academic Press, New York, 1991), p.92.

[127]A. Fischer-Colbrie, Hewlett-Packard Laboratories, private communication, 1992.

[128]This was chosen based on work in rapid thermal processing growth of SiGe discussed with Dr. J. Hoyt, Stanford University, February 1992.

[129]These initial steps were used in an attempt to prevent an overshoot of the In furnace temperature in going from the idle condition to measurable In flux.

[130]Y. C. Pao, Ph.D. Thesis, Stanford University, 1990.

[131]R. K. Willardson and A. C. Beer, Eds., *Semiconductors and Semimetals*, Vol. 33 "Strained-Layer Superlattices: Materials Science and Technology," (Academic Press, New York, 1991), p. 98.

[132]J. M. Vandenberg, R. A. Hamm, M. B. Panish, and H. Temkin, J. Appl. Phys. **62**, 1278 (1987).

[133]Poisson's ratio does depend on composition for InGaAs and AlGaAs. However, the ratio f is approximately constant and equal to 2.0 for InGaAs and 1.9 for AlGaAs over a wide range of compositions.

[134]Charles Kirschbaum, Charles Evans and Associates, Redwood City, CA

[135]G. Bastard, *Wave Mechanics Applied to Semiconductor Heterostructures*, (Les Editions de Physique, France, 1988), p. 272-3, 290, 295-296.

[136]For a more complete discussion of the nonradiative defects in InGaAs/AlGaAs quantum wells, see S. M. Lord, G. Roos, J. S. Harris, Jr., and N. Johnson, J. Appl. Phys. **73**, 740 (1993).

[137]D. Harris, Charles Evans and Associates. This sample would probably take 4-8 hours at $300/h. Etching to remove the top is not recommended as it may roughen the surface. Accuracy should be better than 5 relative % with good standards.

[138]Popt= 0.9 mW, Photocurrent = 135 μA, R1=0.32, R2=0.8 (Ag paint used)

[139]Measurement performed by Dr. Bardia Pezeshki at IBM T. J. Watson Research Center, Yorktown Heights, NY, 1992.

[140]A. M. Fox, D. A. B. Miller, G. Livescu, J. E. Cunningham, and W. Y. Jan, IEEE J. Quant. Electron., QE-**27**, 2281 (1991).

[141]S. M. Lord, G. Roos, B. Pezeshki, and J. S. Harris, Jr., Appl. Phys. Lett. **60**, 2276 (1992).

[142]G. H. Olsen, J. Cryst. Growth **31,** 223 (1975).

[143]using b=4 Å β=0.75, and $\mu_f = \mu_s = 0.5(c_{11}-c_{11})$

[144]M. Shur, *GaAs Circuits and Devices*, (Prentice Hall, Englewood Cliffs, New Jersey, 1990).

[145]J. W. P. Hsu, E. A. Fitzgerald, Y. H. Xie, P. J. Silverman, and M. J. Cardillo, Appl. Phys. Lett. **61**, 1293 (1992).

[146]This clear region is definitely not a function of the TEM sample becoming thinner near the MQW as it is seen in all samples.

[147]E. A. Fitzgerald, Y. -H. Xie, D. Monroe, P. J. Silverman, J. M.Kuo, A. R. Kortan, F. A. Thiel, and B. E. Weir, J. Vac. Sci. Technol. B **10** 1807 (1992).

[148]E. A. Fitzgerald, AT&T Bell Laboratories, private communication, April 1993.

[149]J. E. Cunningham, AT&T Bell Laboratories, private communication, 1992.

[150]J. E. Cunningham, AT&T Bell Laboratories, private communication, 1992.

[151]K. W. Jelley, R. W. H. Engelmann, K. Alavi, and H. Lee, Appl. Phys. Lett. **55**, 70 (1989).

[152]Coating performed at CVI Laser Corporation, Livermore, CA 94550 (510) 449-1064

[153]EpoTech H20E

[154]S. M. Lord, B. Pezeshki, and J. S. Harris, Jr., submitted to Optical and Quantum Electronics.

[155]S. M. Lord, B. Pezeshki, A. F. Marshall, J. S. Harris, Jr., R. Fernandez, and A. Harwit, MRS Symp. D, Fall 1992, Paper D2.7.

[156]B. Pezeshki, Ph.D. Thesis, Stanford University 1991, Chapter 4.

[157]H. A. MacLeod, *Thin Film Optical Filters* (Macmillan, New York), 1986.

[158]Sample with GaAs barriers described in Chapter 7.

[159]I. J. Fritz, B. E. Hammons, A. J. Howard, and T. M. Brennan, Appl. Phys. Lett. **62**, 919 (1993).

[160]H. C. Chui, S. M. Lord, M. M. Fejer, and J. S. Harris, Jr., Paper QWB6 in OSA Quantum Optoelectronics Topical Meeting, 1993 Technical Digest (Optical Society of America, Washington, D. C. 1993), Vol. 8, 1993.